Study on nanostructured electrocatalysts for oxygen reduction reaction in polymer electrolyte fuel cells

朴，佳榮

Study on nanostructured electrocatalysts for oxygen reduction reaction in polymer electrolyte fuel cells

Kayoung Park

A Dissertation

for the Degree of Doctor of Engineering

at

Department of Materials Process Engineering

Graduate School of Engineering

Kyushu University

2017

Contents

I

Chapter 1

Introduction

1.1 Fundamentals of polymer electrolyte fuel cells

The alternative energy sources have been demanded for the past few decades due to the increasing consumption of energy resources, the high cost of energy, the continuous and rapid depletion of fossil fuels, and the environmental problems such as emission of harmful pollutants like CO_2, NO_x, SO_x. Fuel cells convert chemical energy directly into electric energy with fuel and oxidant, resulting in high efficiency, low emissions, and low environmental impact. Consequently, fuel cells are a very attractive alternative device [1–4]. In particular, polymer electrolyte fuel cells (PEFCs) as one of the fuel cells can be applied to fields such as portable electronics, vehicles, and combined heat and power (CHP) system etc. In addition, the PEFCs have been actively developed due to their low operating temperature in range of $20 \sim 100$ ℃, simplicity, high power density, and quick start-up [5]. These PEFC's systems are composed of stack which means a number of single cells in series and some components such as fuel processor, humidifiers, air compressors, and power conditioners, etc [6,7]. The single cell of PEFCs is shown in Fig. 1.1. The PEFCs consist of a membrane electrode assembly (MEA), two bipolar plates as separators, and two seals. The MEA which is known as a critical component of PEFC is comprised of a proton exchange membrane (PEM) which is usually Nafion®, two
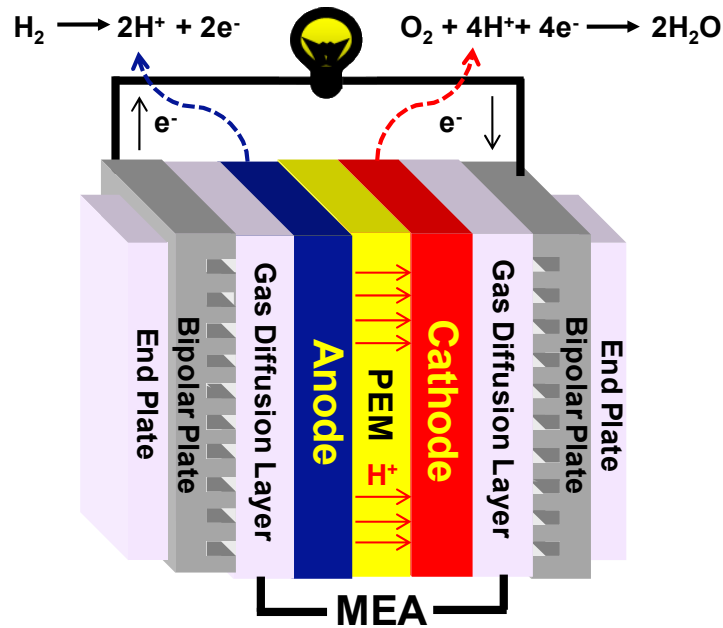
Fig. 1.1 Schematic diagram of PEFCs.

dispersed catalyst layers (anode and cathode), and two gas diffusion layers which offer

the fuels and oxygen (air). Hydrogen oxidation reaction (HOR) and oxygen reduction

reaction (ORR) occur at the anode and cathode in the MEA, respectively. The membrane

allows protons to pass through to complete the overall reaction while it separates the half

reactions at the anode and cathode [8]. The electrons also flow through an external load

circuit from the anode to the cathode. During operation of PEFCs, the oxygen molecule

is reduced by the protons and electrons, resulting in the generation of water, electricity,

and heat. The theoretical open circuit voltage is given as 1.229 V where both HOR and

ORR simultaneously occur. However, the PEFCs generate the lower actual voltage than

1.229 V due to their overpotential or irreversible voltage losses. Figure 1.2 shows voltage

losses of PEFCs [6]. Activation losses at low current density give rise to significant

voltage drop and occur primarily at the cathode because reaction rate of the ORR on the
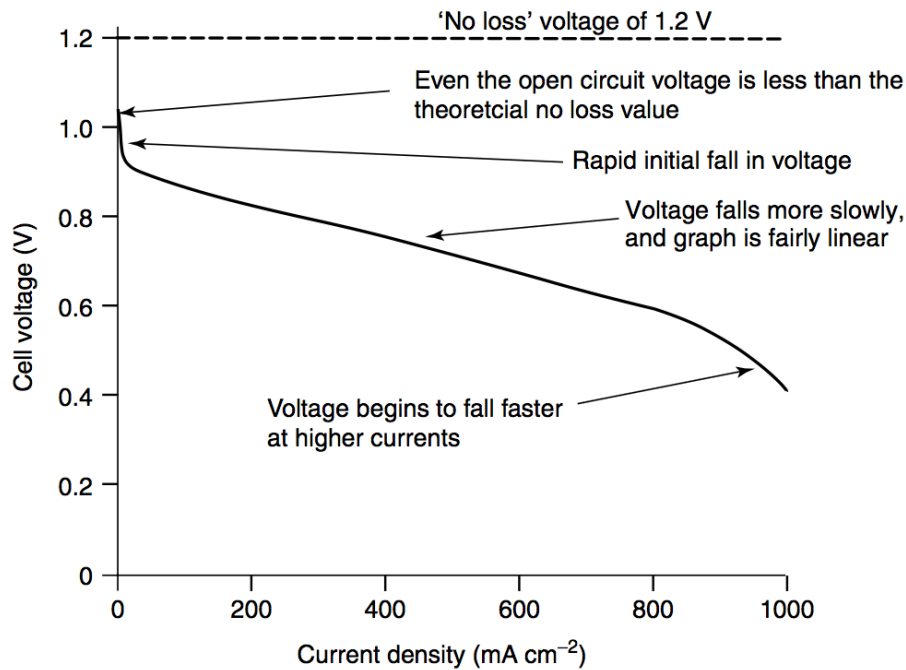
Fig. 1.2 Voltage losses of PEFCs [6].

cathode is much slower than that of the HOR on the anode. Fuel crossover/internal current losses associated with the electrolyte also take place at low current densities by either fuel leaking or electrons leaking through the electrode. In the Fig. 1.2, voltage falls more slowly and graph is fairly linear as results of ohmic losses which are generated by electrical resistance of the electrodes and the resistance to the flow of ions in the electrolyte. Voltage then begins to fall faster at higher currents caused by the mass transport/concentration losses. These losses affect the theoretical voltage, which results in the degradation of their performance in the PEFCs [6,9].

1.2 Challenges of conventional Pt catalysts

As mentioned above, the oxygen reduction reaction (ORR) occurs at the cathode. The

3

ORR has two pathways including direct four-electron reaction and a series of two-electron reaction, respectively. In the direct 4-electron pathway, O_2 is directly reduced to H_2O (Eq 1), which offers higher operation potentials and current efficiency in the PEFCs. In contrast, the two-electron reaction takes place at low potential and produces H_2O_2 as an intermediate by-product (Eq 2). The produced H_2O_2 is reduced to H_2O (Eq 3). The formation of H_2O_2 at cathode results in oxidative degradation of the membrane.

$$O_2 + 4H^+ + 4e^- \rightarrow H_2O \qquad \text{1.229 V vs. NHE} \qquad (1)$$

$$O_2 + 2H^+ + 2e^- \rightarrow H_2O_2 \qquad \text{0.70 V vs. NHE} \qquad (2)$$

$$H_2O_2 + 2H^+ + 2e^- \rightarrow 2H_2O \qquad \text{1.76 V vs. NHE} \qquad (3)$$

The direct 4-electron reaction of O_2 is thus preferred, resulting in high ORR activity, as compared to the series of two-electron reaction. The most commonly used metal catalyst for the ORR at the cathode is Pt catalyst due to their efficient ORR ability [11–14]. However, the Pt cathode catalysts are facing the problems that are related to their degradation. The degradation of the Pt catalysts takes place under severe cathode conditions such as low pH value, high temperature, highly positive potential, high humidity, and oxidant feeds, which result in catalytic activity loss [15]. Figure 1.3 shows simplified mechanisms of Pt degradation on a carbon support in the PEFCs. The Pt degradation is divided into various processes : (i) dissolved Pt ion transport in the ionomer phase and then reprecipitation by H_2 crossover through the membrane, (ii) Ostwald ripening on the carbon support, (iii) coalescence of Pt nanoparticles via Pt crystal migration on the carbon support, and (iv) detachment and agglomeration of Pt nanoparticles from the carbon support [16–20]. These processes of Pt degradation can
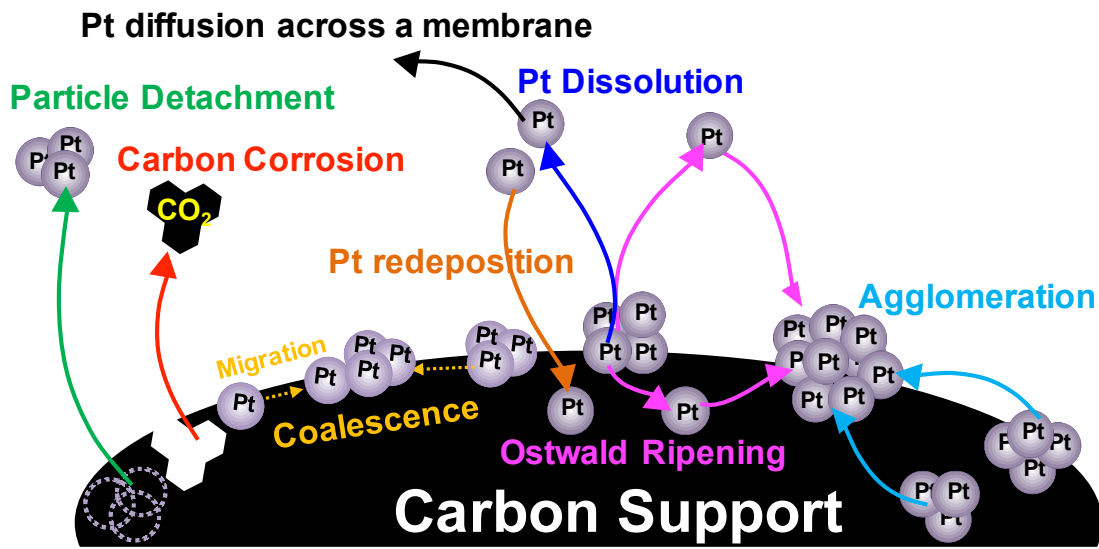
Fig. 1.3 Simplified mechanism of Pt degradation on a carbon support in the fuel cells.

distinguish conceptually between primary and secondary degradation phenomena. The Pt dissolution as a primary degradation process can induce secondary processes such as Pt deposition in the ionomer or Ostwald ripening. Moreover, carbon corrosion is another primary degradation phenomenon which causes secondary degradation processes such as Pt particle detachment or agglomeration [18]. These degradation phenomena of the Pt catalysts eventually reduce their catalytic activity. In particular, during start-stop cycles of PEFCs, severe activity loss of Pt catalysts is caused by such Pt degradation phenomena due to their instability, which results in a decrease of durability. In other words, to prevent the Pt degradation, the stability of the Pt catalysts is an important factor for high performance fuel cells under the severe cathode conditions [21]. Therefore, more stable Pt or non-Pt cathode catalysts, which can replace the conventional Pt catalysts, should be developed to avoid the degradation of catalysts under severe cathode conditions. However, the challenge of cathode catalysts has yet to be solved.

5
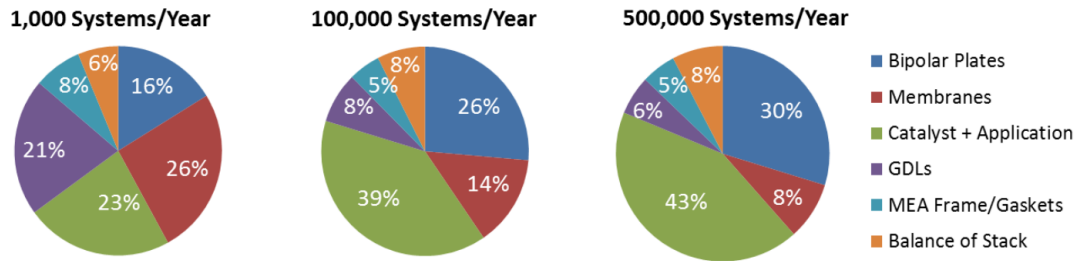
Fig. 1.4 A breakdown of stack component cost depending on the number of system

One of the most challenging problems is high cost of PEFCs for commercialization, which can be attributed to cathode catalysts. Recently, Adria Wilson et al. reported on 2016 projected cost of 80-kWnet transportation fuel cell stacks and systems depending on system units per year. Stack cost (153 $ / kWnet) at 1,000 units/year accounted for approximately 71 % of total system cost (215 $ / kWnet), while stack cost (27 $ / kWnet) at 500,000 units/year formed about 52 % of total system cost (53 $ / kWnet). Namely, an increase in the number of system units reduced the total system cost with a decrease in the percentage of the stack cost. Figure 1.4 shows a breakdown of stack component cost depending on the number of system units. The stack cost at 1,000 systems/year is dominated by two components such as membrane and (catalyst + application). When production volume of fuel cell systems increases from 1,000 to 500,000 systems/year, the percentage of the membrane decreases from 26 % to 8 % in fuel cell stack cost. In contrast, the part of (catalyst + application) increases from 23% to 43 % with rising in the systems despite decrease in the stack cost at 500,000 systems/year. This is caused by the cost of Pt metals used as catalysts in the both electrodes for PEFCs [22]. It was reported that the Pt metal, average monthly calculation, significantly increased from the price of $1234 per ounce for 2007 to $1724 per ounce for 2011 and then decreased the Pt price of $ 993 per

ounce for 2016 as for trend of the Pt price in the market. These trends of the Pt price are variable so that one can have an effect on the cost of fuel cell systems [23]. To commercialize the PEFCs, it is necessary to reduce the utilization of Pt or develop non-Pt catalysts which can meet the higher performance than the conventional Pt catalysts. In order to solve the challenges of the conventional cathode catalysts, more efficient, inexpensive, and stable electrocatalysts are required.

1.3 Cathode electrocatalyst approaches

A number of cathode catalysts have been developed to solve the challenges of the conventional Pt catalysts. These studies can be classified into three groups such as Pt-based catalysts, supporting materials, and non-Pt metal catalysts.

1.3.1 Pt-based catalysts

One of the most common Pt-based catalysts to reduce utilization of the Pt is by alloying Pt and transition metals such as Co, Mn, Ni, Fe, and Cu, which are designed for binary alloys or ternary alloys as potential candidates [24–28]. A substantial amount of researches have been carried out over the past decades on carbon-supported binary alloys or ternary alloys which demonstrate 2 ~ 3 times higher mass activity compared to the commercial Pt catalysts. In addition, the ORR activity of these Pt-alloy catalysts such as Pt-Co, Pt-Ni, Pt-Fe, Pt-Cr, Pt-V, Pt-Ti, Pt-W, Pt-Al, and Pt-Ag has been improved by the shorter Pt-Pt bond distances and the structure-sensitive inhibiting effects of OH_{ads} [29,30]. Due to the highest possible Pt utilization, core-shell catalyst which is composed of Pt
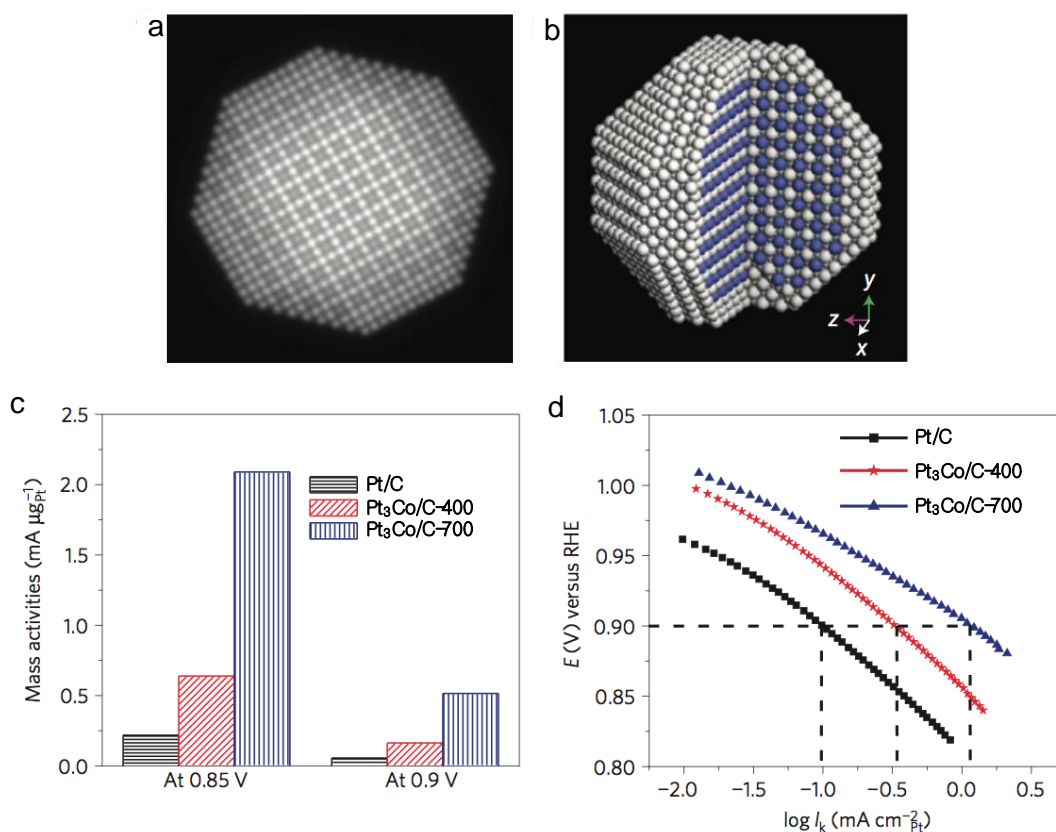
Fig. 1.5 (a) Multislice simulated ADF-STEM image of the idealized nanoparticle. (b) The idealized atomic structure of the Pt₃Co core–shell nanoparticle and, white and blue spheres present Pt and Co atoms, respectively. (c) Comparison of mass activities for Pure Pt and Pt-Co alloy nanoparticles at 0.85 and 0.9 V and (d) comparison of specific activities (I_k) [31].

located only on the surface of nanoparticles of another metal is highly attractive from a cost perspective. In particular, the largest potential advantage of such core-shell catalyst design is the extraordinarily high electrochemically active surface area (ECSA) caused by the high Pt dispersion [29]. Wang et al. demonstrated that prepared Pt-Co core-shell nanoparticles were comprised of ordered Pt₃Co intermetallic cores with a 2~3 atomic layer thick Pt shell and showed impressive activity. Idealized Pt-Co nanoparticles are shown in Fig. 1.5a-b. As comparison of mass activities (Fig. 1.5c), carbon-supported

Pt$_3$Co nanoparticles after heat-treatment at 700℃ (denoted as Pt$_3$Co/C-700) exhibit one of the highest electrocatalytic activities for the ORR. Figure 1.5d also presents the specific activity of Pt$_3$Co/C-700 is 1.1 mA cm^{-2} at 0.9 V, which is much higher than those of pure Pt and Pt$_3$Co/C-400 (after heat-treatment at 400℃). This high activity is attributed to the Pt-rich shell as well as the stable intermetallic Pt$_3$Co core arrangement, which arise from the strain put on the Pt surface via lattice mismatch resulting in the Pt$_3$Co with the smaller lattice constant than Pt shell. So far, this mass activity for the ORR is the highest among the Pt-Co systems reported in the literature under similar testing conditions [31]. As other studies, shape-controlled catalysts also show a highly promising class of ORR catalyst due to their extremely high mass activities. Stamenkovic et al. demonstrated that the Pt$_3$Ni(111) surface is 10 times more active for the ORR than the corresponding Pt(111) surface and 90 times more active than the current-of-the-art commercial Pt/C catalysts for PEFC. The Pt$_3$Ni(111) surface has an unusual electronic structure (d-band center position) and arrangement of surface atoms in the near-surface region. Under operating conditions relevant to fuel cells, its near-surface layer exhibits a highly structured compositional oscillation in the outermost and third layers, which are Pt-rich, and in the second atomic layer, which is Ni-rich. The weak interaction between the Pt surface atoms and nonreactive oxygenated species increases the number of active sites for O$_2$ adsorption [32]. Interestingly, Pt-based nanoframe showed significantly higher mass activity up to 20 times than commercial Pt/C based on RDE studies. Particularly, the largest advantage of such nanoframe is their superb stability and durability during voltage cycling [28,29]. Chen et al. synthesized a highly active and durable class of electrocatalysts by exploiting the structural evolution of Pt-Ni bimetallic nanocrystals. The synthesized Pt$_3$Ni

nanoframe catalysts achieved 36-fold enhancement in the mass activity and 22-fold enhancement in the specific activity, respectively, for the ORR (relative to state-of-the-art Pt/C) during prolonged exposure to reaction conditions [33].

1.3.2 Support materials for Pt catalysts

Carbon blacks have been widely used as support materials for PEFC catalysts due to their high electrical conductivity, affordability, and accessibility, relatively high chemical and electrochemical stability [34]. However, when it is used as supports for the Pt or Pt-based alloy catalysts, the carbon black suffers from carbon corrosion under the severe cathode conditions, leading to the Pt degradation which results in the lower performance. This is caused by weak interaction between support and nanoparticles. When the carbon blacks with an average pore diameter below 2 nm are used as supports for Pt or Pt-based alloy catalysts, supply for a fuel to the catalyst layer may not be smooth and efficient, and the catalytic activity starts to be limited by mass transfer. Furthermore, it is known that micropores of amorphous carbon particles are poorly connected. To solve the problems for carbon blacks as the supports, many support materials have thus been developed [35–39]. One of the common support materials is carbon material including carbon nanotubes (CNTs), carbon nanofibers (CNFs), graphene, ordered mesoporous carbon, and carbon nanocages. Mesoporous carbons with the range of 2 to 50 nm of pore diameter present important porous features such as pore connectivity, pore size, distribution, and pore length, which can influence catalytic performance [14,40–44]. In addition, the

(a)

Armchair   Zig-Zag type   Helical type

Carbon nanotubes

(b)

(c)

Platelet type   Tubular type   Fishbone type

Carbon nanofibers
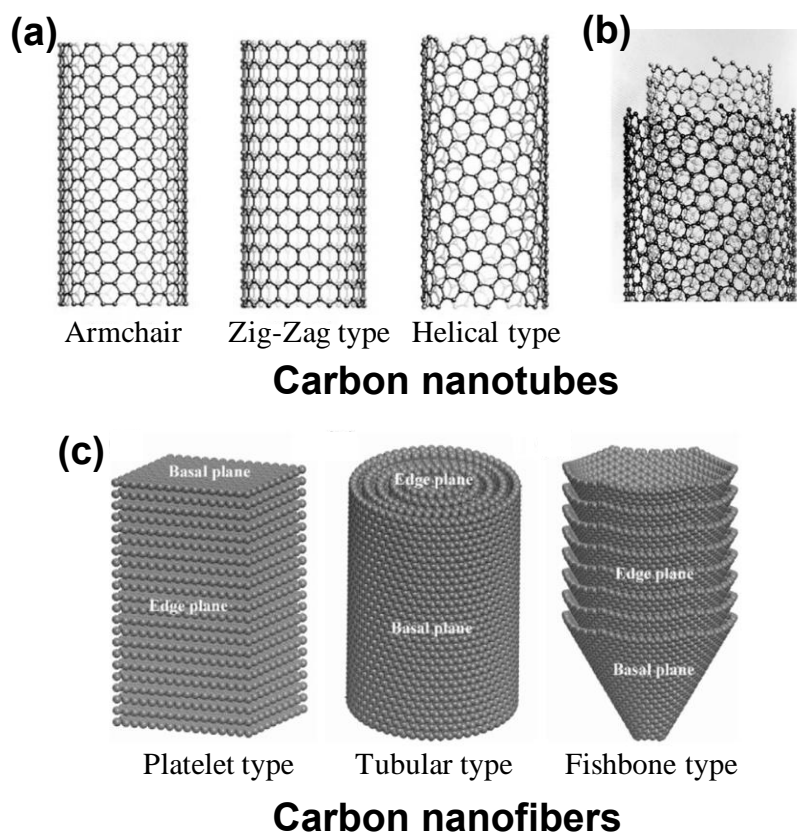
Fig. 1.6 Schematic representations of (a) single-wall CNTs and (b) multi-wall CNTs, and (c) three types of CNFs [46,47].

mesoporous carbons have high surface area and few or no micropores, and high distribution of Pt or Pt-alloy nanoparticles and result in a largely effective Pt surface area with high catalytic activity. The mesoporous structures also facilitate smooth mass transport, yielding high limiting current values. In particular, the support materials with high graphic nature (e.g. CNFs and CNTs) among the various mesoporous carbons are reportedly more stable [1,45]. Both CNFs and CNTs also possess the unique surface structures, excellent mechanical and thermal properties, and high electric conductivity and surface area. Many types of CNTs and CNFs are shown in Fig. 1.6. The CNTs are classified as single-wall CNT (SWNT) and multi-wall CNT (MWNT). The SWNT is a

seamless cylinder enclosed by a single graphene sheet. The MWNT can be considered as a concentric SWNT with an increasing diameter and is coaxially disposed. On the other hands, CNFs are well known as platelet, tubular, and fishbone types. The platelet type CNF has graphene layers perpendicular to the growth axis. The tubular type CNF has graphene layers parallel to the growth axis with multi-wall assembly. The fishbone type CNF also has graphene layers with an angle of 45° to the growth axis [46,47]. These graphic carbons are expected to offer great potential for catalyst supports. However, it is necessary to modify their surfaces via various methods such as non-covalent polyelectrolyte functionalization or strong oxidation because the graphic carbons are relatively inert [34,48,49]. Guha et al. reported that modified CNF as functionalized graphitic carbon by concentrated acid treatment showed the higher performance than activated carbons as amorphous carbons and is comparable to the commercial Pt catalysts during single cell test because the CNFs have the lower ohmic losses than the activated carbons measured by electrochemical impedance spectroscopy (EIS) [50,51]. In addition, Sebastián et al. investigated three different CNFs with varying in terms of average diameter, ordering degree, and surface structure as Pt supports for the cathode in PEFCs. These three different CNFs were prepared by different temperatures using catalytic chemical vapor deposition method. Dispersion of Pt on Vulcan (carbon blacks) does not appear better than that of CNF as shown in Fig. 1.7a-d. Among the CNF-supported Pt(Pt/CNF) catalysts, Pt catalyst supported on the CNF prepared at 650 ℃ (Pt/CNF650) showed the highest ECSA values due to its best compromise in terms of support surface area and dispersion of Pt as resulting from a moderate concentration of surface groups in the support in Fig. 1.7e. In contrast, carbon black supported Pt catalyst and Pt catalyst supported on the CNF prepared at 550 ℃ (Pt/CNF550) presented very low mass activities,
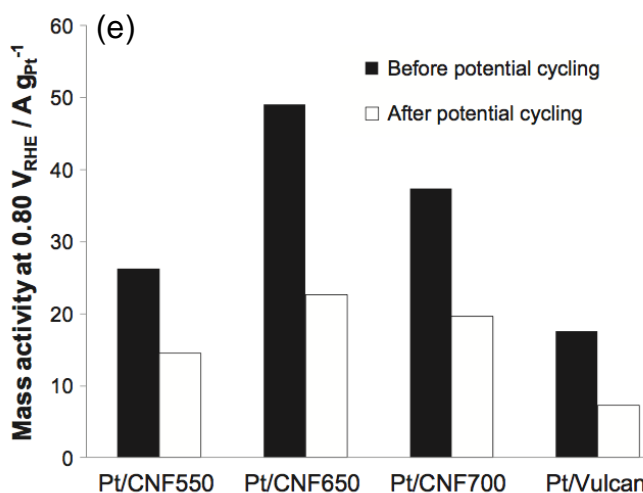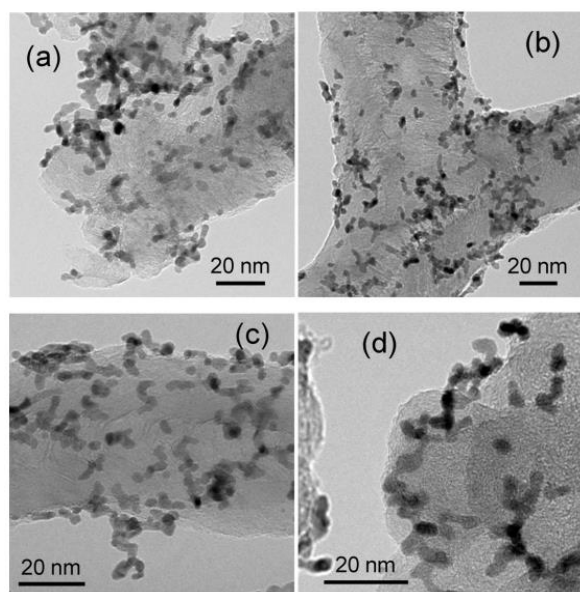
Fig. 1.7 TEM micrographs of (a) Pt/CNF550, (b) Pt/CNF650, (c) Pt/CNF700, and (d) Pt/Vulcan and (e) their mass activities in the ORR before and after Pt degradation from polarization curves at 0.80 V vs. RHE [36].

which was caused by a large number of support surface groups and defects. The highest performance was also obtained both before and after the accelerated degradation tests for the Pt/CNF650 catalysts, which is attributed to the highest ECSA and proper graphitic character of the support [36]. Similarly, it was observed that graphitic CNT(GCNT)

supported Pt catalysts showed enhanced ORR activity, which was attributed to the high graphitization degree of GCNTs as well as the high electrochemical surface area of Pt nanoparticles [52]. Consequently, such carbon material supports including specialized CNT, CNF, graphene, and other types of carbon material supports do offer improved ORR activity, compared with the conventional carbon black [14]. On the other hand, non-carbon materials including titanium oxides, cerium oxide, niobium oxide, tungsten oxide, some carbides, nitrides, oxynitrides, borides, and conductive polymers also have been developed [34,53–55]. Titanium dioxide as one of non-carbon materials presents high chemical and electrochemical stability, along with strong interaction with metal nanoparticles, showing great potential as an alternative support material for PEFCs [14]. Huang et al. reported that a novel TiO_2-supported Pt electrocatalyst (Pt/TiO_2) showed excellent fuel cell performance due to its low mass transport limitation in the cathode catalyst layer. The Pt/TiO_2 also had an ultrahigh stability compared to the conventional Pt catalyst, which can be attributed to a strong metal support interaction between the Pt particles and TiO_2 support [56].

1.3.3 Non-Pt metal catalysts

Non-Pt metal catalysts with various types of active components have been studied due to their potential to greatly reduce cost as well as overcome limitation of the commercial Pt catalysts having insufficient performance, stability, and durability. Recent non-Pt metal catalysts have demonstrated sufficient performance to be considered for use in certain nonautomotive applications such as backup power and/or portable power, which have significantly lower performance, stability, and durability requirements than automotive applications [29].
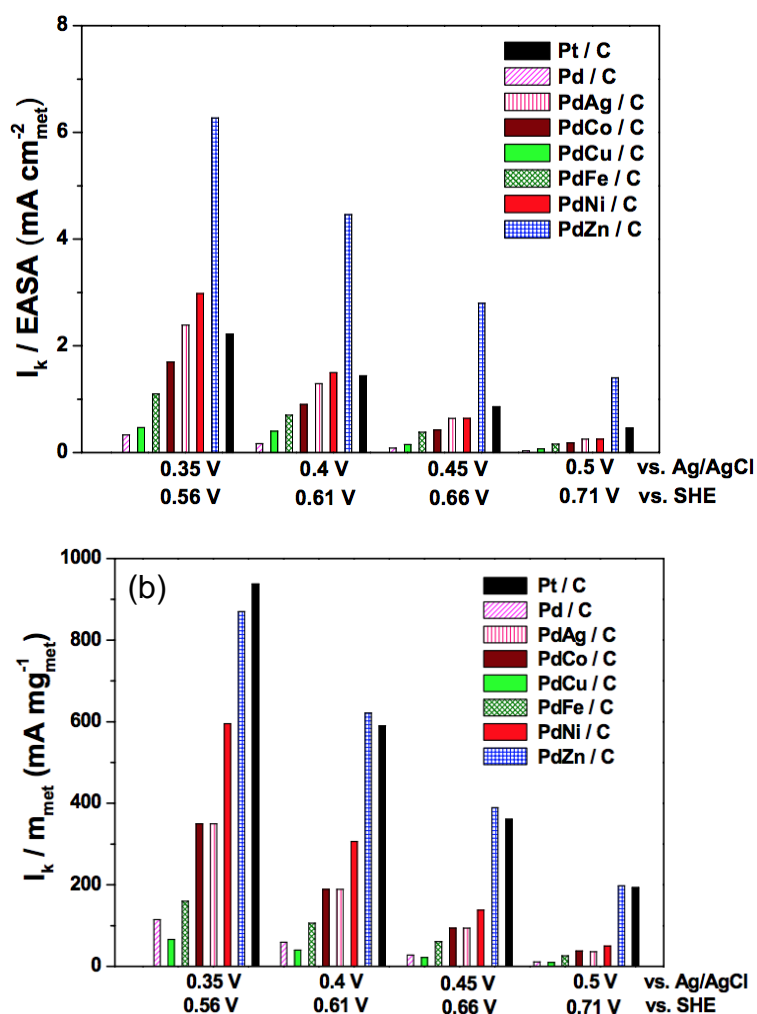
Fig. 1.8 Histograms showing at selected potentials, (a) specific activity and (b) mass activity [60].

One of the non-Pt metal catalysts is by using Pd as the main metal. Pd, it is much less costly than Pt, has similar physical properties to Pt, including fcc crystal structure and a similar atomic radius. Indeed, Pd-based catalysts have been developed by either changing their structure, shape, and particle size or alloying other metals such as Co, Ni, and Au [57–59]. Electrocatalytic activities of various Pd-alloy catalysts were investigated in Fig. 1.8. Bampos et al. reported that many Pd-M (M = Ag, Co, Cu, Fe, Ni, and Zn) alloy catalysts show the different ORR activities depending on types of transition metals.

15
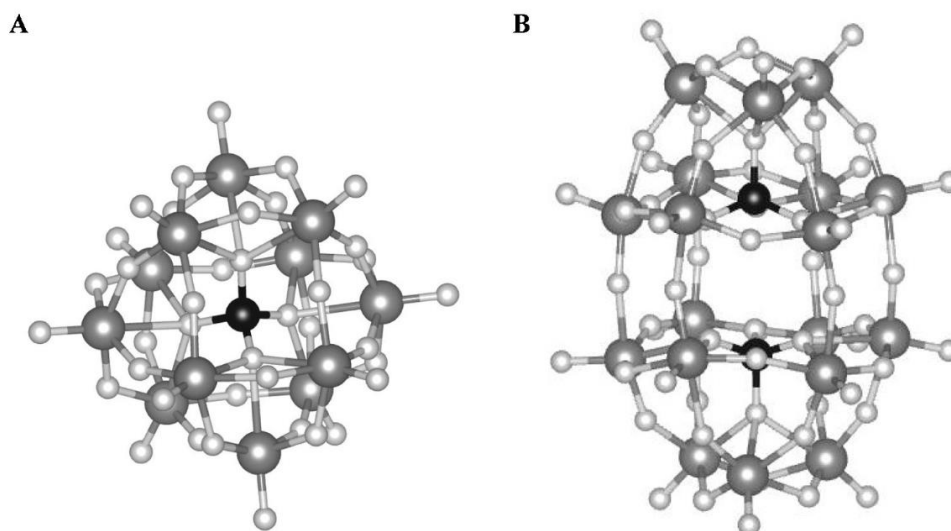
Fig. 1.9 Ball and stick diagrams showing (A) Kegging (B) Wells-Dawson HPA variants where, phosphorus atoms are black, addenda atoms are dark [64].

Among the tested Pd/C and Pd-alloy catalysts, the PdZn/C electrocatalyst exhibited significantly higher specific activity and similar mass activity compared to Pt/C. In particular, the specific activity of the PdZn/C was $2.8 \sim 3.3$ times higher than that of Pt/C, whereas its mass activity was slightly lower at 0.35 V vs. Ag/AgCl and slightly higher for $0.4 - 0.5$ V vs. Ag/AgCl. This clearly demonstrates the superiority of the PdZn/C over the Pd/C [60]. In addition, Kondo et al. reported the ORR activity trend on the low index planes of Pd. It was observed that the current density of the ORR on Pd(100) was nearly three times as high as that on Pt(110) at 0.90 V vs. RHE, indicating that Pd(100) structure is the active site for the ORR on Pd electrodes [57].

Some researches on metal chalcogenides catalysts, mainly Se or S-based, have attracted significant attention since Alonso-Vante and Tributsch discovered that $Ru_2Mo_4Se_8$ had the ORR activity comparable to Pt in aqueous H_2SO_4. The metal chalcogenides catalysts including S, Se, and Te showed good ORR activity [5,61−63].

Heteropolyacids (HPAs)-based catalysts have been attracting attention because of their unique structures which are capable of the ORR via oxidation and reduction (redox). Typical HPAs contain Keggin ($H_nXM_{12}O_{40}$) and Wells-Dawson ($H_nX_2M_{18}O_{62}$) structures composed of a particular combination of hydrogen and oxygen with heteroatoms (X) such as P or Si and addenda atoms (M) W, Mo, and V as shown in Fig. 1.9 [64]. These HPAs as fuel cell catalysts have an advantage because they can simplify the ionomer needs of the electrode and theoretically reduce the complexity of the three phases boundary. Moreover, it is known to be stable under the high voltages and low pH conditions which are similar to the PEFC cathode conditions. These HPAs can go through multiple reversible 1 or $2e^-$ reductions while still retaining their structure. In particular, the HPAs with Mo addenda atoms can produce steady and significant current densities due to their outstanding redox abilities. This high activity for the ORR on the HPA-based catalysts may be caused by the HPA to be reduced by $4e^-$. In addition, the potential where the HPA-based catalyst begins the ORR in the polarization curves can be improved by substituting two or three V atoms into the HPA structure, which positively shifted the reduction potential [64,65].

Other types of non-Pt catalysts, including carbon based-non-Pt metal catalysts and metal-free catalysts, also have been reported. It was found that either Fe- and/or Co-based catalysts show interesting properties for the ORR [14,66]. Lefèvre et al. produced microporous carbon-supported Fe-based catalysts(Fe/N/C) with active sites including Fe cations coordinated by pyridinic nitrogen functionalities in the interstices of graphitic sheets within the micropores. The synthesized Fe/N/C catalysts showed the best current density among all Fe-based electrocatalysts reported in the paper and also were equal to Pt-based cathode with a Pt loading of 0.4 mg cm^{-2} at 0.9 V [67]. Other research groups

reported that metal oxide catalysts, particularly group 4 and 5 metals, in the form of metal nitrides and oxynitrides, and metal carbonitrides. The metal oxide catalysts have definite catalytic activity for the ORR due to their chemically good stability in acidic electrolytes [68,69]. Chisaka et al. recently demonstrated the successful syntheses of zirconium oxynitride (ZrO_xN_y) catalysts on multi-walled carbon nanotubes. The catalyst showed the highest ORR activity among other oxide-based catalysts tested by his research group. In addition, the single-cell performance of these ZrO_xN_y catalysts presented 10 mA cm^{-2} at 0.9 V. Such a high performance has never been reported for Fe-free oxide-based catalysts so far, indicating that the ZrO_xN_y catalysts are suitable ORR catalysts for real PEFC cathodes [70].

1.4 Cathode catalysts on the durability aspects

Durability of cathode catalysts is thought to be one of major problems inhibiting the commercialization of PEFCs. The durability is also one of the important factors that can determine lifetime of the PEFCs. Improving the durability for such cathode catalysts thus can lengthen the lifetime of PEFCs, enhance the reliability and reduce the total lifetime cost [71]. However, the durability is reduced by Pt degradation on the Pt-based catalysts and instability of non-Pt-based catalysts under harsh cathode conditions. To solve the reduction in the durability, the researches on the durability of cathode catalysts including both Pt- and non-Pt based catalysts have been reported.

As one of the methods to enhance the durability of the cathode catalysts, silica-coating of Pt or Pd-based catalysts has been developed in our laboratory. We have previously covered CB or CNT-supported metal particles such as Pt and Pd with silica layers. These

silica-coated metal catalysts showed excellent durability because the silica layers around the metal particles prevent the migration of metal particles on the CB or CNT supports and the diffusion of dissolved metal cations out of silica layers under the cathode conditions. Thus, the silica-coating method was our study on the improvement of durability for Pd-Ag catalysts described as chapter 4 [72–75].

1.4.1 Pt-based catalysts on the durability aspects

The conventional Pt catalysts have experienced the Pt degradation including the increase in Pt nanoparticle size or/and the Pt dissolution into an electrolyte, or/and the detachment of the Pt from carbon support, which result in deterioration of the performance following the loss of ECSA during the PEFC operation as shown in Fig. 1.10 [17,71]. Thus, strategies to enhance the durability such as alloying Pt with another metals and development of catalyst supports have been proposed in the Pt-based catalysts. Some approaches have reported that Pt alloy catalysts with a second and/or third metal such as Pt_3Ni/C, Pt-Fe alloy, Pt_4ZrO_2/C, and $Pt_6Co_1Cr_1/C$ showed improved durability, which is attributed to an anchor effect between Pt and another metals [32,76–78]. Zhang et al. demonstrated that Au/Pt/C catalysts by modifying Pt nanoparticles with gold (Au) clusters can be stabilized against dissolution under potential cycling between 0.6 and 1.1 V vs. RHE in over 30,000 cycles, which results in no loss of activity. The Au clusters confer stability by raising the Pt oxidation potential [79]. Development of carbon materials with high graphic nature such as CNT and CNF that can be used as substitute for the carbon black also is one of methods for improvement of durability. An increase in the degree of graphitization leads to stronger π sites (sp^2-hybridized carbon) on the support, which acts as anchoring sites for Pt, thus strengthen the metal-support interaction

and the resistance of Pt to sintering [71]. Recently, Ando et al. demonstrated that Pt/TiO$_2$/cup-stacked CNT (CSCNT) composite catalysts met high catalytic activity and high durability for the ORR. In particular, the Pt/TiO$_2$/CSCNT composite showed no change in the Pt particle size of 3.4 nm after 2000 potential cycling between 0.05 V and 1.1 V vs. RHE as well as 1.0 V and 1.5 V vs. RHE, respectively. This result indicates that for the Pt/TiO$_2$/CSCNT composite, TiO$_2$ matrix composed of Ti oxides and CSCNT anchors the Pt nanoparticles, which prohibits them from aggregating and consequently the durability is improved [80].

1.4.2 non-Pt catalysts on the durability aspects

Prior to 2009, very few publications discussed the cycling durability of non-Pt catalysts, which primarily reported stability data (performance loss during potentiostatic experiments). However, as significant advances have brought the activity of these non-Pt catalysts to a stage where they are becoming industrially relevant, the requirement for durability during voltage cycling has attracted more attention. Thus, since 2009, there have been many reports focusing on the cycling durability of the non-Pt catalysts. Despite many reports on the durability of the non-Pt catalysts, the non-Pt catalysts are still widely observed to suffer from extremely poor stability. The mechanism for the poor stability of the non-Pt catalysts is not known with certainty, and takes place by metal dissolution or leaching of the active metal site, oxidative attack by H$_2$O$_2$, and protonation of the active site [81] . To obtain high stability, many approaches have been proposed. Peng et al. reported Fe- and N- doped carbon catalyst Fe-PANI/C-Melamine with graphene structure. It was found that after 10,000 cycles, the activity decreased by ~ 27%. They highlighted the fact that the Fe-PANI/C-Melamine showed less activity loss at both the low potentials
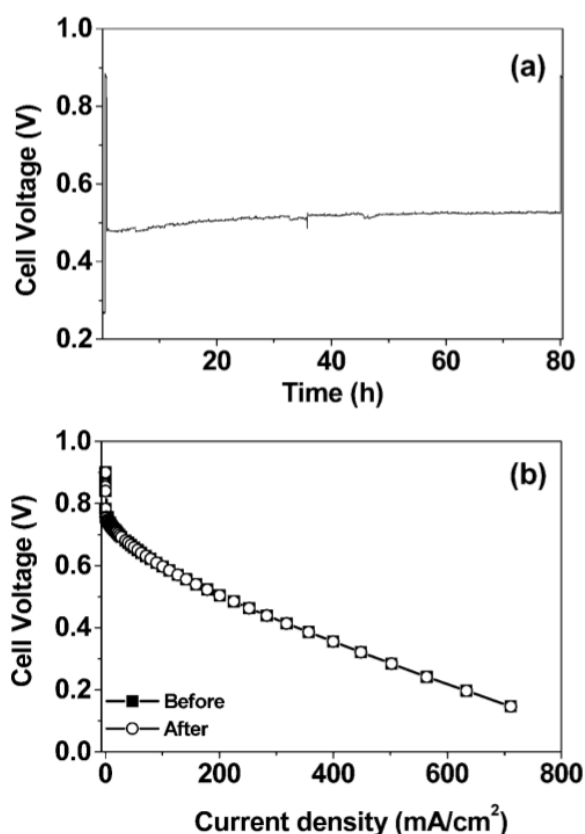
Fig. 1.10 Stability evaluation of Pd-Co-Mo/C (Pd:Co:Mo = 70:20:10 atom %) cathode upon polarizing the cell at 200 mA/cm^2 for 80 h in a single cell PEMFC at 60 °C with a metal(s) loading of 0.2 mg/cm^2 : (a) cell voltage variation during the time of polarization and (b) steady-state polarization curves before and after polarization. The current density values are with respect to the geometrical area.

and high potentials after the accelerated test cycling [82].

The Pd-based catalysts also have been reported for their durability. Despite Pd metal possesses high activity for the ORR, the Pd-based catalysts have poor stability and durability because Pd is easily dissolved in an acidic electrolyte for PEFCs. As one of the methods to improve the durability of Pd-based catalysts, alloying with certain elements thus has been suggested [83]. Some researches including Pd-Mo, Pd-Co-Mo, Pd-Ti, Pd-

21

Co-Au have reported that alloying Pd with another metal results in the improved stability [84–86]. Figure 1.10 shows a stability assessment for Pd-Co-Mo catalysts by recording the cell voltage with time (Fig. 1.10a) and the polarization curves before and after polarizing the fuel cell at a constant current density of 200 mA cm^{-2} for 80 h (Fig. 1.10b). The cell exhibits stable voltage within this test period (Fig. 1.10a) without any difference in the curves before and after polarizing the cell (Fig. 1.10b), indicating excellent stability for the Pd-Co-Mo catalysts [85].

1.5 Objectives and approach of thesis

The objective of this thesis is to develop new cathode electrocatalyst technologies that are able to improve the performance and durability of PEFCs with reducing the Pt loading. To achieve the objective of this thesis, a new strategy was required. Our new strategies are related to development of support materials for Pt or Pt-alloy catalysts and non-Pt metal catalysts. Figure 1.11 shows the individual research area of this thesis.

To reduce the Pt loading, we firstly focused on Pt-based alloy catalysts due to their excellent catalytic activity toward ORR when compared to pure Pt catalysts [87]. The Pt-based alloy catalysts should be treated at high temperatures for the enhancement of their alloying degree, which leads to aggregation of the alloy particles due to weak interaction between carbon black and alloy particles. Thus, we investigated many carbon materials such as carbon nanotubes (CNTs) and carbon nanofibers (CNFs) as a new support for Pt-based alloy catalysts, which should be capable of stabilization of metal particles during the treatment of the catalysts at high temperatures. We chose the fishbone-typed CNFs, which possess high mechanical and chemical stability, and high surface area, due to the
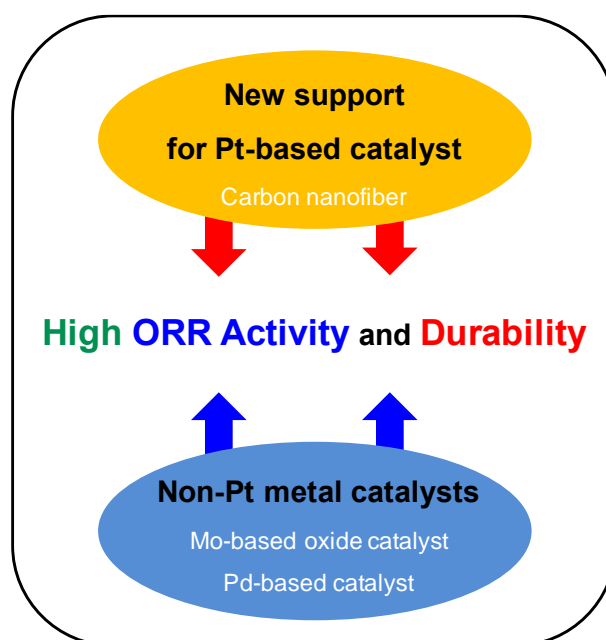
Fig. 1.11 Research topic of cathode catalysts for PEFCs.

higher yields and metal dispersion compared to CNTs [88,89]. To utilize the CNFs as the support for the Pt-based alloy catalysts, the CNFs are usually treated with oxidants because the surface of the CNFs is chemically inert. Oxygen- containing functional groups such as –COOH and –OH are introduced by the treatment with oxidants. However, the functional groups on the CNF surfaces are easily decomposed at high temperatures [90]. Thus, we considered the formation of porous structures in the CNFs which are capable of anchoring metal particles in the pores by using the treatment for elongated period of the CNFs with concentrated HNO_3. It was expected that the introduction of porous structures in the CNF supports, which is attributed to continuous carbon oxidation on the CNFs, inhibits the migration of metal nanoparticles on the surface of the CNFs at high temperatures. In addition, we thought that the Pt-based alloy catalysts with high tolerance to sintering of alloy nanoparticles can show the higher activity for the ORR compared to carbon black-supported Pt-based catalysts.

23

Secondly, we studied on metal-based oxide catalysts without Pt metal in chapter 3. Non-Pt catalysts have problem for the ease of metal dissolution under severe cathode conditions including low pH, high potential, and oxygen atmosphere, which result in low ORR activity. We investigated non-Pt metal oxide catalysts with high catalytic activity for the ORR under the harsh cathode conditions. Mo-based catalysts including Mo oxides and Mo nitrides have been reported to be an attractive catalyst toward the ORR because they facilitate dissociation of the oxygen molecule, which leads to the higher ORR activity [91,92]. Thus, this Mo-based catalyst was chosen as a non-Pt catalyst and modified with many transition metals to improve their catalytic activity for the ORR. Carbon black which is usually used was selected as a support for the Mo-based catalysts due to its high surface area. In addition, the preparation of Mo-based catalysts in our study did not require the treatment at high temperatures. Thus, we used conventional carbon support, carbon black. We also used Mo-based heteropolyacids (HPAs) as main Mo precursors, including $H_3PMo_{12}O_{40}$ and $H_4SiMo_{12}O_{40}$ due to their multi-electron reduction and oxidation (redox) ability which led to excellent catalytic activity for the ORR. Thus, we tried to prepare Mo-based oxide catalysts with addition of another transition metal by using the Mo-based HPAs as the Mo precursors. We expected that the Mo-based oxide catalysts are stable in acidic electrolyte and show excellent ORR activity which is attributed to metal redox ability at the cathode.

Finally, we studied silica-coated Pd-based catalysts as non-Pt catalysts in chapter 4. Pd is less expensive than Pt and has the higher ORR activity than other non-Pt metals. However, pure Pd catalysts have low activity for the ORR and durability under cathode conditions. Thus, we focused on development of the active and durable Pd-based catalysts. We modified the pure Pd metal with transition metals to improve ORR activity [93,94].

24

A carbon black also was chosen as a support for the Pd-based catalysts due to their high surface area. As demonstrated in chapter 4, we could develop the preparation method of Pd-based alloys with high alloying degree at low temperatures. Thus, we could use a conventional carbon support, carbon black. These Pd-based catalysts were prepared by reduction of $NaBH_4$ in EG solution without heat-treatment leading to aggregation of the metal particles. Thus, we expected that the Pd-based catalysts have small alloy nanoparticles and high activity for the ORR. In addition, the Pd-based catalysts with the highest ORR activity were covered with silica layers to improve their durability. It was expected that the durability of Pd-based catalysts will be enhanced by silica-coating on the metals when the silica layers are the optimal thickness.

1.6 Thesis outline

Chapter 1 consists of an introduction to fundamentals and challenges of polymer electrolyte fuel cell (PEFC) and cathode catalysts, as well as advances in cathode catalyst. In addition, the thesis objectives are given in this chapter.

Chapter 2 describes study on the development of carbon nanofiber (CNF) used as catalytic supports for Pt or Pt-Co alloy nanoparticles. We prepared CNFs used as the supports for Pt or Pt-Co alloy nanoparticles, which can inhibit the sintering of Pt metal particles during alloy formation at high temperatures. In this chapter, we report the structural properties and excellent performances of the CNF supports for the stabilization of precious metal particles.

Chapter 3 describes the study on the ORR activity of carbon black-supported vanadium-molybdenum oxides (V-MoO$_x$/CB) catalysts for the cathode in the PEFCs. We prepared Mo-based catalysts with V cation from heteropolyacids (HPAs) as the metal oxide precursors due to their ability for reduction-oxidation reaction (redox). In this chapter, we report the activity for the ORR for the optimized V-MoO$_x$/CB catalysts as cheap non-Pt catalysts.

Chapter 4 describes the study on carbon black-supported palladium-silver (Pd-Ag/CB) catalysts with silica-coating layers as active and durable cathode catalysts for PEFCs. We developed highly active Pd-Ag/CB catalysts and then covered their catalysts with silica layers to improve their durability under the cathode conditions. In this chapter, we report the catalytic activity of the Pd-Ag/CB catalysts including for the ORR during durability test and the effects of silica-coating on their durability.

Chapter 5 provides overall conclusions which summarize the results of this study.

References

[1]   S. Sharma, B.G. Pollet, J. Power Sources 208 (2012) 96–119.

[2]   X. Zhou, Y. Gan, J. Du, D. Tian, R. Zhang, C. Yang, Z. Dai, J. Power Sources 232 (2013) 310–322.

[3]   S. Thiele, T. Fürstenhaupt, D. Banham, T. Hutzenlaub, V. Birss, C. Ziegler, R. Zengerle, J. Power Sources 228 (2013) 185–192.

[4]   S. Shahgaldi, J. Hamelin, Carbon N. Y. 94 (2015) 705–728.

[5]   M. Shao, Q. Chang, J.-P. Dodelet, R. Chenitz, Chem. Rev. 116 (2016) 3594–3657.

[6]   J. Larminie, A. Dicks, Fuel Cell Systems Explained: Second Edition, 2003.

[7]   M.M. Hussain, J.J. Baschuk, X. Li, I. Dincer, Int. J. Therm. Sci. 44 (2005) 903–911.

[8]   J. Mehta, V., Cooper, J. Power Sources 114 (2003) 32–53.

[9]   C. Rayment, S. Sherwin, Introduction to Fuel Cell Technology, Notre Dame, IN 46556, U.S.A., 2003.

[10]   C. Song, J. Zhang, in:, J. Zhang (Ed.), PEM Fuel Cell Electrocatal. Catal. Layers, Springer London, London, 2008, pp. 89–134.

[11]   DH. Lim, J. Wilcox, J. Phys. Chem. C 116 (2012) 3653–3660.

[12]   S. Sui, X. Wang, X. Zhou, Y. Su, S. Riffat, C. Liu, J. Mater. Chem. A 5 (2017) 1808–1825.

[13]   O.T. Holton, J.W. Stevenson, Platin. Met. Rev. 57 (2013) 259–271.

[14]   M.E. Scofield, H. Liu, S.S. Wong, Chem. Soc. Rev. 44 (2015) 5836–5860.

[15]   R. Borup, J. Meyers, B. Pivovar, Y.S. Kim, R. Mukundan, N. Garland, D. Myers, M. Wilson, F. Garzon, D. Wood, P. Zelenay, K. More, K. Stroh, T. Zawodzinski, J. Boncella, J.E. McGrath, M. Inaba, K. Miyatake, M. Hori, K. Ota, Z. Ogumi, S. Miyata, A. Nishikata, Z. Siroma, Y. Uchimoto, K. Yasuda, K. Kimijima, N. Iwashita, Chem. Rev. 107 (2007) 3904–3951.

[16]   Y. Li, K. Moriyama, W. Gu, S. Arisetty, C.Y. Wang, J. Electrochem. Soc. 162 (2015) F834–F842.

[17]   P.J. Ferreira, G.J. la O', Y. Shao-Horn, D. Morgan, R. Makharia, S. Kocha, H.A. Gasteiger, J. Electrochem. Soc. 152 (2005) A2256.

[18]   J.C. Meier, C. Galeano, I. Katsounaros, J. Witte, H.J. Bongard, A.A. Topalov, C. Baldizzone, S. Mezzavilla, F. Schüth, K.J.J. Mayrhofer, Beilstein J. Nanotechnol.

5 (2014) 44–67.

[19] T. Akita, A. Taniguchi, J. Maekawa, Z. Siroma, K. Tanaka, M. Kohyama, K. Yasuda, J. Power Sources 159 (2006) 461–467.

[20] K. Yasuda, A. Taniguchi, T. Akita, T. Ioroi, Z. Siroma, Phys. Chem. Chem. Phys. 8 (2006) 746–752.

[21] J.C. Meier, C. Galeano, I. Katsounaros, A.A. Topalov, A. Kostka, F. Schüth, K.J.J. Mayrhofer, ACS Catal. 2 (2012) 832–843.

[22] A. Wilson, J. Marcinkoski, D. Papageorgopoulos, R. Ahluwalia, B. James, C. Houchins, J. Huya-Kouadio, DOE Hydrogen and Fuel Cells Program Record Title: Fuel Cell System Cost -2016 Originator, 2016.

[23] Johnson Matthey (http://www.matthey.com).

[24] J. Greeley, I.E.L. Stephens, A.S. Bondarenko, T.P. Johansson, H.A. Hansen, T.F. Jaramillo, J. Rossmeisl, I. Chorkendorff, J.K. Nørskov, Nat. Chem. 1 (2009) 552–556.

[25] Q. Huang, H. Yang, Y. Tang, T. Lu, D.L. Akins, Electrochem. Commun. 8 (2006) 1220–1224.

[26] A. Bonakdarpour, K. Stevens, G.D. Vernstrom, R. Atanasoski, A.K. Schmoeckel, M.K. Debe, J.R. Dahn, Electrochim. Acta 53 (2007) 688–694.

[27] H. Yang, W. Vogel, C. Lamy, J. Phys. Chem. B 108 (2004) 11024–11034.

[28] A. Stassi, C. D'urso, V. Baglio, A. Di Blasi, V. Antonucci, A.S. Arico, A.M. Castro Luna, A. Bonesi, W.E. Triaca, J. Appl. Electrochem. 36 (2006) 1143–1149.

[29] D. Banham, S. Ye, ACS Energy Lett. 2 (2017) 629–638.

[30] S. Mukerjee, S. Srinivasan, M.P. Soriaga, J. McBreen, J. Electrochem. Soc. 142 (1995) 1409–1422.

[31]   D. Wang, H.L. Xin, R. Hovden, H. Wang, Y. Yu, D.A. Muller, F.J. DiSalvo, H.D. Abruña, Nat. Mater. 12 (2012) 81–87.

[32]   V.R. Stamenkovic, B. Fowler, B.S. Mun, G. Wang, P.N. Ross, C.A. Lucas, N.M. Markovic, Science (80-.). 315 (2007) 493–497.

[33]   C. Chen, Y. Kang, Z. Huo, Z. Zhu, W. Huang, H.L. Xin, J.D. Snyder, D. Li, J.A. Herron, M. Mavrikakis, M. Chi, K.L. More, Y. Li, N.M. Markovic, G.A. Somorjai, P. Yang, V.R. Stamenkovic, Science (80-.). 343 (2014) 1339–1343.

[34]   L. Du, Y. Shao, J. Sun, G. Yin, J. Liu, Y. Wang, Nano Energy 29 (2016) 314–322.

[35]   Y. Li, Y. Li, E. Zhu, T. McLouth, C.-Y. Chiu, X. Huang, Y. Huang, J. Am. Chem. Soc. 134 (2012) 12326–12329.

[36]   D. Sebastián, A.G. Ruíz, I. Suelves, R. Moliner, M.J. Lázaro, V. Baglio, A. Stassi, A.S. Aricò, Appl. Catal. B Environ. 115–116 (2012) 269–275.

[37]   L. Yang, S. Jiang, Y. Zhao, L. Zhu, S. Chen, X. Wang, Q. Wu, J. Ma, Y. Ma, Z. Hu, Angew. Chemie 123 (2011) 7270–7273.

[38]   Y. Shao, J. Sui, G. Yin, Y. Gao, Appl. Catal. B Environ. 79 (2008) 89–99.

[39]   E. Antolini, E.R. Gonzalez, Solid State Ionics 180 (2009) 746–763.

[40]   L. Zhang, K. Lee, J. Zhang, Electrochim. Acta 52 (2007) 3088–3094.

[41]   S.M. Andersen, M. Borghei, P. Lund, Y.R. Elina, A. Pasanen, E. Kauppinen, V. Ruiz, P. Kauranen, E.M. Skou, Solid State Ionics 231 (2013) 94–101.

[42]   S. Guo, S. Sun, J. Am. Chem. Soc. 134 (2012) 2492–2495.

[43]   Z. Yang, I. Moriguchi, N. Nakashima, ACS Appl. Mater. Interfaces 7 (2015) 9800–9806.

[44]   B. Seger, P. V. Kamat, J. Phys. Chem. C 113 (2009) 7990–7995.

[45]   Y.-J. Wang, B. Fang, H. Li, X.T. Bi, H. Wang, Prog. Mater. Sci. 82 (2016) 445–

498.

[46] S. Iijima, Phys. B Condens. Matter 323 (2002) 1–5.

[47] H.Y. Cheng, Y.A. Zhu, Z.J. Sui, X.G. Zhou, D. Chen, Carbon N. Y. 50 (2012) 4359–4372.

[48] K. Lee, J. Zhang, H. Wang, D.P. Wilkinson, J. Appl. Electrochem. 36 (2006) 507–522.

[49] D. He, C. Zeng, C. Xu, N. Cheng, H. Li, S. Mu, M. Pan, Langmuir 27 (2011) 5582–5588.

[50] A. Guha, W. Lu, T.A. Zawodzinski, D.A. Schiraldi, Carbon N. Y. 45 (2007) 1506–1517.

[51] A. Guha, T.A. Zawodzinski, D.A. Schiraldi, J. Power Sources 172 (2007) 530–541.

[52] S. Zhang, Y. Shao, G. Yin, Y. Lin, Appl. Catal. B Environ. 102 (2011) 372–377.

[53] S. Yin, S. Mu, H. Lv, N. Cheng, M. Pan, Z. Fu, Appl. Catal. B Environ. 93 (2010) 233–240.

[54] M. Nie, P.K. Shen, Z. Wei, J. Power Sources 167 (2007) 69–73.

[55] JH. Kim, A. Ishihara, S. Mitsushima, N. Kamiya, K. Ota, Electrochim. Acta 52 (2007) 2492–2497.

[56] SY. Huang, P. Ganesan, S. Park, B.N. Popov, J. Am. Chem. Soc. 131 (2009) 13898–13899.

[57] S. Kondo, M. Nakamura, N. Maki, N. Hoshi, J. Phys. Chem. C 113 (2009) 12625–12628.

[58] L. Liu, G. Samjeske, S. Nagamatsu, O. Sekizawa, K. Nagasawa, S. Takao, Y. Imaizumi, T. Yamamoto, T. Uruga, Y. Iwasawa, Top. Catal. 57 (2014) 595–606.

[59]   H. Erikson, A. Sarapuu, J. Kozlova, L. Matisen, V. Sammelselg, K. Tammeveski, Electrocatalysis 6 (2015) 77–85.

[60]   G. Bampos, S. Bebelis, D.I. Kondarides, X. Verykios, Top. Catal. 0 (2017) 0.

[61]   Y. Feng, T. He, N. Alonso-Vante, Chem. Mater. 20 (2008) 26–28.

[62]   H. Wang, Y. Liang, Y. Li, H. Dai, Angew. Chemie - Int. Ed. 50 (2011) 10969–10972.

[63]   K. Lee, L. Zhang, J. Zhang, Electrochem. Commun. 9 (2007) 1704–1708.

[64]   M. Kourasi, R.G.A. Wills, A.A. Shah, F.C. Walsh, Electrochim. Acta 127 (2014) 454–466.

[65]   R.J. Stanis, M.C. Kuo, A.J. Rickett, J.A. Turner, A.M. Herring, Electrochim. Acta 53 (2008) 8277–8286.

[66]   R. Othman, A.L. Dicks, Z. Zhu, Int. J. Hydrogen Energy 37 (2012) 357–372.

[67]   M. Lefèvre, E. Proietti, F. Jaouen, J.P. Dodelet, Science 324 (2009) 71–74.

[68]   Y. Liu, A. Ishihara, S. Mitsushima, N. Kamiya, K. Ota, J. Electrochem. Soc. 154 (2007) B664.

[69]   K. Ota, Y. Ohgi, K.-D. Nam, K. Matsuzawa, S. Mitsushima, A. Ishihara, J. Power Sources 196 (2011) 5256–5263.

[70]   M. Chisaka, A. Ishihara, H. Morioka, T. Nagai, S. Yin, Y. Ohgi, K. Matsuzawa, S. Mitsushima, K. Ota, ACS Omega 2 (2017) 678–684.

[71]   Y. Shao, G. Yin, Y. Gao, J. Power Sources 171 (2007) 558–566.

[72]   H. Matsumori, S. Takenaka, H. Matsune, M. Kishida, Appl. Catal. A Gen. 373 (2010) 176–185.

[73]   S. Takenaka, N. Susuki, H. Miyamoto, E. Tanabe, H. Matsune, M. Kishida, Chem. Commun. 46 (2010) 8950.

[74] S. Takenaka, H. Matsumori, H. Matsune, M. Kishida, Appl. Catal. A Gen. 409–410 (2011) 248–256.

[75] S. Takenaka, H. Miyamoto, Y. Utsunomiya, H. Matsune, M. Kishida, J. Phys. Chem. C 118 (2014) 774–783.

[76] A. Seo, J. Lee, K. Han, H. Kim, Electrochim. Acta 52 (2006) 1603–1611.

[77] G. Liu, H. Zhang, H. Zhong, J. Hu, D. Xu, Z. Shao, Electrochim. Acta 51 (2006) 5710–5714.

[78] Z. Wei, H. Guo, Z. Tang, J. Power Sources 62 (1996) 233–236.

[79] J. Zhang, K. Sasaki, E. Sutter, R.R. Adzic, Science (80-.). 315 (2007) 220–222.

[80] F. Ando, T. Tanabe, T. Gunji, T. Tsuda, S. Kaneko, T. Takeda, T. Ohsaka, F. Matsumoto, Electrochim. Acta 232 (2017) 404–413.

[81] D. Banham, S. Ye, K. Pei, J. Ozaki, T. Kishimoto, Y. Imashiro, J. Power Sources 285 (2015) 334–348.

[82] H. Peng, Z. Mo, S. Liao, H. Liang, L. Yang, F. Luo, H. Song, Y. Zhong, B. Zhang, Sci. Rep. 3 (2013) 1765.

[83] M. Shao, J. Power Sources 196 (2011) 2433–2444.

[84] A. Sarkar, A. V. Murugan, A. Manthiram, J. Phys. Chem. C 112 (2008) 12037–12043.

[85] V. Raghuveer, A. Manthiram, A.J. Bard, J. Phys. Chem. B 109 (2005) 22909–22912.

[86] J.L. Fernández, V. Raghuveer, A. Manthiram, A.J. Bard, J. Am. Chem. Soc. 127 (2005) 13100–13101.

[87] X. Yu, S. Ye, J. Power Sources 172 (2007) 133–144.

[88] S. Takenaka, Y. Shigeta, E. Tanabe, K. Otsuka, J. Catal. 220 (2003) 468–477.

[89]   S. Takenaka, S. Kobayashi, H. Ogihara, K. Otsuka, J. Catal. 217 (2003) 79–87.

[90]   L. Calvillo, M. Gangeri, S. Perathoner, G. Centi, R. Moliner, M.J. Lázaro, J. Power Sources 192 (2009) 144–150.

[91]   H. Zhong, H. Zhang, G. Liu, Y. Liang, J. Hu, B. Yi, Electrochem. Commun. 8 (2006) 707–712.

[92]   J. Qi, L. Jiang, Q. Jiang, S. Wang, G. Sun, J. Phys. Chem. C 114 (2010) 18159–18166.

[93]   S. Takenaka, T. Tsukamoto, H. Matsune, M. Kishida, Catal. Sci. Technol. 3 (2013) 2723.

[94]   M. Shao, K. Sasaki, R.R. Adzic, J. Am. Chem. Soc. 128 (2006) 3526–3527.

Chapter 2

Development of carbon nanofiber with high tolerance to sintering as a support for Pt-based catalysts

2.1 Introduction

Precious metals such as Pt, Rh and Ru supported on carbon materials are widely used as active catalysts for various reactions. Pt metal supported on carbon black has been utilized as an electrocatalyst at the cathode for the oxygen reduction reaction (ORR), and utilized as an electrocatalyst at the anode for the hydrogen oxidation reaction in polymer electrolyte fuel cells (PEFCs). Pd, Pt or Ru catalysts supported on activated carbons catalyze the hydrogenation of ketones and aldehydes to form alcohols. Reducing the precious metal loading without compromising the catalytic activity is an important requirement because of the high cost of such precious metals and their limited resource. The catalytic performance of precious metals supported on carbon materials strongly depends on the morphology and surface structure of the carbon materials [1-4]. Recently, one-dimensional carbon materials such as carbon nanotubes (CNTs) and carbon nanofibers (CNFs) have been utilized as supports for precious metals [5-7]. Pt catalysts supported on CNTs and CNFs show a higher activity toward ORR when compared to Pt catalysts supported on carbon black, which are used in state of the art PEFCs [7-12]. The catalytic performance of Pt metal supported on CNTs and CNFs is enhanced by the interaction between the Pt metal and these carbon nanostructures. An additional benefit

of CNTs and CNFs as electrocatalyst supports is their potential to improve the electron conductivity and mass transport. Their one-dimensional structures allow effective fuel and oxidant access to the densely scattered triple phase boundaries. Thus, the use of CNTs and CNFs as supports has the potential to reduce precious metal loading in the catalysts. Precious metals supported on CNTs and CNFs also show a specific catalytic performance for the hydrogenation of α, β-unsaturated aldehydes such as cinnamaldehyde [13-16]. Pt or Pd catalysts supported on CNTs and CNFs catalyze the selective hydrogenation of α, β-unsaturated aldehydes to unsaturated alcohols, whereas saturated alcohols and aldehydes are inevitably formed on these metal catalysts supported on conventional carriers such as activated carbon, silica and alumina.

CNTs and CNFs can be formed by catalytic chemical vapor deposition [17-19]. Reactant molecules, such as CO, hydrocarbons and alcohols as carbon sources, are contacted with Fe, Co or Ni metal catalysts at high temperatures, to form CNTs and CNFs. The yields of CNTs and CNFs strongly depend on the reaction conditions such as the type of catalysts and reactant molecules, and reaction temperatures [20-22]. Nonetheless, the yields of CNFs are extremely higher than that of CNTs [23,24]. Thus, CNFs are promising supports for precious metals. CNFs formed by catalytic chemical vapor deposition are one of the fishbone-typed CNFs, meaning that graphene sheets are oriented at a uniform angle to the central axis of the nanofibers [17]. The edges of stacked graphene sheets form the outer walls of the CNFs. When metal particles are supported on the outer surfaces of the CNFs, exposed graphite edges on the CNF surfaces are interacted with the metals, which leads to the specific catalytic performances [25]. However, it is difficult to highly disperse metal particles on the surfaces of CNFs because the property of CNF surfaces is chemically inert. Thus, CNFs are usually pre-treated with oxidants such as gaseous

oxygen, and oxidizing acid solutions such as aqueous HNO_3 and aqueous mixtures of HNO_3 and H_2SO_4, before the metal particles are supported on the CNFs [26-29]. The treatment of the CNFs with these oxidants led to the formation of oxygen-containing functional groups such as −COOH and −OH. The functional groups on the surface of the CNFs work as anchoring sites for the precious metal particles when introducing the metal phase. However, the functional groups on the CNF surfaces are easily decomposed at high temperatures [30,31]. Thus, the CNF supports with oxygen-containing functional groups cannot stabilize metal nanoparticles at high temperatures. It is expected that the introduction of porous structures in the CNF supports prevents the migration of metal nanoparticles on the CNFs at high temperatures and improves the tolerance to sintering of metal nanoparticles.

Precious metal-based alloy catalysts supported on carbon materials also show excellent catalytic performance. For example, Pt-based alloys such as Pt-Co, Pt-Ni and Pt-Pd show excellent catalytic activity toward ORR, when these alloys are used as cathode catalysts in PEFCs [32-34]. Pd-Ni alloy catalysts supported on CNFs have high activity and long life for the methane decomposition to form hydrogen and CNFs [24]. The preparation of the alloy catalysts usually requires the treatment of the catalysts at high temperatures for the improvement of their alloying degree, which causes aggregation of the alloy particles [35-37]. Therefore, the sintering of metal nanoparticles supported on CNFs at high temperatures should be inhibited for the preparation of highly active alloy catalysts.

In the present study, CNFs formed from methane decomposition over silica-supported Ni catalysts were used as supports for Pt metal and Pt-based alloys. It was found that the treatment of the CNFs with concentrated HNO_3 for elongated periods brought about the

formation of porous structures in the CNFs in addition to the introduction of oxygen-containing functional groups on the CNFs. The porous structures in the CNFs inhibited the sintering of Pt metal particles when the CNFs were used as supports. Nanosized Pt-based alloy particles could be thus prepared on the CNF supports even after treatment of the catalysts at high temperatures. The Pt-based alloy catalysts supported on the CNFs showed a high activity toward ORR. Herein, we report the excellent performances of the CNF supports for the stabilization of precious metal particles.

2.2 Experimental

2.2.1 Formation of CNFs

CNFs were formed by methane decomposition over silica-supported Ni (Ni/SiO$_2$) catalysts [38]. SiO$_2$ (Cab-O-Sil, supplied from CABOT) was impregnated into aqueous Ni(NO$_3$)$_2$ and dried at 353 K in air. The samples thus obtained were calcined at 773 K in air for 5 h. The loading of Ni in the catalysts was adjusted to be 20 wt% as Ni metal. The Ni/SiO$_2$ catalysts (0.20 g) were placed in a quartz-fixed bed reactor and then reduced in a stream of hydrogen (P=20.0 kPa) diluted with Ar gas at 773 K prior to the methane decomposition. The reduced Ni/SiO$_2$ catalysts were contacted with methane (flow rate = 100 mL min^{-1}, P=101.3 kPa) at 823 K for 10 h. Carbon nanofibers of ca. 9.0 g were obtained by methane decomposition over the Ni/SiO$_2$ catalysts.

The CNFs were dispersed and stirred in an aqueous HCl solution (3.0 M) at 363 K for 20 h in order to remove Ni metal. The CNFs were further treated in concentrated HNO$_3$ (60 %) at 393 K for 14 h. After filtration, the samples thus obtained were thoroughly washed with distilled water several times. The CNFs treated with HNO$_3$ were

37

denoted as CNF(HNO$_3$), whereas the CNFs before the treatment with HNO$_3$ (just after washing with aqueous HCl) was denoted as CNF(HCl).

2.2.2 Preparation of supported Pt catalysts

Pt catalysts supported on carbon supports were prepared using a conventional impregnation method. CNF(HCl) or CNF(HNO$_3$) was impregnated into tetrahydrofuran (THF) containing H$_2$PtCl$_6$ and dried at 333 K. The loading of Pt metal in these catalysts was adjusted to 15 wt%. The dried samples were reduced with hydrogen (P = 10.0 kPa, diluted with Ar) at 573 K for 2 h. The Pt catalysts were further treated with hydrogen (P = 10.0 kPa, diluted with Ar) at 973 K for 3 h in order to examine the tolerance to sintering of Pt metal particles. Carbon black (denoted as CB, Vulcan XC-72 supplied from CABOT) was also used as a support of Pt for comparison.

Supported Pt-Co alloy catalysts were prepared by impregnation of these Pt catalysts into THF containing Co(NO$_3$)$_2$. The Pt catalysts supported on CNF(HCl), CNF(HNO$_3$) or CB were impregnated into THF containing Co(NO$_3$)$_2$. The amount of Co dissolved in the solution was such that the molar ratio of Co to Pt in the catalysts was equal to 1/1. After drying, the samples were reduced with hydrogen at 573 K and further treated at 1073 K for 3 h in Ar to allow for the formation of Pt-Co alloys.

CNF(HCl), CNF(HNO$_3$) or CB was also impregnated into diphenyl ether containing Pt(II) acetylacetonate (denoted as Pt(acac)$_2$). The amount of Pt(acac)$_2$ dissolved in the solution was such that the nominal loading of Pt metal in the catalysts was 40 wt%. These carbon materials were refluxed in the solutions at 443 K for 10 h in N$_2$ atmosphere. After filtration of the solutions, the samples were reduced with hydrogen at 773 K for 2 h. The Pt catalysts were further treated with hydrogen (P = 10.0 kPa, diluted with Ar) at 973 K

38

for 2 h in order to examine the tolerance to sintering of Pt metal particles.

2.2.3 Characterization of Pt-based catalysts

The morphology of the samples was examined by transmission electron microscopy (TEM). TEM images of the samples were recorded with a JEOL JEM-3000F instrument. Specimens were prepared by ultrasonically suspending the samples in 2-propanol. A drop of the suspension was deposited on a carbon-enhanced copper grid and dried in air.

X-ray powder diffraction (XRD) was used to identify crystallized metal species in the catalysts. XRD data were collected at room temperature on a Rigaku Ultima IV diffractometer using CuKα radiation (λ=1.5418 Å).

Raman spectra for carbon samples were measured at room temperature under ambient conditions on a JASCO NRS-3100 spectrometer (excitation wavelength = 532 nm, laser power = 2 mW at the sample position).

Nitrogen adsorption/desorption isotherms were measured at 77 K using a BELSORP-max (BEL Japan, Inc.) to examine the surface area and pore structure of the carbon samples. The specific surface area of the samples was calculated using the Brunauer-Emmett-Teller (BET) equation, and pore size distributions were determined by the Barrett-Joyner-Halenda (BJH) method using the desorption branch. Before measurement of the nitrogen adsorption, the samples were degassed at 573 K for 5 h.

Thermogravimetric analysis was performed on a Shimadzu DTG60 instrument for determining the metal loading on the carbon supports. Typical samples of weight 0.010 g in a platinum pan were heated to 973 K at a rate of 5 K min^{-1} in air.

X-ray absorption near edge structure (XANES) and extended X-ray absorption fine structure (EXAFS) for the samples were measured at the Photon Factory in the Institute

of Materials Structure Science for High Energy Accelerator Research Organization, Japan (Proposal No. 2010G556). Pt L_{III}-edge XANES/EXAFS spectra of the Pt-Co catalysts were measured in transmission mode at room temperature at beam line BL-9C with a Si(111) two crystal monochromator. Analysis of the EXAFS spectra was performed by using the EXAFS analysis program, REX (Rigaku Co.). Fourier transformation of k^3-weighted EXAFS was performed over the k range from 4 to 16 $Å^{-1}$. Inversely Fourier transformed data for each Fourier peak were analyzed by a curve-fitting method, using phase shift and amplitude function for a Pt-Pt shell and a Pt-Co shell derived from FEFF 8.0 [39].

2.2.4 Electrochemical measurement of the catalysts

Electrochemical measurements using a rotating disk electrode (RDE) were carried out with a three-electrode electrochemical cell. Pt foil was used as a counter electrode and Ag/AgCl was used as a reference electrode. All potentials in this work are referenced to a reversible hydrogen electrode (RHE). The working electrode was composed of a 6-mm diameter glassy carbon core embedded in a Teflon cylinder. Catalyst ink was prepared by ultrasonically blending the catalysts and ethanol. This ink was deposited on a glassy carbon disk. The amount of catalyst deposited onto the glassy carbon rod was such that the Pt content was equivalent to 14 μg-Pt cm^{-2} in all experiments. After drying the catalysts at room temperature, a Nafion solution diluted with methanol was deposited onto the catalysts to fix the catalysts in place on the disk. The catalysts were immersed in 0.1 M $HClO_4$ at room temperature. The potential of the Pt-Co catalysts was repeatedly changed between 0.05 and 1.20 V in N_2-purged 0.1 M $HClO_4$ at room temperature until reproducible cyclic voltammograms (CVs) were obtained. The reproducible CVs for all
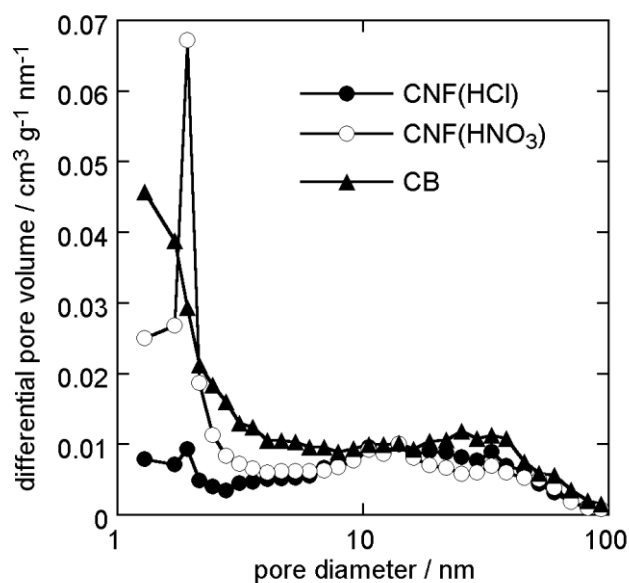
Fig. 2.1 Pore size distribution of CNF(HCl), CNF(HNO$_3$) and CB estimated by N$_2$ adsorption/desorption at 77 K.

the catalysts were obtained within 50 cycles of the potential cycling. The polarization curves for ORR on the Pt catalysts were measured in O$_2$-saturated 0.1 M HClO$_4$ at room temperature by changing the potential of the working electrode from 0.1 to 1.1 V at a scan rate of 10 mV s^{-1} with an electrode rotation rate of 1600 rpm.

2.3 Results and discussion

2.3.1 Characterization of carbon supports

Specific surface area and pore size distribution for CNF(HCl), CNF(HNO$_3$) and CB were evaluated by the adsorption and desorption of nitrogen at 77 K. Figure 2.1 shows the pore size distributions of CNF(HCl), CNF(HNO$_3$) and CB. CNF(HCl) had little porous structure as shown in Fig. 2.1. The treatment of CNF(HCl) with HNO$_3$ resulted in
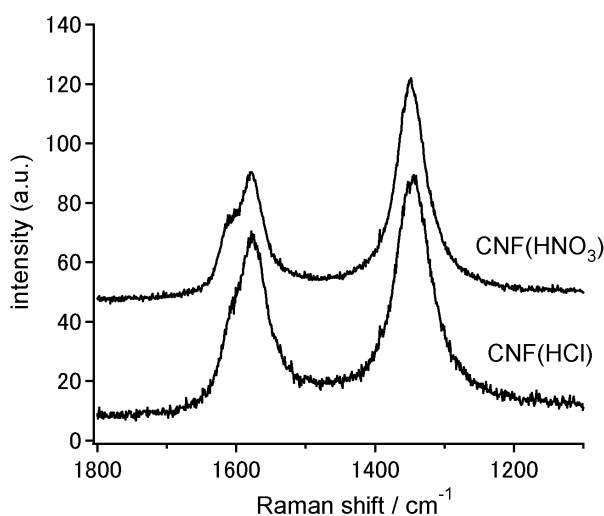
Fig. 2.2 Raman spectra of CNF(HCl) and CNF(HNO₃).

the formation of porous structures. The pore diameter in CNF(HNO$_3$) ranged from 2 to 6 nm with a maximum at around 3 nm. The treatment of CNF(HCl) with HNO$_3$ increased its surface area. The specific surface areas of CNF(HCl), CNF(HNO$_3$) and CB were evaluated to be 59, 116 and 230 m^2 g^{-1}, respectively. The surfaces of CNF(HCl) were etched with concentrated HNO$_3$ to form oxygen-containing functional groups on their surfaces. The treatment of CNF(HCl) with HNO$_3$ for elongated periods led to the further oxidation of these functional groups, which resulted in the formation of porous structures in the CNF.

Figure 2.2 shows Raman spectra of CNF(HCl) and CNF(HNO$_3$). Two strong peaks are observed at around 1360 and 1580 cm^{-1} in addition to a shoulder peak at around 1600 cm^{-1} in the Raman spectra for both samples. The peak at 1580 cm^{-1} (denoted as the G band) can be attributed to the in-plane carbon-carbon stretching vibrations of graphite layers and the peaks at 1360 cm^{-1} (denoted as the D band) were assignable to the structural imperfection of graphite [40,41]. Additionally, a shoulder peak at 1600 cm^{-1} (denoted as

42

the D' band) is also ascribed to the imperfect graphite and disordered carbon [42]. The relative peak intensity of the G band to the D band decreased after the treatment of CNF(HCl) with HNO_3. The intensity ratio of the G band to the D band (I_G/I_D) can be an index for the graphitization degree, i.e., the graphitization degree of the carbons is higher as the I_G/I_D value increases [43-45]. The I_G/I_D value for CNF(HCl) and CNF(HNO_3) was evaluated to be 0.63 and 0.50, respectively, suggesting the higher graphitization degree of CNF(HCl) compared to that of CNF(HNO_3). It is well accepted that oxygen-containing functional groups such as hydroxyl, carbonyl and carboxyl groups can be introduced onto the surfaces of carbon materials by the treatment with oxidizing acid solutions such as a concentrated HNO_3 solution and a mixed solution of HNO_3 and H_2SO_4 [26-29]. The surface atomic ratio of oxygen to carbon (O/C) in CNF(HCl) and CNF(HNO_3) was examined by X-ray photoelectron spectroscopy (XPS). The surface atomic ratio O/C for CNF(HCl) increased from 0.04 to 0.09 after the treatment with concentrated HNO_3, indicating the formation of oxygen-containing functional groups on the surface of CNF(HNO_3). The formation of functional groups on CNF(HCl) by the treatment with HNO_3 led to the decrease of its graphitization degree.

Figure 2.3 shows TEM images of CNF(HCl) and CNF(HNO_3). The diameter of CNF(HCl) ranged from 100 to 200 nm. The graphite structure can be clearly confirmed from the TEM images of CNF(HCl). The structure of CNF(HCl) was a cup-stacked one, meaning that the graphene was oriented at a uniform angle to the central axis of CNF(HCl). The diameter range of CNF(HCl) did not change appreciably after the treatment with HNO_3. However, the graphite structure of CNF(HCl) significantly changed after the treatment with HNO_3. The CNF(HNO_3) had hollow inside after the treatment with HNO_3 shown in Fig. 2.3(c and h). The surface roughness of CNF(HCl)
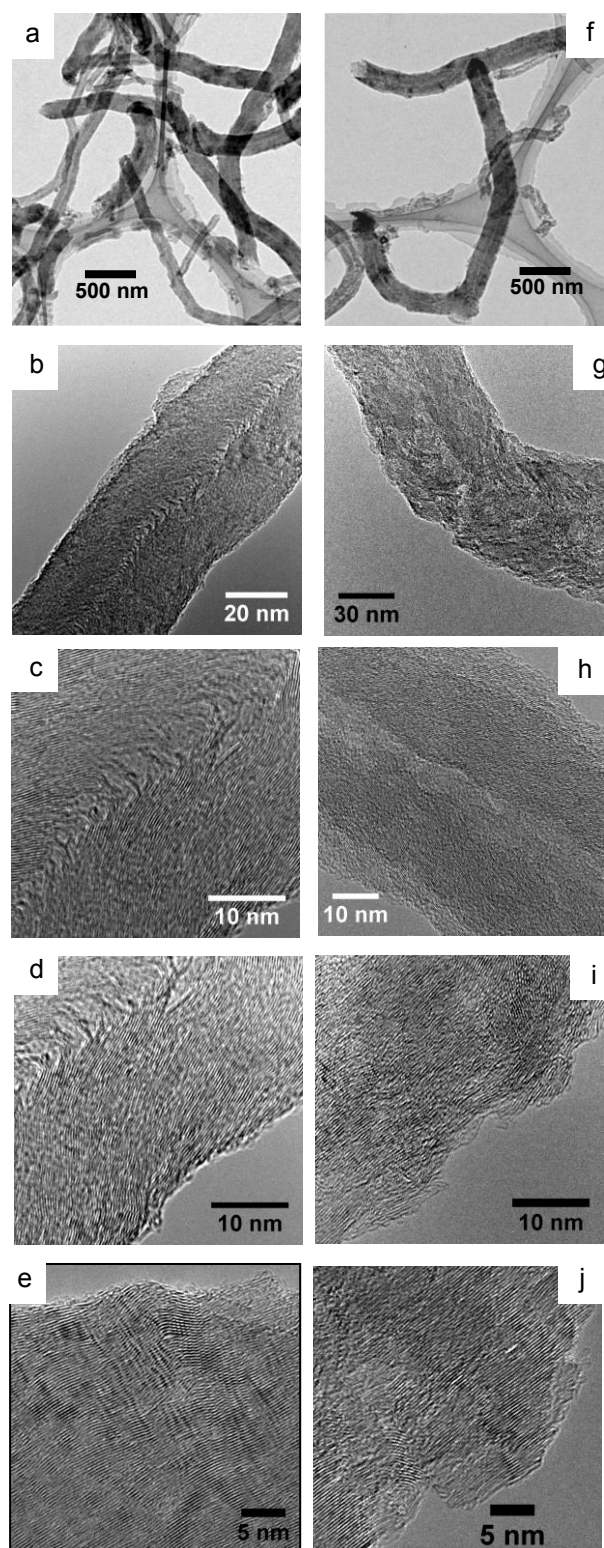
Fig. 2.3 TEM images of CNF(HCl) (a-e) and CNF(HNO₃) (f-j).

seemed to be enhanced after the treatment with HNO₃ from the high resolution TEM

44

images. In addition, dark and light spots could be found in the TEM images of CNF(HNO_3). Contrast variation in the bodies of CNF(HNO_3) showed the high density of the pores and chemically etched surfaces [46]. The graphite structure of CNF(HNO_3) was interrupted by many pores. These results strongly suggest that the surfaces and bodies of CNF(HCl) were etched with concentrated HNO_3. The carbon surfaces with low graphitization degrees in CNF(HCl) were oxidized with HNO_3 to introduce oxygen-containing functional groups such as –COOH on the CNF(HCl) surfaces. The treatment of CNF(HCl) with HNO_3 for elongated periods resulted in deep oxidation of the carbon surfaces to form CO_2, which consequently led to the formation of defects and pores on both the surface and inner of CNF(HCl).

2.3.2 Preparation of Pt catalysts supported on CNF

Pt metal particles were supported on CNF(HCl), CNF(HNO_3) and CB by the impregnation method. The Pt catalysts supported on these carbons were reduced with hydrogen at 573 K. The Pt catalysts were further treated with hydrogen at 973 K in order to clarify their tolerance to sintering of the Pt metal particles. Figure 2.4 shows representative TEM images of these Pt catalysts reduced at 573 K as well as the Pt catalysts treated at 973 K. The distribution of Pt metal particle size was evaluated based on the TEM images for each Pt catalyst. The results are shown in Fig. 2.5. Many Pt metal particles were observed in the TEM images for all of the Pt catalysts treated at 573 K. The Pt metal particle size for all of the catalysts studied ranged from 1 to 10 nm. The distribution of Pt metal particle size for Pt/CNF(HNO_3) was narrower than that for the other Pt catalysts, as shown in Fig. 2.5. The average particle size of the Pt metal for Pt/CNF(HCl), Pt/CNF(HNO_3) and Pt/CB reduced at 573 K was evaluated to be 4.2, 3.3
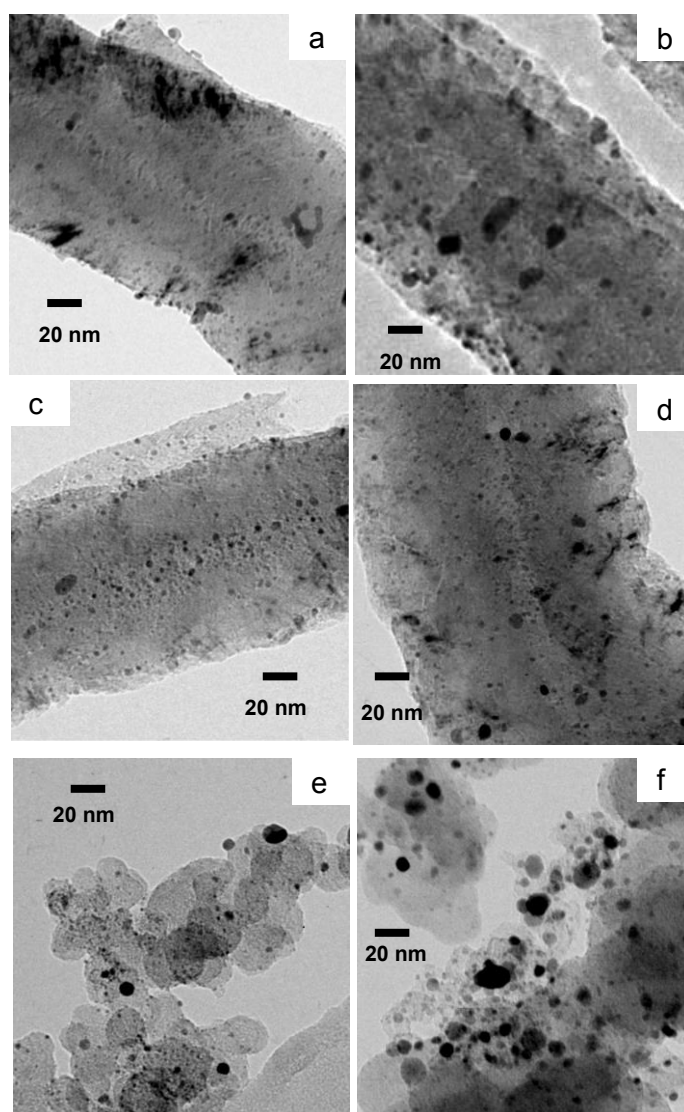
Fig. 2.4 TEM images of Pt/CNF(HCl) (a and b), Pt/CNF(HNO₃) (c and d) and Pt/CB
(e and f). a, c and e for the catalysts after the treatment at 573 K; b, d and f for
the catalysts after the treatment at 973 K.

and 3.6 nm, respectively. The Pt metal particles in these catalysts were aggregated during
the treatment at 973 K. Pt metal particles with a larger diameter than 10 nm were easily
found in the TEM image of Pt/CNF(HCl) after the treatment at 973 K. The size
distribution of Pt metal particles in Pt/CNF(HCl) was shifted toward a larger size after
the treatment at 973 K, and consequently the average size of the Pt metal particles

46
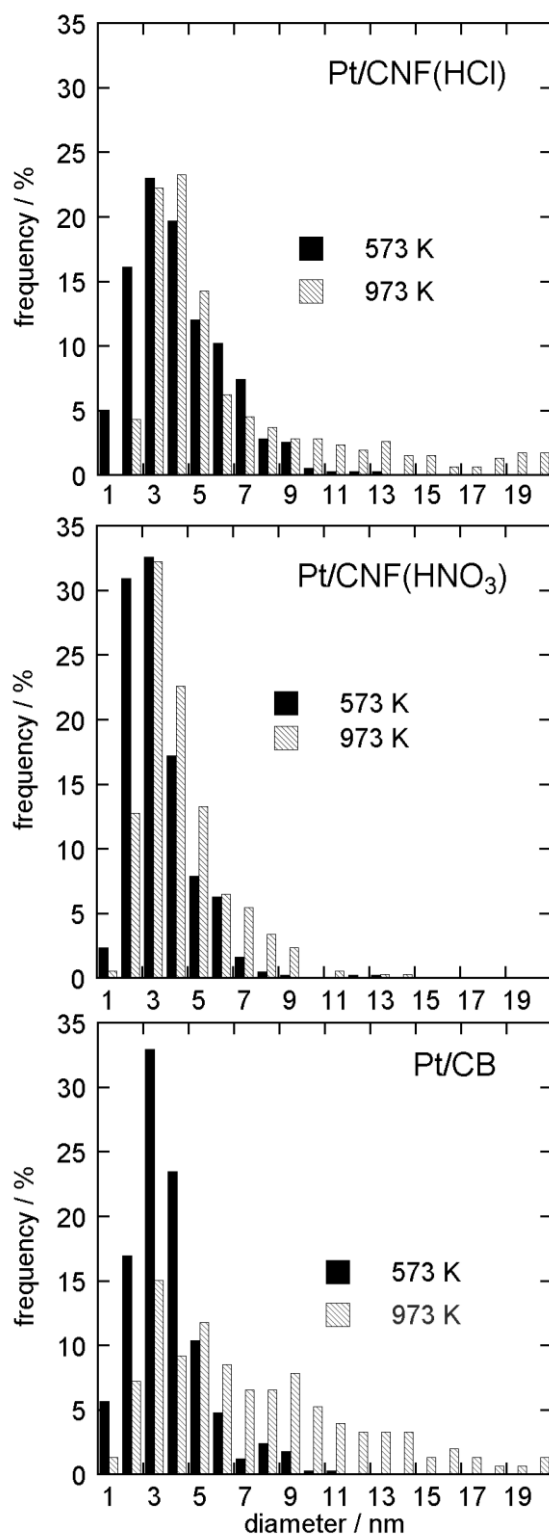
Fig. 2.5 Particle size distributions of Pt metal in Pt/CNF(HCl), Pt/CNF(HNO$_3$) and Pt/CB before and after the treatment at 973 K.

increased from 4.2 to 6.6 nm. The Pt metal particles in Pt/CB were also heavily

aggregated by their treatment at 973 K, as clarified from the TEM images (e) and (f) in Fig. 2.4. An average Pt metal particle size for the Pt/CB catalyst treated at 973 K was estimated to be 8.3 nm. In contrast, aggregated Pt metal particles were hardly found in the TEM images of Pt/CNF(HNO_3) even after the catalysts were treated at 973 K in hydrogen. The Pt metal particle size in the Pt/CNF(HNO_3) catalyst treated at 973 K ranged from 1 to 10 nm, and an average Pt particle size was evaluated to be 4.2 nm, which was smaller than that observed for the other Pt catalysts treated at 973 K. The Pt metal particles on the CNF(HNO_3) supports thus showed higher tolerance to the sintering compared to the particles on CNF(HCl) and CB. It should be noted that the surface area of CNF(HNO_3) was smaller than that of CB. The porous structures and/or functional groups in CNF(HNO_3) prevented the sintering of the Pt metal particles during the treatment at 973 K.

The high tolerance to the sintering of the Pt metal particles on CNF(HNO_3) was also confirmed by the corresponding XRD patterns. Figure 2.6 shows the XRD patterns of Pt/CNF(HCl), Pt/CNF(HNO_3) and Pt/CB after the treatment at 573 or 973 K. Diffraction lines due to Pt metal crystallites were observed at around 40 and 46 ° in the XRD patterns for all of the Pt catalysts, which could be attributed to the (111) and (200) planes of face-centered cubic (fcc) Pt metal. In addition, a diffraction line corresponding to the (002) graphitic basal plane reflection was found at around 26 ° in all of the XRD patterns shown in Fig. 2.6. The diffraction line due to graphite in the XRD patterns of Pt/CNF(HCl) and Pt/CNF(HNO_3) was sharper than that for Pt/CB, which means that the degree of graphitization of CNF(HCl) and CNF(HNO_3) was appreciably higher than that of CB. The diffraction lines due to Pt metal became sharper for all of the Pt catalysts after the treatment at 973 K. An average crystallite size of the Pt metal in the catalysts treated at
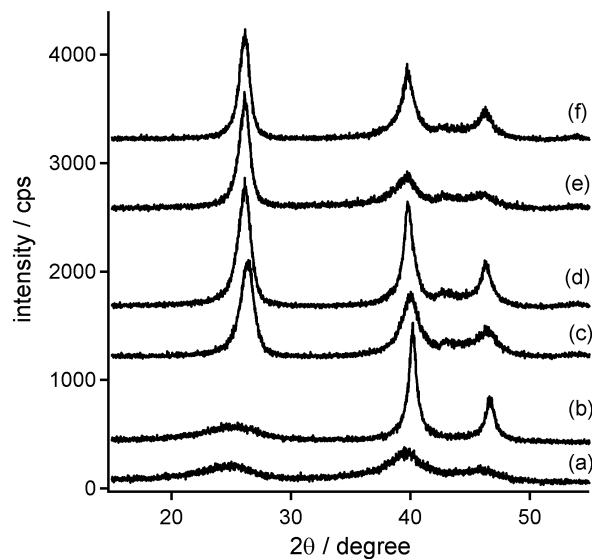
Fig. 2.6 XRD patterns of Pt/CB (a and b), Pt/CNF(HCl) (c and d) and Pt/CNF(HNO₃) (e and f) before and after the treatment at 973 K. (a), (c) and (e) for the catalysts treated at 573 K, (b), (d) and (f) for the catalysts treated at 973 K.

573 K was evaluated from the full width at half- maximum of the diffraction line using Scherrer's equation to be 5.1 nm for Pt/CNF(HCl), 3.8 nm for Pt/CNF(HNO₃) and 2.6 nm for Pt/CB. The average size of the Pt metal crystallites increased to 7.1 nm for Pt/CNF(HCl), 5.5 nm for Pt/CNF(HNO₃) and 10.1 nm for Pt/CB after the treatment at 973 K. Thus, CNF(HNO₃) supports prevent the sintering of Pt metal particles during the treatment at 973 K. As described earlier, the CNF(HNO₃) supports have pore structures and many oxygen-containing functional groups. These pores and functional groups can act as the anchorage sites of Pt metal and prevent the sintering of Pt metal particles at high temperatures. However, the functional groups on the CNF(HNO₃) support would be decomposed at high temperatures. In fact, the XPS results for the CNF(HNO₃) support showed that the surface atomic ratio of O/C decreased from 0.09 to 0.02 after the treatment of the CNF(HNO₃) support at 973 K. In contrast, the pore structure of the
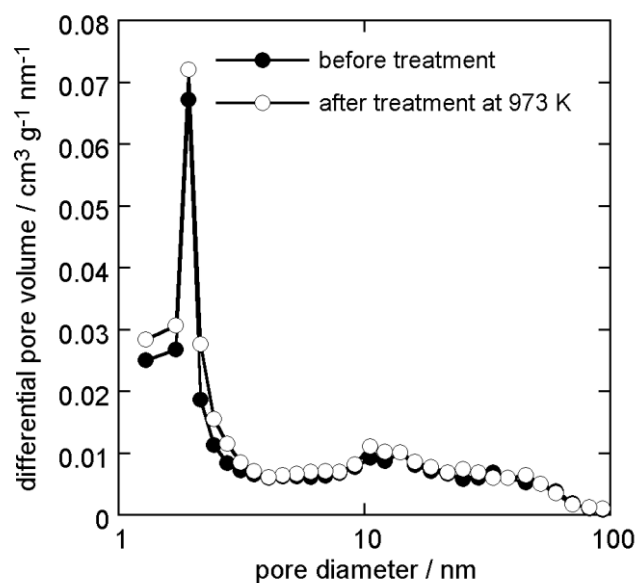
49

Fig. 2.7 Pore size distribution of CNF(HNO$_3$) before and after the treatment at 973 K.

CNF(HNO$_3$) support did not change after the treatment at 973 K. Figure 2.7 shows the pore size distribution for the CNF(HNO$_3$) support before and after the treatment at 973 K. The pore size distribution of the CNF(HNO$_3$) support treated at 973 K was similar to that of the CNF(HNO$_3$) support treated at 573 K. Thus, the pore structures in the CNF(HNO$_3$) support are effective for inhibiting the sintering of Pt metal particles at high temperatures.

A catalyst with a higher Pt loading is required for application to PEFC catalysts, because a catalyst with a lower Pt loading leads to the formation of a thick catalyst layer and a concomitantly higher mass transfer and higher electric resistance. The application of catalysts with a high loading and a high dispersion of Pt can obviate the issue related to mass transfer, water management and conductivity in the membrane-electrode-assembly (MEA) of PEFCs. Thus, a Pt/CNF(HNO$_3$) catalyst with a higher Pt loading was prepared by impregnation of CNF(HNO$_3$) into THF containing H$_2$PtCl$_6$. Figure 2.8 shows
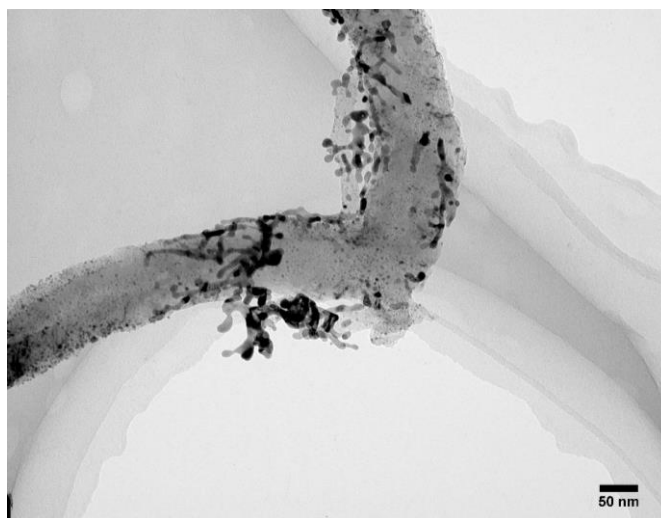
Fig. 2.8 TEM image of Pt/CNF(HNO₃) with a higher Pt loading prepared
by impregnation.

the TEM image of Pt/CNF(HNO$_3$) prepared by impregnation. Aggregated Pt metal

particles were supported on the CNF(HNO$_3$) support at a Pt loading of 30wt%. Pt metal

particles with small size could be uniformly supported on the CNF(HNO$_3$) surface at a

lower Pt loading (Pd = 15wt%) by the impregnation method. However, large Pt metal

particles were deposited at the supports when the Pt loading increased to 30 wt%. Thus,

Pt catalysts with a higher loading needed to be prepared by other methods. Pt catalysts

with a higher loading was prepared as follows: CNF(HNO$_3$) was dispersed into diphenyl

ether containing Pt(acac)$_2$. The solution was refluxed at 443 K for 10 h in N$_2$ and then

filtered. The samples thus obtained were reduced with hydrogen at 773 K. The amount of

Pt(acac)$_2$ dissolved in diphenyl ether was such that the nominal Pt loading in the catalysts

was 40 wt%. Pt metal particles were also deposited on CNF(HCl) and CB according to a

similar method, for comparison. The Pt loading in these catalysts was evaluated by

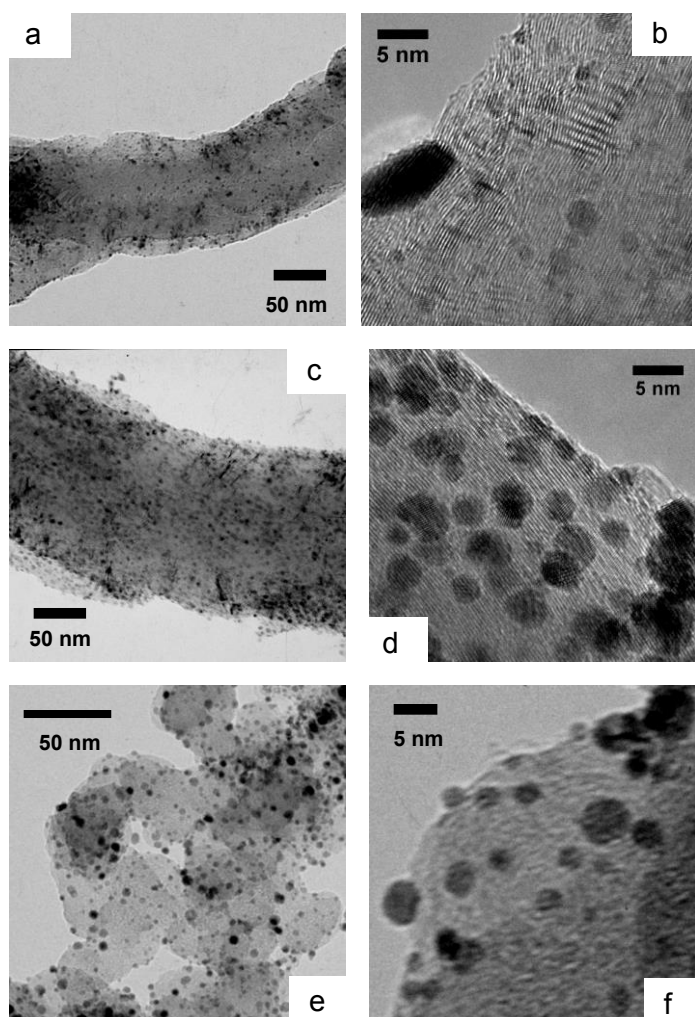thermogravimetric analysis in air to be 5.4 wt% for Pt/CNF(HCl), 30 wt% for

Fig. 2.9 TEM images of Pt/CNF(HCl) (a and b), Pt/CNF(HNO$_3$) (c and d) and Pt/CB (e and f) prepared from Pt (acac)$_2$. These catalysts were reduced with H$_2$ at 773 K.

Pt/CNF(HNO$_3$) and 25 wt% for Pt/CB, suggesting that the pore structures and functional groups on the surface of the CNF(HNO$_3$) support would stabilize the Pt metal precursors or Pt metal particles

Figure 2.9 shows the TEM images of Pt/CNF(HCl), Pt/CNF(HNO$_3$) and Pt/CB catalysts prepared from Pt(acac)$_2$. The Pt metal particles were densely deposited on the surface of the CNF(HNO$_3$) and CB supports, whereas few Pt metal particles were found
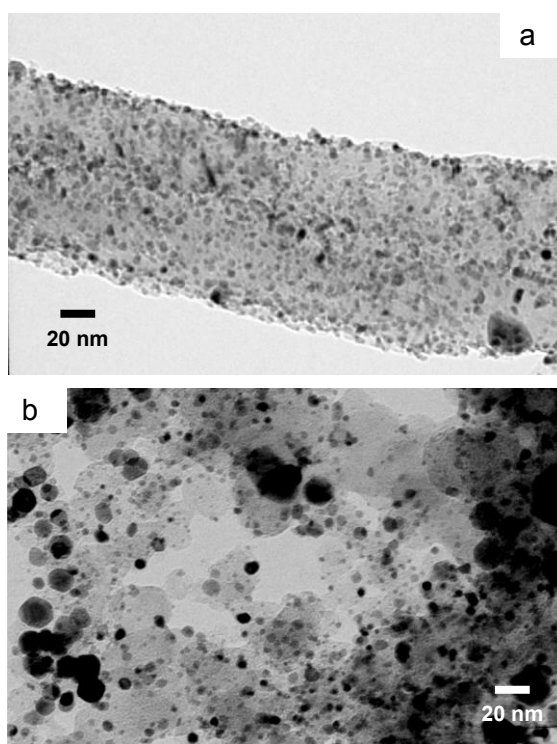
Fig. 2.10 TEM image of Pt/CNF(HNO$_3$) (a) and Pt/CB (b) treated at 973 K.

on the surface of the Pt/CNF(HCl) catalyst. The Pt metal particle size in all of the catalysts ranged from 1 to 3 nm, and the size distribution was very narrow. These results indicate that Pt metal particles of a few nanometers in diameter, can be densely supported on the surfaces of the CNF(HNO$_3$) and CB supports by this preparation method. The Pt metal particles on the surface of the CNF(HNO$_3$) support showed high tolerance to sintering. Figure 2.10 shows the TEM images of the Pt/CNF(HNO$_3$) and Pt/CB catalysts treated at 973 K. In the TEM image of Pt/CB treated at 973 K, the Pt metal particles larger than 10 nm in diameter could be easily found. In contrast, aggregated Pt metal particles were scarcely seen and the size of most of the Pt metal particles was smaller than 5 nm for the Pt/CNF(HNO$_3$) catalysts treated at 973 K. As described earlier, pore structures are present in the surfaces and bodies of CNF(HNO$_3$). It is expected that the Pt metal particles should

be stabilized in the pores in the CNF(HNO₃) support. In addition, the degree of
graphitization of the CNF(HNO₃) support was higher than that of CB, as clarified from
the corresponding XRD patterns for the Pt catalysts. CB is easily hydrogenated to form
methane during treatment of Pt/CB at 973 K in hydrogen, which promotes the sintering
of the Pt metal particles. Therefore, the Pt metal particles in the Pt/CNF(HNO₃) catalysts
showed high durability toward sintering even at high temperatures in a hydrogen
atmosphere.

2.3.3 Preparation of Pt-Co alloy catalysts

The catalytic activity of precious metals can be modified by alloying with other metal
species [47,48]. The catalytic activity of Pt metal supported on carbon materials for ORR
is improved by alloying the Pt metal with transition metals such as Fe, Co and Ni, which
leads to the reduction of Pt loading in the PEFC cathode [32-34]. The Pt-based alloy
catalysts are generally prepared by the deposition of metal precursors on carbon supports,
followed by treatment at higher temperatures > 900 K to allow for the alloy formation
[49,50]. Pt-based alloy catalysts with a high alloying degree can be obtained by this
preparation method, but the predominance of the weak interaction between the metal
particles and carbon supports leads to a serious sintering of the alloy particles and a
consequent decrease in their catalytic activity. The sintering of the Pt-based alloy particles
during the treatment at high temperatures would be suppressed by using CNF(HNO₃) as
a support. Thus, the Pt-Co alloy particles were supported on CNF(HCl), CNF(HNO₃) and
CB supports. The Pt/CNF(HNO₃), Pt/CNF(HCl) and Pt/CB catalysts (Pt loading = 15
wt%) were impregnated into THF containing $Co(NO_3)_2$ (molar ratio Co/Pt = 1.0) and
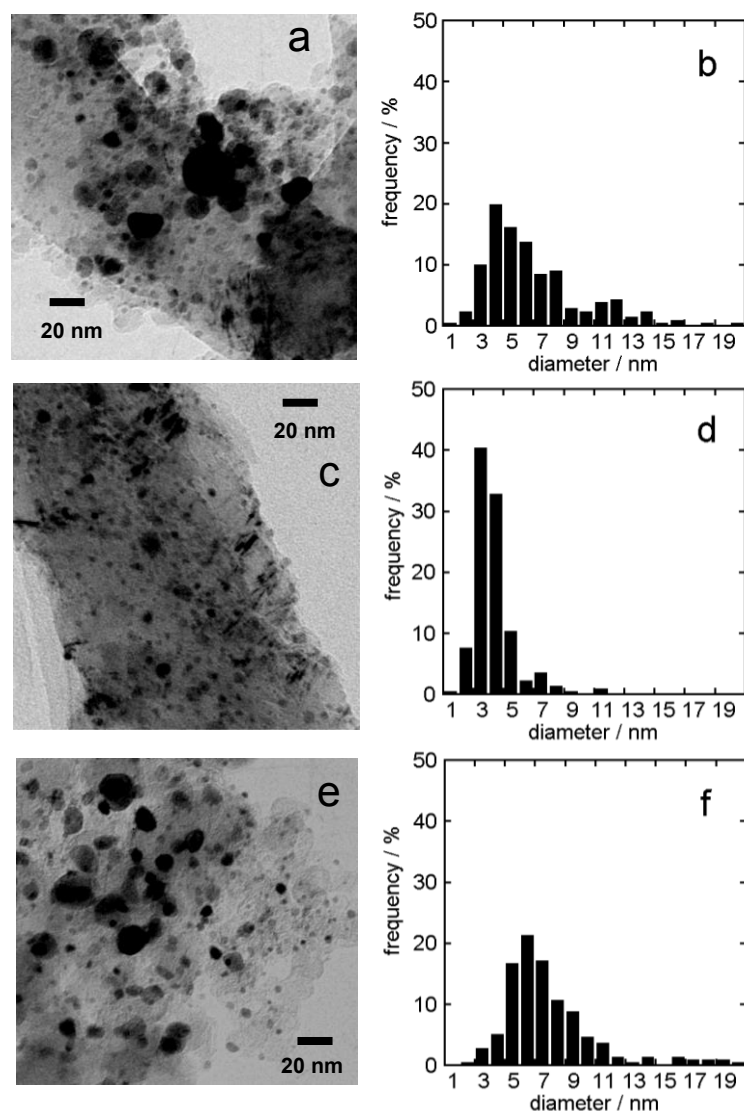dried. The dried samples were then reduced with hydrogen at 573 K and subsequently

Fig. 2.11 TEM images and the distributions of metal particle size for Pt-Co/CNF(HCl) (a and b), Pt-Co/CNF(HNO$_3$) (c and d) and Pt-Co/CB (e and f) treated at 1073 K.

treated at 1073 K in Ar. TEM images of these Pt-Co catalysts are shown in Fig. 2.11. The distributions of metal particle size evaluated by these TEM images are also shown in Fig. 2.11. Many metal particles of a smaller diameter than 5 nm were present in the TEM images of Pt-Co/CB and Pt-Co/CNF(HCl). However, aggregated metal particles larger than 10 nm in diameter were also easily found in the TEM images for Pt-Co/CNF(HCl)
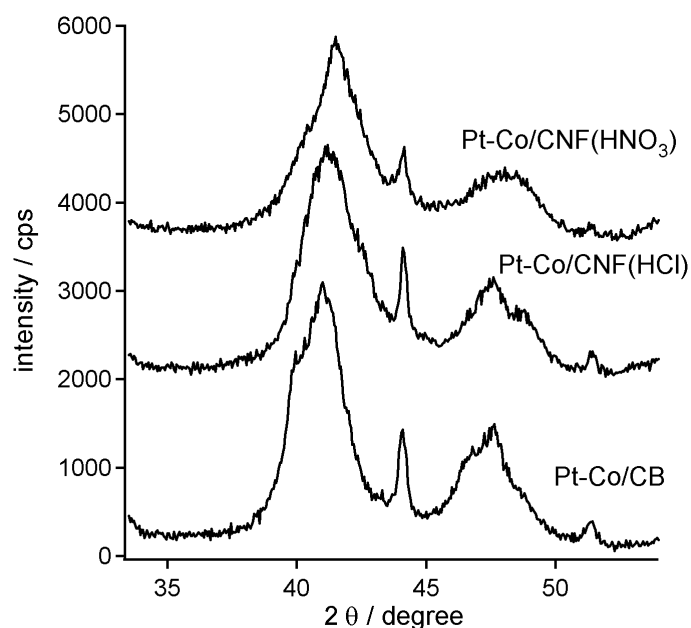
Fig. 2.12 XRD patterns of Pt-Co/CNF(HCl), Pt-Co/CNF(HNO$_3$) and Pt-Co/CB.

and Pt-Co/CB, and the diameter of the observed metal particles were widely distributed from 1 to 20 nm. In contrast, aggregated metal particles were hardly found in the TEM images for Pt-Co/CNF(HNO$_3$), and the size of most of the metal particles observed was smaller than 5 nm. The CNF(HNO$_3$) supports inhibited the sintering of the metal particles during the treatment at 1073 K in Ar.

The XRD patterns of these Pt-Co catalysts were measured in order to clarify the structure and alloying degree of the metals. The results are shown in Fig. 2.12. As shown in the XRD pattern for the supported Pt catalysts (Fig. 2.6), two diffraction lines were characteristic of a fcc Pt metal crystallite, corresponding to the (111) and (200) planes at 2θ values of 40 and 46 °, respectively. In the XRD patterns for all of the Pt-Co catalysts, two diffraction lines characteristic of a fcc Pt crystallite were observed, but the peak position for the Pt-Co catalysts was located at higher 2θ values compared to that of pure
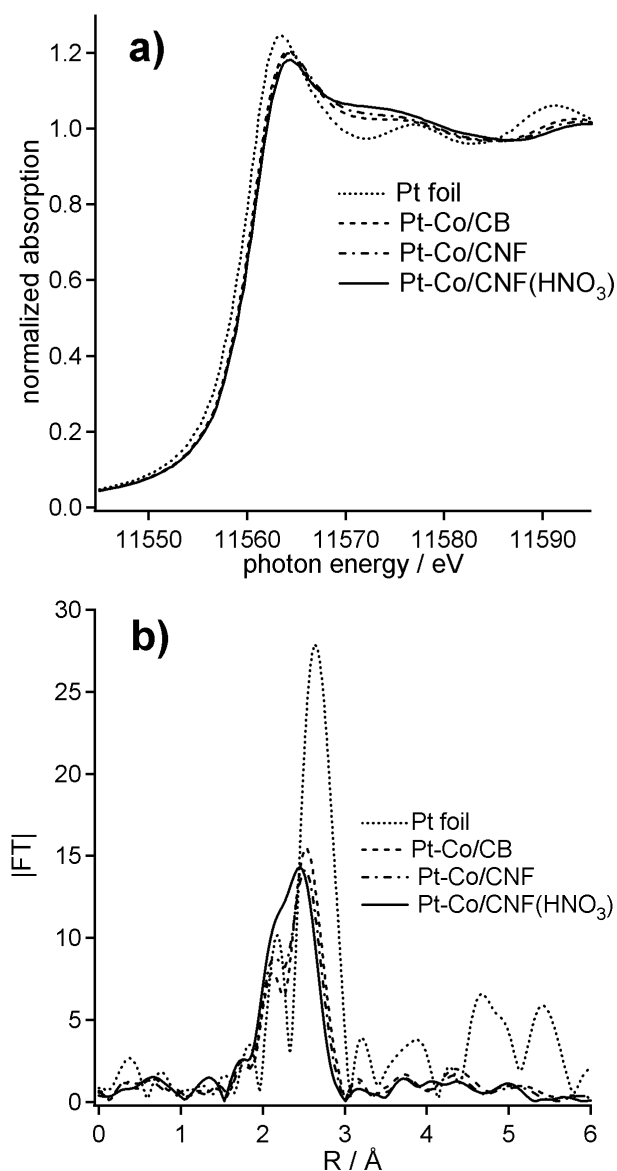
Fig. 2.13 Pt LIII-edge XANES spectra (a) and Fourier transforms of Pt LIII-edge k^3-weighted EXAFS (b) for Pt-Co/CB, Pt-Co/CNF(HCl), Pt-Co/CNF(HNO$_3$) and Pt foil.

Pt metal, indicating the formation of Pt-Co alloys. An additional two peaks were observed at around 44 and 51 ° in the XRD pattern of each of the Pt-Co catalysts. It is considered that these peaks could be due to crystalline Co or Pt-Co alloys with high Co/Pt mole ratios [51]. No reflection arising from a superlattice such as a face-centered tetragonal alloy

57

phase was present in the XRD patterns for the Pt-Co catalysts [52,53]. These results indicate the formation of disordered Pt-Co alloys involving the incorporation of Co atoms into the fcc crystallite of Pt metal. The peak for the (111) plane was shifted toward higher angles in the order of Pt-Co/CB (2θ= 41.0 º) < Pt-Co/CNF(HCl) (41.2 º) < Pt-Co/CNF(HNO$_3$) (41.6 º). Pt-Co/CNF(HNO$_3$) thus had the highest alloying degree among all of the catalysts studied. The peaks due to the Pt-Co alloys in Pt-Co/CNF(HNO$_3$) are broader than those for Pt-Co/CNF(HCl) and Pt-Co/CB, implying a smaller crystallite size of Pt-Co alloys in Pt-Co/CNF(HNO$_3$).

Figure 2.13 shows the Pt L$_{III}$-edge XANES spectra and Fourier transforms of k^3-weighted Pt L$_{III}$-edge EXAFS spectra for the Pt-Co catalysts and Pt foil. XANES spectra of all the Pt-Co catalysts were very similar in shape to that of Pt foil. Therefore, most of the Pt species in all the Pt-Co catalysts studied were present in the metallic state. The strong absorption at around 11560 eV in the Pt L$_{III}$-edge XANES spectra, which is known as a white line, corresponds to an electron transition from 2p$_{3/2}$ to 5d, and the magnitude of the white line is related to the 5 d-electron vacancies [54-56]. The intensity of the white line for all of the Pt-Co catalysts studied was lower than that for Pt foil. Especially, Pt-Co/CNF(HNO$_3$) showed a lower white line intensity compared to the other Pt-Co catalysts. The decrease in the white line intensity for Pt-Co compared to Pt can be easily understood as being due to the electron transfer from Co to Pt, leading to a high electron density around the Pt atoms [57]. The lowest intensity for Pt-Co/CNF(HNO$_3$) implied the highest alloying degree of Pt-Co alloys.

Fourier transforms of the Pt L$_{III}$-edge EXAFS spectra (RSFs, radial structure functions) for the Pt-Co catalysts provided useful information for understanding the structure of the metal particles more clearly. A strong peak was observed at around 2.5 Å

in the RSF for Pt foil. This peak is assignable to the contribution of the first Pt-Pt shell coordination to the EXAFS spectrum. A strong peak is also found in the R range from 1.8 to 3.0 Å in the RSFs for all of the Pt-Co catalysts studied. The peak for the Pt-Co catalysts is located at a shorter distance, compared to that for Pt foil, suggesting alloy formation between Pt and Co. The RSFs for the Pt-Co catalysts were inversely Fourier-transformed in the R range from 1.5 to 3.0 Å, and the EXAFS spectra thus obtained were fitted in the k range from 4.5 to 15.5 Å^{-1}. The structural parameters estimated by the curve-fitting analyses are listed in Table 2.1.

Table. 2-1 Structural parameters estimated by the curve-fitting analyses for Pt L$_{III}$-edge EXAFS spectra for Pt-Co catalysts.

Catalysts	Shell	CN[a]	R[b] (Å)	DW[c] / (Å)
Pt-Co/CNF(HCl)	Pt-Pt	5.8 ± 0.6	2.68	0.073
	Pt-Co	3.9 ± 0.5	2.61	0.085
Pt-Co/CNF(HNO$_3$)	Pt-Pt	4.8 ± 0.5	2.66	0.072
	Pt-Co	4.2 ± 0.6	2.59	0.074
Pt-Co/CB	Pt-Pt	7.2 ± 0.7	2.69	0.075
	Pt-Co	4.0 ± 0.5	2.63	0.090

[a] Coordination number. [b] Interatomic distance. [c] Debye-Waller factor.

The EXAFS spectra for all of the Pt-Co catalysts could be fitted using two kinds of shells, Pt-Pt and Pt-Co bonds. The interatomic distance of Pt-Pt for all the Pt-Co catalysts is ranged from 2.66 to 2.69 Å and the distance is shorter than the Pt-Pt distance in Pt foil (2.76 Å). These results suggest the formation of an alloy between Pt and Co, although the

degree of alloying of Pt-Co depends on the type of carbon support used. The mole ratio of Co to Pt is 1:1 for all of the Pt-Co catalysts studied. Therefore, the coordination number of Pt-Co should be similar to that of Pt-Pt if all of the Co atoms are uniformly incorporated into the fcc Pt crystallite. However, the coordination number of the Pt-Co bond was lower than that of the Pt-Pt bond in the case of the Pt-Co/CNF(HCl) and Pt-Co/CB catalysts. In contrast, the coordination number of Pt-Co was quite similar to that of Pt-Pt for the Pt-Co/CNF(HNO$_3$) catalyst. Additionally, the total coordination number of Pt-Pt and Pt-Co bonds for the Pt-Co/CNF(HNO$_3$) catalyst was lower than that for the other Pt-Co catalysts. The total coordination number of neighboring metal atoms around the Pt atoms corresponds to the crystallite size of the metal; the metal crystallite size becomes larger with the coordination number [58-60]. The Pt-Co/CNF(HNO$_3$) catalysts thus have Pt-Co alloy particles with a smaller crystallite size and a higher alloying degree. The CNF(HNO$_3$) supports prevent the sintering of Pt and Co metal particles at high temperatures, while these metal particles are seriously aggregated on the CNF(HCl) and CB supports. The contact between Pt and Co metal particles with smaller diameters on the CNF(HNO$_3$) support leads to the facile formation of Pt-Co alloy particles with higher alloying degree.

As described earlier, the treatment of CNF(HCl) with HNO$_3$ resulted in the formation of porous structures as well as the introduction of oxygen-containing functional groups in the CNF(HCl). The porous structures and functional groups in the CNF(HNO$_3$) inhibited the sintering of metal particles on their surfaces. In contrast, noncovalent functionalization methods of CNFs also stabilized the Pt metal or Pt-based alloy particles on their surfaces [61,62]. In the functionalization of CNFs with 1-aminopyrene, the pyrenyl groups of 1-aminopyrene are attached onto the basal plane of graphite via π

stacking and amino groups in 1-aminopyrene work as anchoring sites for Pt or Pt-based alloy particles. Zhang et al. reported that Pt metal and Pt-Ru alloy particles of a few nanometers in diameter could be deposited on the CNFs functionalized with 1-aminopyrene through the reduction of metal precursors with ethylene glycol. In the present study, we demonstrated that CNF(HNO$_3$) stabilized Pt and Pt-Co alloy particles of a few nanometers in diameter. In addition, these metal particles on the CNF(HNO$_3$) showed high tolerance to sintering at high temperatures. The porous structures in CNF(HNO$_3$) prevented the sintering of metal particles.

2.3.4 Electrocatalytic performance of Pt-Co/CNF(HNO$_3$)

Figure 2.14 shows the polarization curves obtained with RDE for ORR on the Pt-Co/CNF(HCl), Pt-Co/CNF(HNO$_3$) and Pt-Co/CB catalysts. The ORR for all of the catalysts is diffusion-controlled in a potential range that is lower than 0.8 V, and under a mixed diffusion-kinetic control in the potential range from 0.8 V to 1.0 V. The onset potential for ORR on the Pt-Co/CNF(HCl) catalyst was consistent with that on the Pt-Co/CB catalyst. In contrast, the onset potential for ORR on the Pt-Co/CNF(HNO$_3$) catalyst was located at the higher potential compared to that on the Pt-Co/CNF(HCl) and Pt-Co/CB catalysts. The mass activity at 0.9 V is higher in the order of Pt-Co/CNF(HNO$_3$) (200 mA mg-Pt^{-1}) > Pt-Co/CNF (102 mA mg-Pt^{-1}) > Pt-Co/CB (90 mA mg-Pt^{-1}). The higher mass activity for the Pt-Co/CNF(HNO$_3$) catalyst should result from a smaller crystallite size and a higher degree of alloying of the Pt-Co alloys. Thus, we conclude that CNF(HNO$_3$) is an attractive support for the preparation of highly active Pt-based alloy catalysts.
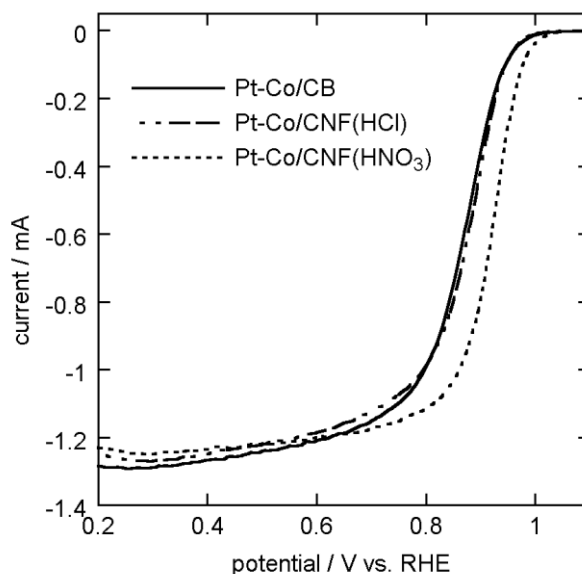
Fig. 2.14 Polarization curves obtained with RDE for the oxygen reduction reaction
(ORR) on Pt-Co/CB, Pt-Co/CNF(HCl) and Pt-Co/CNF(HNO$_3$).

2.4 Conclusions

The treatment of CNF(HCl) with concentrated HNO$_3$ led to the etching of the surface and the body of CNF(HCl), and the consequent formation of pore structures and oxygen-containing functional groups. When the CNF(HNO$_3$) was used as supports, Pt metal particles on the support showed a high tolerance to the sintering at high temperatures, because the metal particles were stabilized in the pores of the supports. In addition, CNF(HNO$_3$) supports were effective for the preparation of Pt-based alloys with a smaller size and a higher alloying degree, since the supports prevented the sintering of metal particles during the treatment at high temperatures to allow for the alloy formation.

References

[1] P. Li, Y.L. Huang, D. Chen, J. Zhu, T.J. Zhao, X.G. Zhou, Catal. Commun. 10 (2009) 815–818.

[2] A.J. Plomp, T. Schubert, U. Storr, K.J. de Jong, J.H. Bitter, Top. Catal. 52 (2009) 424–430.

[3] Z.R. Ismagilov, M.A. Kerzhentsev, N.V. Shikina, A.S. Lisitsyn, L.B. Okhlopkova, Ch.N. Barnakov, M. Sakashita, T. Iijima, K. Tadokoro, Catal. Today 102–103 (2005) 58–66.

[4] M.J. Ledoux, R. Vieira, C. Pham-Huu, N. Keller, J. Catal. 216 (2003) 333–342.

[5] P. Serp, M. Corrias, P. Kalck, Appl. Catal. A: Gen. 253 (2003) 337–358.

[6] M. Pumera, Chem. Eur. J. 15 (2009) 4970–4978.

[7] K. Lee, J. Zhang, H. Wang, D.P. Wilkinson, J. Appl. Electrochem. 36 (2006) 507–522.

[8] J.F. Lin, V. Kamavaram, A.M. Kannan, J. Power Sources 195 (2010) 466–470.

[9] W. Li, C. Liang, W. Zhou, J. Qiu, Z. Zhou, G. Sun, Q. Xin, J. Phys. Chem. B 107 (2003) 6292–6299.

[10] W. Li, X. Wang, Z. Chen, M. Waje, Y. Yan, Langmuir 21 (2005) 9386–9389.

[11] Z.D. Wei, C. Yan, Y. Tan, L. Li, C.X. Sun, Z.G. Shao, P.K. Shen, H.W. Dong, J. Phys. Chem. C 112 (2008) 2617–2677.

[12] P. Ramesh, M.E. Itkis, J.M. Tang, R.C. Haddon, J. Phys. Chem. C 112 (2008) 9089–9094.

[13] J.M. Planeix, N. Coustel, B. Coq, V. Brotons, P.S. Kumbhar, R. Dutartre, P. Geneste, P. Bernier, P.M. Ajayan, J. Am. Chem. Soc. 116 (1994) 7935–7936.

[14] V. Lordi, N. Yao, J. Wei, Chem. Mater. 13 (2001) 733–737.

[15] J.P. Tessonnier, L. Pesant, G. Ehret, M.J. Ledoux, C. Pham-Huu, Appl. Catal. A: Gen. 288 (2005) 203–210.

[16] H. Vu, F. Gonçalves, R. Philippe, E. Lamouroux, M. Corrias, Y. Kihn, D. Plee, P. Kalck, P. Serp, J. Catal. 240 (2006) 18–22.

[17] R.T.K. Baker, Carbon 27 (1989) 315–323.

[18] H. Dai, Acc. Chem. Res. 35 (2002) 1035–1044.

[19] C. Laurent, E. Flahaut, A. Peigney, A. Rousset, New J. Chem. (1998) 1229–1237.

[20] K. Hernadi, A. Fonseca, J.B. Nagy, A. Siska, I. Kirisci, Appl. Catal. A: Gen. 199 (2000) 245–255.

[21] C.H. Lee, J. Park, J.A. Yu, Chem. Phys. Lett. 360 (2002) 250–255.

[22] K. Otsuka, Y. Abe, N. Kanai, Y. Kobayashi, S. Takenaka, E. Tanabe, Carbon 42 (2004) 727–736.

[23] S. Takenaka, S. Kobayashi, H. Ogihara, K. Otsuka, J. Catal. 217 (2003) 79–87.

[24] S. Takenaka, Y. Shigeta, E. Tanabe, K. Otsuka, J. Catal. 220 (2003) 468–477.

[25] C. Park, R.T.K. Baker, J. Phys. Chem. B 103 (1999) 2453–2459.

[26] A.J. Plomp, D.S. Su, K.P. de Jong, J.H. Bitter, J. Phys. Chem. C 113 (2009) 9865–9869.

[27] H.S. Oh, K. Kim, Y.J. Ko, H. Kim, Int. J. Hydrogen Energy 35 (2010) 701–708.

[28] A.S. Lisitsyn, L.B. Okhlopkova, A.E. Shalagina, Z.R. Ismagilov, Carbon 46 (2008) 549–552.

[29] A. Guha, W. Lu, T.A. Zawodzinski Jr., D.A. Schiraldi, Carbon 45 (2007) 1506–1517.

[30] L. Calvillo, M. Gangeri, S. Perathoner, G. Centi, R. Moliner, M.J. Lázaro, J. Power Sources 192 (2008) 144–150.

[31] F. Zaragoza-Martín, D. Sopeña-Escario, E. Morallón, C. Salinas-Martínez de Lecea, J. Power Sources 171 (2007) 302–309.

[32] X. Yu, S. Ye, J. Power Sources 172 (2007) 133–144.

[33] E. Antolini, J.R.C. Salogado, E.R. Gonzalez, J. Power Sources 160 (2006) 957–968.

[34] V. Jalan, E.J. Tayler, J. Electrochem. Soc. 130 (1983) 2299–2302.

[35] S. Chen, W.C. Sheng, N. Yabuuchi, P.J. Ferreira, L.F. Allard, Y. Shao-Horn, J. Phys. Chem. C 113 (2009) 1109–1125.

[36] C. Wang, G.F. Wang, D. van der Vliet, K.C. Chang, N.M. Markovic, V.R. Stamenkovic, Phys. Chem. Chem. Phys. 12 (2010) 6933–6939.

[37] H. Schulenburg, E. Muller, G. Khelashvili, T. Roser, H. Bonnemann, A. Wokaun, G.G. Scherer, J. Phys. Chem. C 113 (2009) 4069–4077.

[38] S. Takenaka, H. Ogihara, K. Otsuka, J. Catal. 208 (2002) 54–63.

[39] A. Ankudinov, B. Ravel, J.J. Rehr, S.D. Conradson, Phys. Rev. B 58 (1998) 7565–7576.

[40] K. Sinha, J. Menendez, Phys. Rev. B 41 (1990) 10845–10847.

[41] R.J. Nemanich, S.A. Solin, Phys. Rev. B 20 (1979) 392–401.

[42] H. Darmstadt, L. Sümmchen, J.-M. Ting, U. Roland, S. Kaliaguine, C. Roy, Carbon 35 (1997) 1581–1585.

[43] R.O. Dilon, J.A. Woollam, V. Katkanant, Phys. Rev. B 29 (1984) 3482–3489.

[44] A. Cuesta, P. Dhamelincourt, J. Laureyns, A. Martínez-Alonso, J.M.D. Tascón, Carbon 32 (1994) 1523–1532.

[45] T. Jawhari, A. Roid, J. Casado, Carbon 33 (1995) 1561–1565.

[46] D.A. Fonseca, H.R. Gutierrez, A.D. Lueking, Micropor. Mesopor. Mater. 113 (2008) 178–186.

[47] S. Takenaka, Y. Shigeta, E. Tanabe, K. Otsuka, J. Phys. Chem. B 108 (2004) 7656–7664.

[48] T. Yamanaka, T. Takeguchi, G. Wang, E.N. Muhamad, W. Ueda, J. Power Sources 195 (2010) 6398–6404.

[49] M. Min, J. Cho, K. Cho, H. Kim, Electrochim. Acta 45 (2000) 4211–4217.

[50] G. Tamizhmani, G.A. Capuano, J. Electrochem. Soc. 141 (1994) 968–975.

[51] F.H.B. Lima, J.F.R. de Castro, L.G.R.A. Santos, E.A. Ticianelli, J. Power Sources 190 (2009) 293–300.

[52] S. Koh, J. Leisch, M.F. Toney, P. Strasser, J. Phys. Chem. C 111 (2007) 3744–3752.

[53] H. Schulenburg, E. Müller, G. Khelashvili, T. Roser, H. Bönnemann, A. Wokaun, G.G. Scherer, J. Phys. Chem. C 113 (2009) 4069–4077.

[54] J.A. Horsley, J. Chem. Phys. 76 (1982) 1451–1458.

[55] Y.W. Tsai, Y.L. Tseng, L.S. Sarma, D.G. Liu, J.F. Lee, B.J. Hwang, J. Phys. Chem. B 108 (2004) 8148–8152.

[56] T. Shishido, H. Asakura, F. Amano, T. Sone, S. Yamazoe, K. Kato, K. Teramura, T. Tanaka, Catal. Lett. 131 (2009) 413–418.

[57] B.J. Hwang, S.M.S. Kumar, C.H. Chen, Monalisa, M.Y. Chen, D.G. Liu, J.F. Lee, J. Phys. Chem. C 111 (2007) 15267–15276.

[58] R.B. Greegor, F.W. Lytle, J. Catal. 63 (1980) 476–486.

[59] S.D. Jackson, J. Willis, G.D. McLellan, G. Webb, M.B. Keegan, R.B. Moyes, S. Simpson, P.B. Wells, R. Whyman, J. Catal. 139 (1993) 191–206.

[60] K. Teramura, S. Okuoka, S. Yamazoe, K. Kato, T. Shishido, T. Tanaka, J. Phys. Chem. C 112 (2008) 8495–8498.

[61] Z. Lin, L. Ji, W.E. Krause, X. Zhang, J. Power Sources 195 (2010) 5520-5526.

[62] Z. Lin, L. Ji, M.D. Woodroof, Y. Yao, W. Krause, X. Zhang, J. Phys. Chem. C 114 (2010) 3791-3797.

Chapter 3

Carbon-supported V-Mo oxides catalysts for oxygen reduction reaction

3.1 Introduction

Polymer electrolyte fuel cells (PEFCs) have been developed as one of the fuel cell technologies. PEFCs with high efficiency, low emission, and low environmental impact can start up fast and easily, and operate at mild temperatures in the range of 20 ~ 100 ℃. The PEFCs also can be applied to automobile, portable power devices, and cogeneration applications [1]. Basically, chemical energy included in fuels such as hydrogen, methanol, and ethanol is directly converted into electric energy in PEFCs. Hydrogen fuel is oxidized at anode and oxygen is reduced into water at cathode of PEFCs, resulting in generating electricity with water and heat. In the PEFC system, catalysts are required at both anode and cathode to promote the corresponding chemical reactions. Pt-based catalysts have been utilized in the state-of the art PEFCs. Wide spread of PEFC is impeded by high cost of Pt [2]. Especially, a large amount of Pt metals is used at the cathode due to the sluggish reaction kinetics for the oxygen reduction reaction (ORR). Thus, the researches on the development of non-precious metal catalysts (NPMCs) for the cathode as an alternative to Pt catalysts have proceeded widely.

As for the development of NPMCs, it is difficult to meet their high performance and durability due to severe cathode conditions such as highly positive potential, low pH, oxygen atmosphere and high temperatures. These severe conditions lead to serious

degradation phenomena including the dissolution of metal, the migration and agglomeration of metal particles, and the deposition of metal in the electrolyte membrane [3]. Therefore, the NPMCs such as transition metal oxides, nitrides, oxynitrides, carbon nitrides, chalcogenides and carbon-based non-precious metal have been investigated in an effort to overcome their degradation problems [3–9].

Transition metal oxide-based catalysts such as group 4 and 5 metal oxides have known for superior candidates of Pt due to their excellent stability in acid electrolyte. However, their metal oxides are insulators and oxygen molecules hardly adsorb on their surfaces when the metal oxides are completely oxidized. Thus transition metal oxide-based catalysts have been modified by addition of foreign metal species to obtain high catalytic activity for the ORR [10–13].

We focused on bimetallic oxide catalysts using heteropolyacids (HPAs) as the main metal precursors for the preparation of the catalysts. The HPAs as an inorganic acid are composed of a particular combination of hydrogen, oxygen, addenda atom (= Mo, V, W and so on), and heteroatom (= Si, P and so on). These HPAs have peculiar properties such as high chemical and thermal stability, multi-electron redox ability [3]. In particular, HPAs with Keggin structures such as $H_3PMo_{12}O_{40}$ and $H_3PW_{12}O_{40}$, shown in Fig. 3.1, are extensively used as active catalysts for various reactions [14–17]. The order of the ability for reduction-oxidation reaction (redox) of following HPAs with the Keggin structure is reported as follows :[3]

$H_3PMo_{12}O_{40} > H_4SiMo_{12}O_{40} \gg H_3PW_{12}O_{40} > H_4SiW_{12}O_{40}$
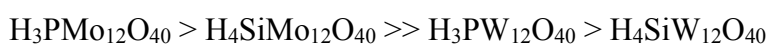
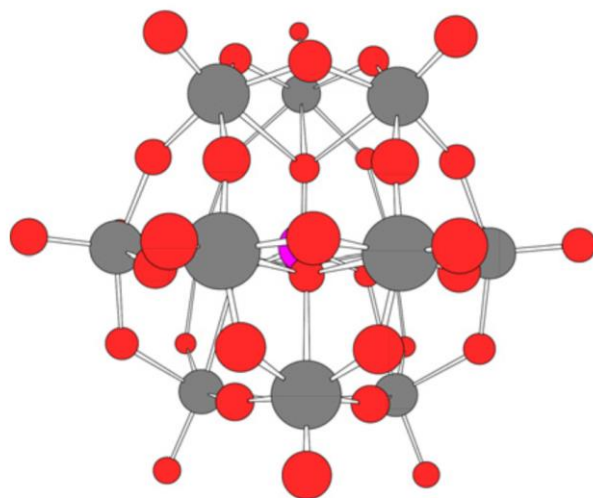The $H_3PMo_{12}O_{40}$ with the highest redox ability shows high catalytic activity for the

69

Fig. 3.1 HPAs with Keggin structures (Pink = P or Si, Gray = Mo or W, Red = O) [14].

oxidation of light alkanes and alcohols with molecular oxygen, which means the high affinity of $H_3PMo_{12}O_{40}$ with molecular oxygen. In addition, the $H_3PMo_{12}O_{40}$ has its redox ability after heat-treatment at high temperature [18].

In this study, the HPAs with the Keggin structure including $H_3PMo_{12}O_{40}$ and $H_4SiMo_{12}O_{40}$ were chosen as the main metal precursors due to their outstanding redox ability. We investigated ORR activity of the Mo-based oxide catalysts prepared from the $H_3PMo_{12}O_{40}$ and $H_4SiMo_{12}O_{40}$. Furthermore, the Mo-based oxide catalysts were modified with transition metal cations (M = Fe, Co, Cr, Ni, V, and Cu) to enhance their ORR activity.

3.2 Experimental

3.2.1 Preparation of catalysts

Carbon black (denoted as CB, Vulcan XC-72, supplied from CABOT) was used as a support. CB-supported Mo oxide catalyst (denoted as MoO_x/CB) and CB-supported Mo

oxide catalysts modified with M cations (M = Fe, Co, Cr, Ni, V, and Cu; denote as M-MoO$_x$/CB) were prepared by a conventional impregnation method. CB powder was impregnated into a mixed aqueous solution containing H$_3$(PMo$_{12}$O$_{40}$)·nH$_2$O and another metal oxide precursors such as Fe(NO$_3$)$_3$, Co(NO$_3$)$_2$, Cr(NO$_3$)$_2$, Ni(NO$_3$)$_2$, NH$_4$VO$_3$, and Cu(NO$_3$)$_2$ at 343 K and then dried at 353 K. Samples thus obtained were treated in N$_2$ gas at 773 K for 3 h. The loading of Mo cation in these catalysts was adjusted to be 2.4 wt% and the molar ratio of Mo cations and another transition metal cations was to be 1/1.

MoO$_x$/CB modified with another metal cations was also prepared using different Mo oxide precursors, H$_3$(PMo$_{12}$O$_{40}$)·nH$_2$O, SiO$_2$•12MoO$_3$•nH$_2$O, and (NH$_4$)$_6$Mo$_7$O$_{24}$•4H$_2$O. Catalysts prepared from H$_3$(PMo$_{12}$O$_{40}$)·nH$_2$O, SiO$_2$•12MoO$_3$•nH$_2$O, and (NH$_4$)$_6$Mo$_7$O$_{24}$•4H$_2$O were denoted as M-MoO$_x$(HPMo)/CB, M-MoO$_x$(HSiMo)/CB, M-MoO$_x$(NH$_4$Mo)/CB, respectively.

3.2.2 Electrochemical measurements

Polarization curves of the ORR and cyclic voltammograms (CVs) for all the Mo-based oxide catalysts were measured by a conventional three-electrode electrochemical cell with Au foil and Ag/AgCl electrode as counter and reference electrodes, respectively. Working electrode (5 mm diameter) was composed of a glassy carbon rod. A catalyst ink was prepared by ultrasonically mixing the catalysts, water, and 2-propanol. The prepared ink was deposited on the surface of glassy carbon rod and then Nafion solution diluted with methanol was dropped on the glassy carbon rod with the catalysts. The working electrode was immersed in 0.1 M HClO$_4$ solution. The CVs for the catalysts were measured by changing the potential of the working electrode in the range of 0.05 to 1.20

71

V vs. RHE at scan rate of 10 mV s^{-1} in N$_2$-purged HClO$_4$ solution. Polarization curves for the ORR were obtained by using a rotating disk electrode (RDE) method. During the RDE measurement, the potential was changed from 0.05 to 1.20 V vs. RHE at scan rate of 5 mV s^{-1} with a rotating rate of the working electrode = 1600 rpm in O$_2$-saturated HClO$_4$. Onset potential of the ORR on the catalysts was defined at the potential of the ORR current density (j$_{ORR}$) = - 0.02 mA cm^{-2}. j$_{ORR}$ was evaluated by subtraction of current density in N$_2$-purged HClO$_4$ from one in O$_2$-saturated HClO$_4$.

3.2.3 Characterization of catalysts

Mo-based oxide catalysts were characterized by transmission electron microscopy (TEM), high-angle annular dark field scanning TEM (HAADF-STEM), and X-ray photoelectron spectroscopy (XPS). The morphology of catalysts was observed by TEM and HAADF-STEM (Jeol JEM-ARM 200F). Specimens for the measurement of TEM images were prepared as follows. The catalyst powder was suspended in 2-propanol and ultrasonically treated. The solution was then dropped on copper grid and dried in vacuum oven. The electronic state of metal cations in Mo-based oxide catalysts was evaluated by XPS (Physical Electronics Corp. PHI 5800 ESCA) using Al Kα radiation operating at 14 kV. The binding energy data of all the Mo-based oxide catalysts in XPS spectra were corrected with a C 1s peak of 284.5 eV.

3.3 Results and discussion

3.3.1 Catalytic activity of Mo-based oxide catalysts for the ORR

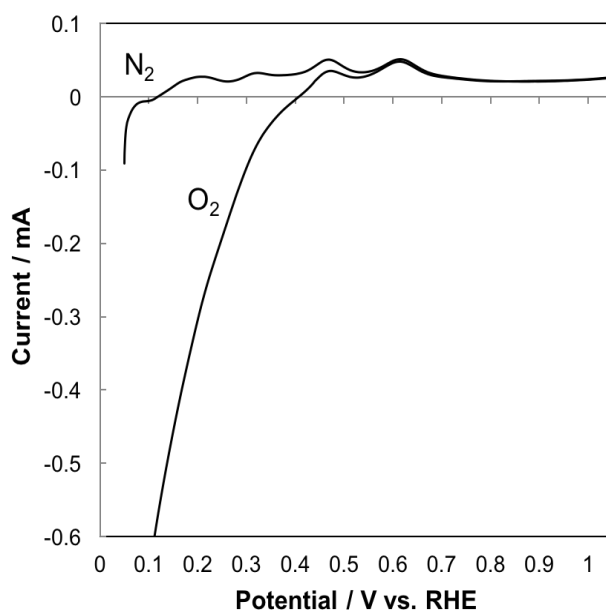Figure 3.2 shows linear sweep voltammograms (LSVs) for MoO$_x$/CB in O$_2$-saturated

Fig. 3.2 Current-potential curves of MoO_x/CB in O_2-saturated and N_2-purged 0.1 M
$HClO_4$.

0.1 M $HClO_4$ and in N_2-purged 0.1 M $HClO_4$. The MoO_x/CB was prepared from
$H_3PMo_{12}O_{40}$. LSV measured in O_2-saturated $HClO_4$ was similar to that in N_2-purged
$HClO_4$ in the potential range from 1.20 to 0.6 V. However, the reduction current became
higher in O_2-saturated $HClO_4$ compared to that in N_2-purged $HClO_4$ in the potential range
lower than 0.6 V. This result indicates that the MoO_x/CB has the catalytic activity for the
ORR. Hereafter, polarization curve for the ORR was shown in the present chapter by
subtracting the LSV in N_2-purged $HClO_4$ from one in O_2-saturated $HClO_4$.

Figure 3.3a shows polarization curves for the ORR of MoO_x/CB catalysts modified
with different metal cations. Onset potential of the ORR strongly depends on the types of
metal cations added into MoO_x/CB. The onset potential for Cu-MoO_x/CB was lower than
that of MoO_x/CB. In contrast, the addition of Co, Fe, Cr, Ni, and V into MoO_x/CB led to
the shift of onset potentials toward higher potentials. Figure 3.3b shows the current

73
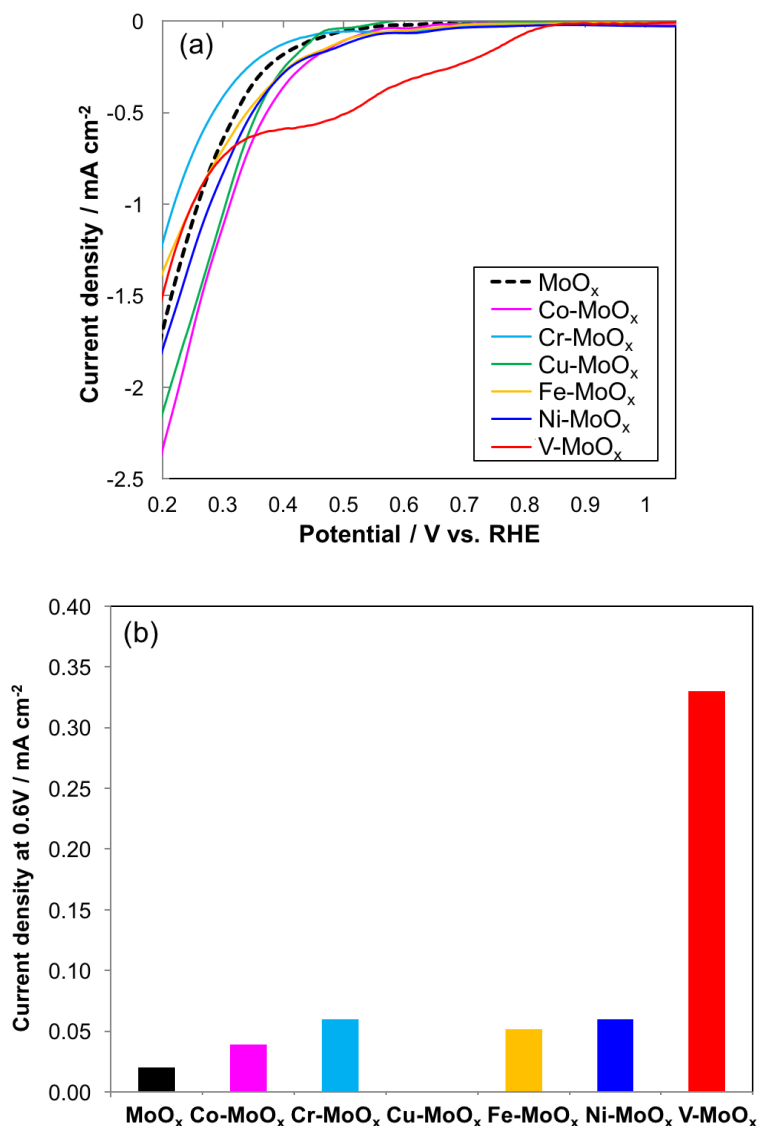
Fig. 3.3 (a) Polarization curves for the ORR and (b) current density at 0.6 V of
Mo-based oxide catalysts in 0.1 M HClO4.

density at 0.6 V for M-MoO$_x$/CB catalysts. The M-MoO$_x$/CB other than Cu-MoO$_x$/CB
showed higher activity for the ORR than the MoO$_x$/CB. Interestingly, V-MoO$_x$/CB
exhibited significantly high ORR current. The V-MoO$_x$/CB had approximately 17 times
higher ORR activity than the MoO$_x$/CB. The ORR activity of the V-MoO$_x$/CB would be
enhanced by modification of catalytically active Mo oxides with V cations. Catalytic
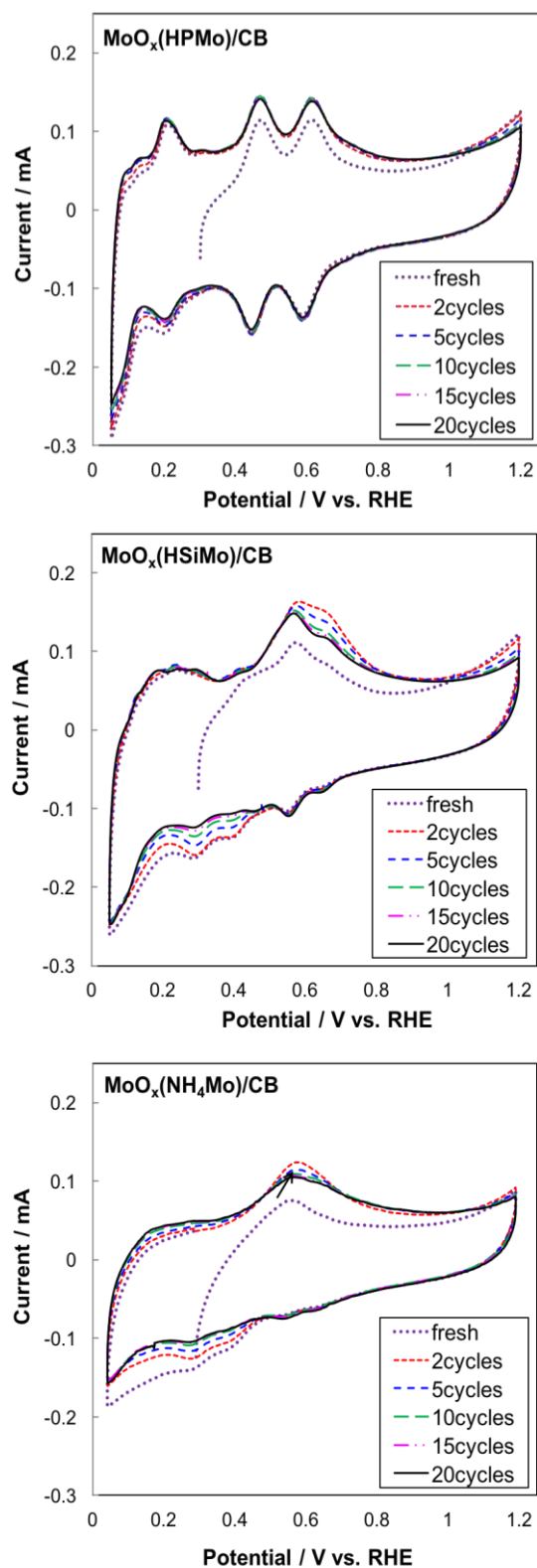
Fig. 3.4 CVs for MoO$_x$/CB prepared from different Mo precursors.

performance of V-MoO$_x$/CB catalysts was thus investigated hereafter in detail to improve

75

their ORR activity.

3.3.2 Electrochemical measurement of V-Mo oxide catalysts

Figure 3.4 shows CVs for MoO_x/CB catalysts prepared by different Mo oxide precursors. The shapes of the CVs were different depending on the types of the used Mo precursors. All the MoO_x/CB catalysts showed different oxidation and reduction peaks, which were attributed to different Mo species in these catalysts. In particular, the MoO_x(HPMo)/CB and MoO_x(HSiMo)/CB had their multiple redox ability although the structure of the HPA was decomposed and rearranged during heat-treatment of its catalyst. During potential cycling, the redox peak currents for MoO_x(HSiMo)/CB and MoO_x(NH_4Mo)/CB gradually decreased. In contrast, there was almost no change in the currents of the MoO_x(HPMo)/CB during the potential cycling. Thus, the MoO_x(HPMo)/CB was stable in acidic electrolyte. These MoO_x/CB with the different Mo precursors were modified with V cations for improvement of the ORR activity.

Figure 3.5 shows a comparison of CVs for MoO_x with and without V. For all the V-MoO_x/CB catalysts, the peak potentials due to the promoted reduction of Mo cations were changed by addition of V cations into the MoO_x/CB. The reduction peaks for the V-MoO_x(HPMo)/CB were positively shifted by addition of V cation.

The ORR properties of MoO_x/CB modified with or without V prepared from various MoO_x precursors in 0.1 M $HClO_4$ solution were investigated, as shown in Fig. 3.6. For the MoO_x/CB prepared from Mo-based HPA precursors, the onset potential increased from around 0.6 to 0.8 V by addition of V cations. Furthermore, the ORR current for the both the MoO_x(HPMo)/CB and MoO_x(HSiMo)/CB increased by addition of V cation.
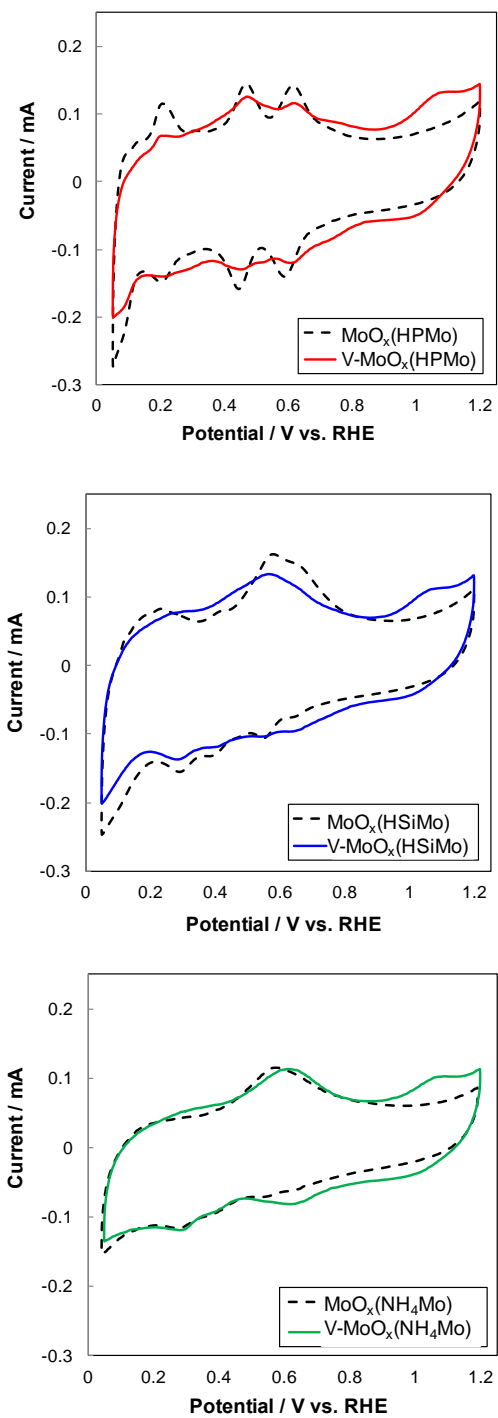
Fig. 3.5 CVs for V-MoO$_x$/CB prepared from different Mo precursors after 3 cycles.

The ORR current of MoO$_x$(HPMo)/CB, MoO$_x$(HSiMo)/CB, V-MoO$_x$(HPMo)/CB, V-
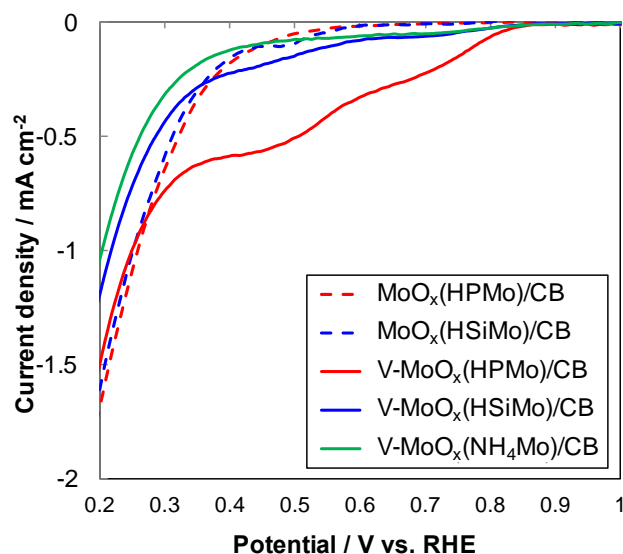
Fig. 3.6 Polarization curves for the ORR of MoO$_x$/CB and V-MoO$_x$/CB prepared from various Mo precursors.

MoO$_x$(HSiMo)/CB, and V-MoO$_x$(NH$_4$Mo)/CB was -0.019, -0.023, -0.330, -0.084, and -0.061 mA cm^{-2} at 0.6 V, respectively. The V-MoO$_x$(HPMo)/CB had the highest ORR current among all the catalysts tested in Fig. 3.6. These results indicate that the ORR current was enhanced by addition of V cation in MoO$_x$ based catalysts. As general ORR system on HPAs, the Mo oxides are reduced firstly to Mo cations with lower oxidation states and then reoxidized to higher oxidation states, and oxygen molecule is reduced by the Mo cations, simultaneously [14,19,20]. This ORR system for the Mo-based catalysts can be applied to the V-MoO$_x$/CB. As mentioned above, the reduction peaks for V-MoO$_x$(HPMo)/CB, shown in Fig. 3.5 were positively shifted by addition of V cation. This result suggests the faster rate of reduction of the Mo cation by addition of V cations. Thus, the ORR current for the V-MoO$_x$(HPMo)/CB was higher than that for MoO$_x$(HPMo)/CB.
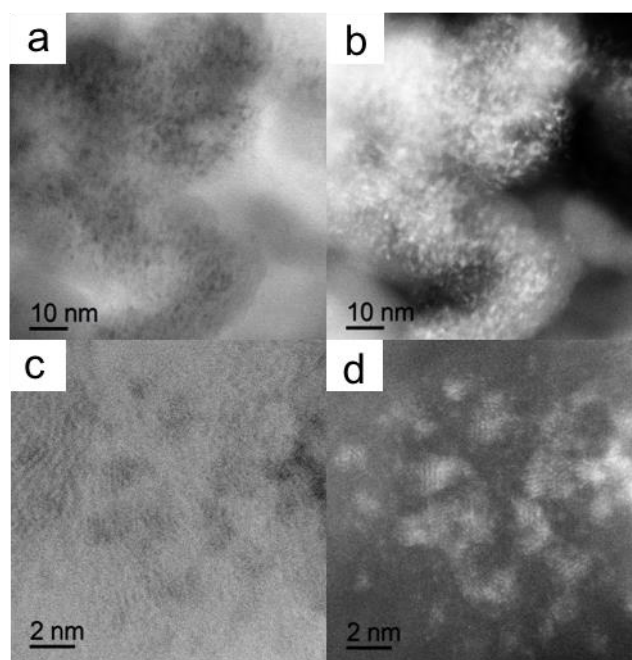
Fig. 3.7 BF-STEM and DF-STEM images of V-MoO$_x$(HPMo)/CB.

3.3.3 Characterization of V-Mo oxide catalysts

Figure 3.7 shows bright field (BF)-STEM (a and c) and dark field(DF)-STEM (b and d) images of V-MoO$_x$(HPMo)/CB. In the BF images (Fig. 3.7a and 3.7c), it was difficult to observe the deposited V and Mo oxide particles because of weak contrast [21]. In contrast, the oxide particles could be identified in the DF-STEM images (Fig. 3.7b and 3.7d) because of a so-called Z-contrast's effect [22]. The Mo and V oxide particles of about 1 ~ 2 nm were uniformly dispersed on carbon support, resulting in contribution to high catalytic activity for the ORR [13].

XRD measurement for the V-MoO$_x$(HPMo)/CB was carried out to analyze the structure of its catalyst. However, there were no peaks for the metal species such as V and Mo in XRD patterns of V-MoO$_x$(HPMo)/CB (not shown). Thus, V-MoO$_x$(HPMo)/CB is composed of too small metal oxides in size or metal oxides with amorphous structure.
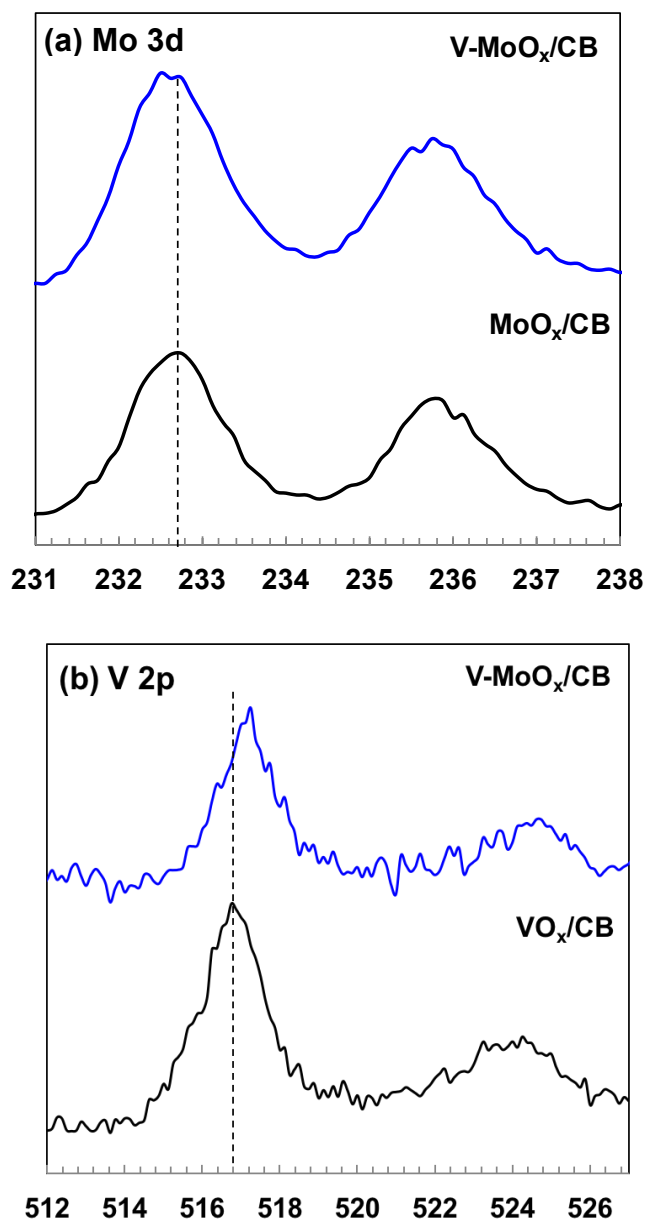
Fig. 3.8 XPS spectra of Mo 3d and V 2p core level for $MoO_x(HPMo)/CB$ and $V-MoO_x(HPMo)/CB$.

Thus, XPS measurement was carried out to confirm the existence of Mo and V oxides and chemical states of their metal cations.

Figure 3.8 shows XPS spectra of Mo 3d and V 2p core level for $MoO_x(HPMo)/CB$ and $V-MoO_x(HPMo)/CB$. Two peaks were observed in the spectra for Mo 3d and V 2p.

The peaks due to Mo species for the V-MoO$_x$(HPMo)/CB were located at around 232.5 eV and 235.8 eV, which were assigned to Mo^{6+} [20,23–25]. As the addition of V cations into the MoO$_x$/CB, the peaks due to Mo cations were slightly shifted to lower binding energy than that of MoO$_x$(HPMo)/CB. On the other hand, the binding energies due to V cations (Mo^{6+}) for the V-MoO$_x$(HPMo)/CB were shifted toward higher energy compared with that of MoO$_x$(HPMo)/CB [26,27]. These results indicate that the Mo^{6+} cations interacted with V^{5+} cations in the V-MoO$_x$(HPMo)/CB. The interaction between Mo and V cations may contribute to the improvement in the catalytic activity for the ORR.

3.4 Conclusions

MoO$_x$/CB catalysts modified with transition metals such as Fe, Co, Cr, Ni, V, and Cu were prepared by a conventional impregnation method. The MoO$_x$/CB modified with V cations exhibited the highest catalytic activity for the ORR among all the modified MoO$_x$/CB catalysts tested in the present chapter. The V-MoO$_x$(HPMo)/CB prepared from H$_3$PMo$_{12}$O$_{40}$ precursor showed the higher catalytic activity for the ORR than the V-MoO$_x$(HSiMo)/CB and V-MoO$_x$(NH$_4$Mo)/CB. The higher activity for the ORR of the V-MoO$_x$(HPMo)/CB could be attributed to the stable MoO$_x$ in acid media and the promoted reduction of the Mo oxides with the addition of V cations.

Moreover, as the addition of V cations into the MoO$_x$(HPMo)/CB, Mo cations interacted with V cations by XPS analysis and the tiny Mo and V oxide particles of about 1 ~ 2 nm were deposited on the carbon support, resulting in contribution to high catalytic activity.

References

[1] R. Othman, A.L. Dicks, Z. Zhu, Int. J. Hydrogen Energy 37 (2012) 357–372.

[2] Y. Wang, D. Leung Y.C., J. Xuan, H. Wang, Renew. Sustain. Energy Rev. 65 (2016) 961–977.

[3] T. Matsui, E. Morikawa, S. Nakada, T. Okanishi, H. Muroyama, Y. Hirao, T. Takahashi, K. Eguchi, ACS Appl. Mater. Interfaces 8 (2016) 18119–18125.

[4] K. Ota, Y. Ohgi, K.-D. Nam, K. Matsuzawa, S. Mitsushima, A. Ishihara, J. Power Sources 196 (2011) 5256–5263.

[5] K. Lee, L. Zhang, J. Zhang, Electrochem. Commun. 9 (2007) 1704–1708.

[6] A. Rabis, P. Rodriguez, T.J. Schmidt, ACS Catal. 2 (2012) 864–890.

[7] Y. Hu, X. Zhao, Y. Huang, Q. Li, N.J. Bjerrum, C. Liu, W. Xing, J. Power Sources 225 (2013) 129–136.

[8] D.C. Higgins, Z. Chen, Can. J. Chem. Eng. 91 (2013) 1881–1895.

[9] Y. Takasu, M. Suzuki, H. Yang, T. Ohashi, W. Sugimoto, Electrochim. Acta 55 (2010) 8220–8229.

[10] A. Ishihara, Y. Ohgi, K. Matsuzawa, S. Mitsushima, K.I. Ota, Electrochim. Acta 55 (2010) 8005–8012.

[11] JH. Kim, A. Ishihara, S. Mitsushima, N. Kamiya, K. Ota, Electrochim. Acta 52 (2007) 2492–2497.

[12] Y. Liu, A. Ishihara, S. Mitsushima, K. ichiro Ota, Electrochim. Acta 55 (2010) 1239–1244.

[13] J. Seo, D. Cha, K. Takanabe, J. Kubota, K. Domen, Phys. Chem. Chem. Phys. 16 (2014) 895–8.

[14] R.J. Stanis, M.C. Kuo, A.J. Rickett, J.A. Turner, A.M. Herring, Electrochim. Acta 53 (2008) 8277–8286.

[15] I. V. Kozhevnikov, Chem. Rev. 98 (1998) 171–198.

[16] R. Wlodarczyk, M. Chojak, K. Miecznikowski, A. Kolary, P.J. Kulesza, R. Marassi, J. Power Sources 159 (2006) 802–809.

[17] B.R. Limoges, R.J. Stanis, J.A. Turner, A.M. Herring, Electrochim. Acta 50 (2005) 1169–1179.

[18] G. Mestl, T. Ilkenhans, D. Spielbauer, M. Dieterle, O. Timpe, J. Krohnert, F. Jentoft, H. Knozinger, R. Schlogl, Appl. Catal. a-General 210 (2001) 13–34.

[19] R. Wlodarczyk, M. Chojak, K. Miecznikowski, A. Kolary, P.J. Kulesza, R. Marassi, J. Power Sources 159 (2006) 802–809.

[20] N.P. Lebedeva, G.J.M. Janssen, Electrochim. Acta 51 (2005) 29–40.

[21] T. Ioroi, T. Akita, S.I. Yamazaki, Z. Siroma, N. Fujiwara, K. Yasuda, Electrochim. Acta 52 (2006) 491–498.

[22] a. J. Armenta-González, R. Carrera-Cerritos, M. Guerra-Balcázar, L.G. Arriaga, J. Ledesma-García, J. Appl. Electrochem. 45 (2014) 33–41.

[23] Z.X. Liu, Y.Q. Li, S.X. Qi, K. Xie, N.J. Wu, Q.X. Bao, Appl. Catal. 56 (1989) 207–218.

[24] J. Qi, L. Jiang, Q. Jiang, S. Wang, G. Sun, J. Phys. Chem. C 114 (2010) 18159–18166.

[25] C.O. a Olsson, H.J. Mathieu, D. Landolt, Surf. Interface Anal. 34 (2002) 130–134.

[26] M. Demeter, M. Neumann, W. Reichelt, Surf. Sci. 454 (2000) 41–44.

[27] E. Hryha, E. Rutqvist, L. Nyborg, Surf. Interface Anal. 44 (2012) 1022–1025.

Chapter 4

Carbon-supported Pd-Ag catalysts with silica-coating layers as active and durable cathode catalysts for polymer electrolyte fuel cells

4.1 Introduction

Polymer electrolyte fuel cells (PEFCs) are promising alternative devices because of their high energy conversion efficiency and low emission of CO, CO_2 and NO_x. The PFECs produce electricity from electrochemical oxidation of hydrogen with oxygen [1]. Pt metal catalysts have been used as the active catalysts for hydrogen oxidation reaction (HOR) at anode and oxygen reduction reaction (ORR) at cathode. A large amount of Pt metals in these catalysts are consumed at the cathode compared with the anode due to the sluggish rate of the ORR. Moreover, the Pt metal is too expensive and limited resource, which results in the inhibition of commercialization of the PEFCs. Thus, many studies on new cathode catalysts for reducing the Pt metal loading or replacing Pt metal have been reported. The Pt-based alloy catalysts, including transition metals such as Co, Cu, Fe, and Pd, showed the higher activity for the ORR than pure Pt metal catalyst. Therefore, the Pt metal loading in PEFC cathode can be reduced when the Pt-based alloy catalysts are used [2–6]. It is eventually required to develop non-Pt catalysts for full commercialization of the PEFCs. However, most metal species in the cathode catalysts are dissolved due to severe cathode conditions such as low pH, high temperature, highly positive potential,

and an oxygen atmosphere, which results in a rapid deactivation of the catalysts at the cathode. It is thus challenging to develop the non-Pt catalysts with high activity and durability [7].

Recently, Pd-based catalysts, one of possible candidates to substitute for Pt, have been investigated as active non-Pt catalysts because Pd metal is less expensive and more abundant than Pt [8]. The Pd-based alloy catalysts modified with transition metals such as Fe, Ni, Co and Cu show higher ORR activity in PEFCs compared with pure Pd catalyst [7,9–11]. For these Pd-based alloy catalysts, the treatment at high temperature is required to form alloy metals during the preparation of catalysts. During the treatment of Pd-based catalysts at high temperature, however, the metal particles seriously agglomerate, which results in the decrease of catalytic activity [11,12]. Thus, it is needed to investigate methods for the preparation of Pd-based catalysts at low temperatures.

In the preparation of catalysts, ethylene glycol (EG) has been widely used as a solvent, reducing agent, and stabilizer. Glycolate, generated from EG oxidation, enhances the formation of metal nanoparticles with well-dispersed and small size due to the excellent interaction between glycolate and metal particle surfaces [13–16]. However, it is difficult to reduce the metal cations with EG at low temperature because poor reduction ability of EG. In contrast, $NaBH_4$ has strong reduction ability at low temperature, although it is difficult to control the particle size and dispersion in catalysts. In an effort to activate EG at low temperature Pt based catalysts were prepared by the reduction with $NaBH_4$ in the presence of EG [14,17–19]. During the preparation of Pt catalysts, $Na^+B^-(OCH_2CH_2OH)_4$ produced from EG and $NaBH_4$ serves as a reducing agent for Pt precursor and a stabilizer for the dispersion of Pt nanoparticles and as a result, the Pt catalysts with small particles and a good dispersion can be obtained at low temperature [17]. Therefore, the modified

85

NaBH$_4$ reduction methods in the presence of EG were applied to obtain the Pd-based catalysts with small particles and a well-defined dispersion, which should lead to high catalytic activity. On the other hand, the Pd-based catalysts have still a problem concerning their durability. Due to the severe conditions of cathode, metal species in the Pd-based catalysts are easily dissolved, which leads to the catalyst deactivation. Thus, it is required to prevent the dissolution of metal species in the Pd-based catalysts under the cathode conditions.

We have developed silica-coated Pt or Pd-based catalysts for the cathode of PEFCs. The silica layers in the silica-coated catalysts prevent the migration of metal particles on the carbon supports and the diffusion of dissolved matal cations out of silica layers in Pt or Pd-based catalysts under the cathode conditions [7,20–22]. Thus, silica-coated Pt or Pd-based catalysts show the excellent durability under the cathode conditions.

In the present study, we developed highly active and durable Pd-based catalysts. The Pd-based catalysts with smaller metal particle sizes were prepared using NaBH$_4$ as a reductant in the presence of EG. Active Pd-based catalysts thus obtained were covered with silica layers to improve their durability under the cathode conditions.

4.2 Experimental

4.2.1 Preparation of catalysts

Carbon black (CB, Vulcan X-72 supplied from Cabot Co.) was used as supports for Pd-based catalysts. CB-supported Pd catalyst (denoted as Pd/CB, hereafter) and CB-supported Pd catalysts modified with M (M = Cu, Co, Y, or Ag; denoted as Pd-M/CB) were prepared by reduction of metal species with NaBH$_4$ in the presence of EG or the

conventional impregnation method. CB powder was dispersed in EG solution containing PdCl$_2$ and another metal precursors such as Cu(NO$_3$)$_2$, Co(NO$_3$)$_2$, YCl$_3$, or AgNO$_3$. The mixed suspension was ultrasonically treated and then stirred with a magnetic bar in N$_2$ gas at room temperature for 0.5 h. NaBH$_4$ dissolved in EG was added to the suspension and stirred at room temperature for 2 h. Samples thus obtained were washed with distilled water for several times and dried in air at 333 K. Pd-M/CB prepared by this method is denoted as Pd-M/CB(N). For comparison, Pd-M/CB catalyst was also prepared by a conventional impregnation method. The CB powder was impregnated into a mixed solution containing Pd(NO$_3$)$_2$ and another metal precursor and dried at 333 K. The dried sample was reduced by H$_2$ diluted with Ar gas at 773 K for 2h. Sample thus obtained is denoted as Pd-M/CB(I).

Pd-based catalysts were covered with silica layers by the hydrolysis and poly-condensation of 3-aminopropyltriethoxysilane (APTES) and tetraethoxysilane (TEOS) as silica sources [10,22,23]. Pd-based catalysts were dispersed in water. pH value of the suspension was adjusted to approximately 10 by addition of triethlyamine. After ultrasonically treated and stirred at 333 K for 0.5 h, APTES was added to the suspension and then stirred at 333 K for 0.5 h. TEOS was then added to the suspension and stirred at 333 K for 2 h. The obtained samples were dried in air at 333 K and reduced in H$_2$ diluted with Ar gas at 623 K for 2 h. The silica-coated Pd-M/CB(N) is denoted as SiO$_2$/Pd-M/CB(N).

4.2.2 Characterization of catalysts

All the Pd-based catalysts were characterized by inductively coupled plasma optical emission spectrometry (ICP-OES), X-ray diffraction (XRD), transmission electron

microscopy (TEM), and high-angle annular dark field scanning TEM (HAADF-STEM).

The loading of Pd, Ag, and SiO$_2$ in all the Pd-based catalysts was evaluated by ICP-OES (Perkin Elmer Optima 8300). The Pd-based catalysts were analyzed by XRD (Rigaku Ultima IV) using Cu Kα radiation (λ = 1.5406 Å). The morphology of the Pd-based catalysts was observed by TEM (JEOL JEM-3000F) and HAADF-STEM (JEOL JEM-ARM 200F). Specimens for measurement of TEM images were prepared as follows. The catalyst powder was suspended in 2-propanol and ultrasonically treated. The suspension was then dropped on copper grid and dried in vacuum oven.

4.2.3 Electrochemical measurements

Cyclic voltammograms (CVs) and polarization curves of the ORR for all the Pd-based catalysts were measured using a conventional three-electrode electrochemical cell with Pt wire and a reversible hydrogen electrode (RHE) as counter and reference electrodes, respectively. A glassy carbon electrode disk (6 mm diameter) was used to prepare a working electrode. Ink containing the catalyst powder, water, methanol, and Nafion solution was deposited on a glassy carbon disk and dried at room temperature. The amount of Pd was adjusted to approximately 7.4 μg cm^{-2} on the working electrode. The working electrode was then immersed in 0.1 M HClO$_4$ solution. The CVs of the catalysts were measured by changing the potential of the working electrode in the range of 0.05 to 1.20 V at scan rate of 50 mV s^{-1} in N$_2$-purged HClO$_4$ solution. The polarization curves for the ORR were also obtained using a rotating disk electrode (RDE) method. During the measurement of the polarization curve for the ORR, the potential was changed from 0.05
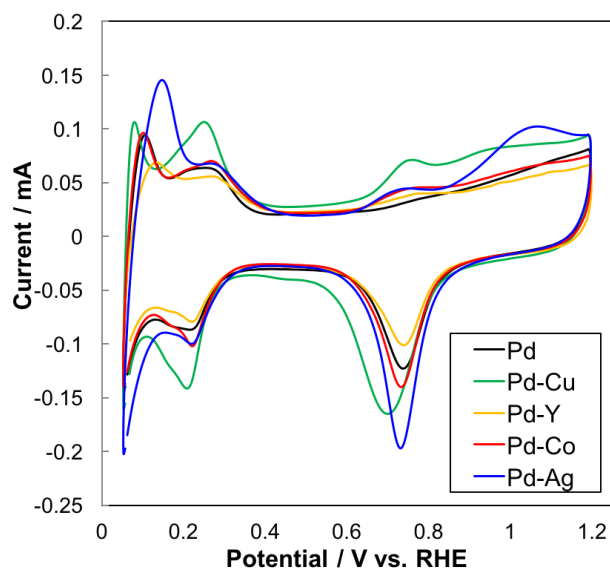
Fig. 4.1 CVs for Pd/CB and Pd-based catalysts.

to 1.20 V at scan rate of 10 mV s^{-1} with rotating rate of the working electrode at 1600 rpm in O$_2$-purged HClO$_4$. Durability test for the Pd-based catalysts was carried out by changing the potential of the working electrode in the range from 0.6 to 1.0 V at scan rate of 100 mV s^{-1} in N$_2$-purged HClO$_4$ solution. After the durability test, CVs and polarization curves of the ORR for the used catalysts were measured.

4.3 Results and discussion

4.3.1 Pd-based catalysts

Pd-M/CB(N) (M; Cu, Co, Ag and Y) catalysts were prepared in the present study. The Pd loading was fixed to 15 wt% and the molar ratio of M/Pd was adjusted to 1/1 for these Pd-M/CB(N) catalysts. Figure 4.1 shows CVs for Pd/CB and Pd-M catalysts. Two regions were observed in these CVs, that is, adsorption and desorption of hydrogen on Pd metal
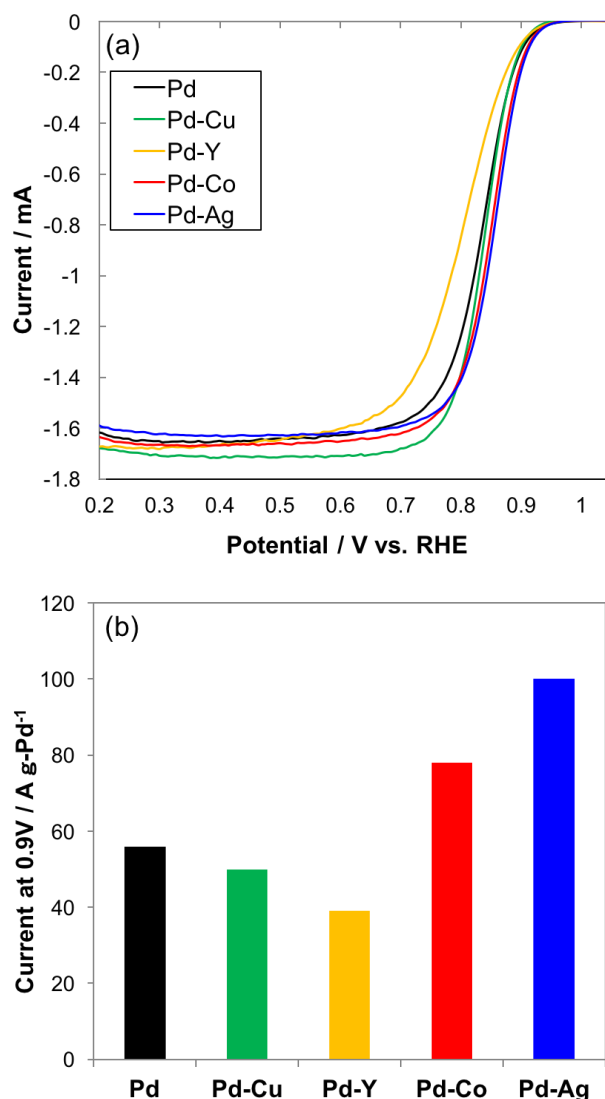
Fig.4.2 (a) Polarization curves for the ORR and (b) the ORR current at 0.9 V for
Pd-based catalysts.

surfaces in the potential range from 0.05 to 0.4 V, and the oxidation and reduction of Pd

metal in the potential range from 0.5 to 1.2 V. All the Pd-based catalysts showed similar

CV features, although peak position was dependent on the type of catalysts.

Figure 4.2 shows the polarization curves for the ORR (panel a) and the ORR current

at 0.9 V (panel b) for Pd-based catalysts. In the polarization curves for all the Pd-based

catalysts, a well-defined limiting-current region was observed at potentials lower than 0.7 V, while a mixed diffusion-kinetic control currents were seen in the potential range from 0.7 V to 1.0 V. Pd-Y/CB showed poorer activity for the ORR compared with Pd/CB. In contrast, the addition of Cu, Co and Ag into Pd/CB enhanced the ORR activity. The threshold for the polarization curves for the Pd-Ag and Pd-Co was clearly located at higher potential compared with that of Pd/CB. Figure 4.2b also shows the higher activity of these Pd-Ag and Pd-Co catalysts. The Pd-Ag/CB showed the highest ORR activity among all the Pd-based catalysts tested in the present study. The Pd-Ag catalysts had higher ORR activity by 2 times than Pd/CB. These results indicate that the modification of Pd metal with Ag and Co can improve their catalytic activity for the ORR. Catalytic performance of Pd-Ag/CB was investigated in detail hereafter to enhance their ORR activity furthermore.

4.3.2 Pd-Ag/CB catalysts

Pd-Ag/CB(I) catalysts were also prepared by a conventional impregnation method and their catalytic performance was compared with that of Pd-Ag/CB(N). Figure 4.3 shows XRD patterns of Pd-Ag/CB(N), Pd-Ag/CB(I), and Pd/CB. A broad diffraction peak due to carbon black was observed at around $2\Theta = 25°$ in all the Pd-based catalysts. The diffraction peaks at around 40° and 47° were assignable to a face centered cubic (fcc) phase of Pd and/or Ag metals. For the Pd-Ag/CB(I), broad diffraction peaks with some peaks appeared in the 2Θ range between 40° and 47°, and between 38° and 44°. This result indicates that alloying degree of Pd and Ag in the Pd-Ag/CB(I) was very low, that is, the catalysts have Pd-Ag alloys with various Ag/Pd ratios. In contrast, Pd-Ag/CB(N)
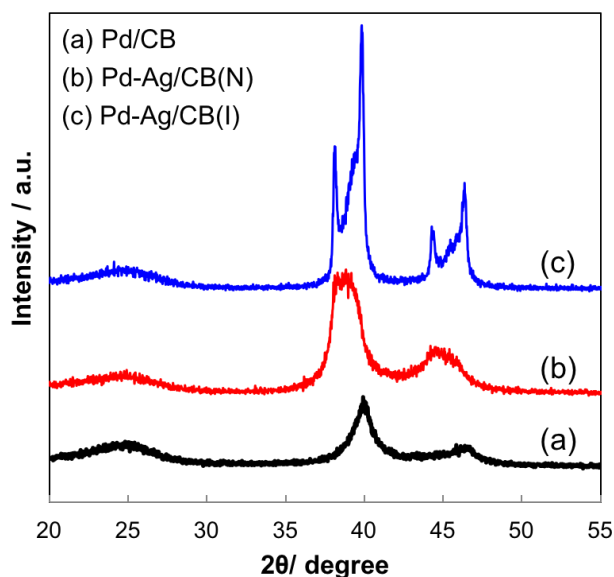
Fig. 4.3 XRD patterns of Pd-Ag/CB(N), Pd-Ag/CB(I), and Pd/CB.

had two peaks due to disordered alloy phases between Pd and Ag metals at around $2\Theta = 39°$ and $45°$ although these peaks were very broad. These results indicate that the composition of Ag to Pd of the metal particles in these Pd-Ag catalysts depends on the preparation methods. Thus, it should be noted that the alloy phase of Pd and Ag metals can be easily formed by the reduction with $NaBH_4$ in the presence of EG instead of the preparation at low temperature.

Figure 4.4 shows TEM, bright field-STEM, and dark field-STEM images of Pd-Ag/CB(I) (a, b, c) and Pd-Ag/CB(N) (d, e, f). In the TEM image for Pd-Ag/CB(I) (panel a), the metal particles of Pd, Ag or Pd-Ag alloys seemed to be deposited on carbon support. The metal particle size in the Pd-Ag/CB(I) was ranged from 4 to 20 nm and the average size was evaluated to be 9.1 nm by counting size of more than 200 particles. In contrast, metal particles were hardly observed in the TEM image for Pd-Ag/CB(N) (panel d), although the metal loading in the catalysts was quite similar to that for Pd-Ag/CB(I). To
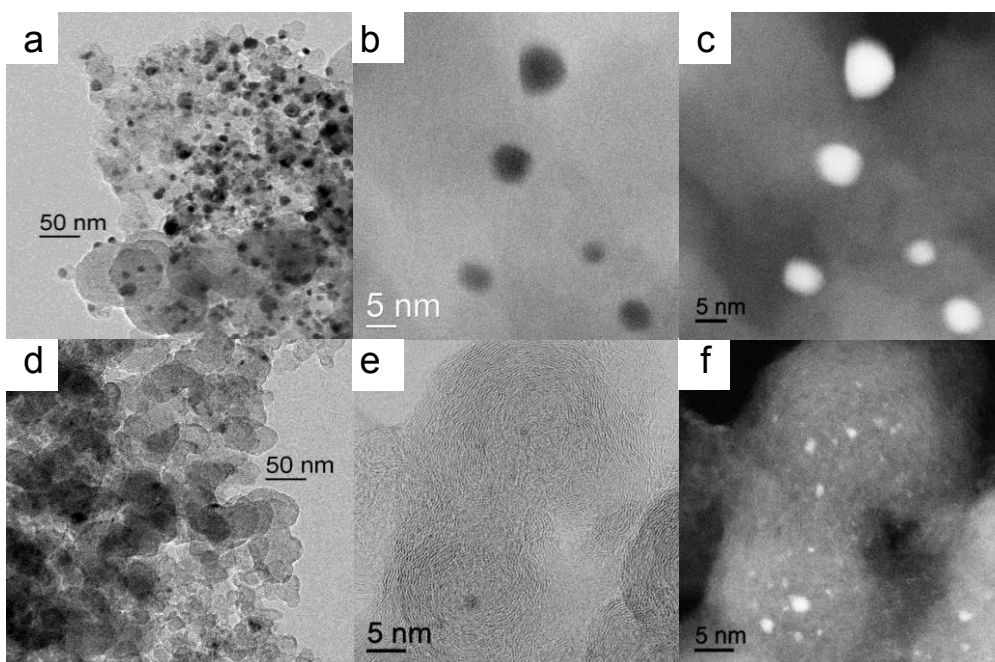
Fig. 4.4 TEM, BF-STEM, and DF-STEM images of Pd-Ag/CB(I) (a, b, c) and
Pd-Ag/CB(N) (d, e, f).

confirm the existence of metal particles in the Pd-Ag/CB(N), HAADF-STEM images were measured. The HAADF-STEM offers two types of images such as bright field (BF, panel e) and dark field (DF, panel f). In the BF-STEM image for Pd-Ag/CB(N), metal particles were hardly found, although a few particles with diameters of 1 ~ 2 nm were found in the image. In contrast, many metal particles could be obviously observed in the DF-STEM image for Pd-Ag/CB(N). The diameter of metal particles of Pd-Ag/CB(N) was very small and average size of metal particles was evaluated to be 2.3 nm. These results indicate that the metal particle size on the Pd-Ag/CB catalysts is affected by the preparation methods. As described earlier, the XRD pattern for Pd-Ag/CB(N) showed the formation of Pd-Ag alloys. Thus, we concluded that the reduction of Ag and Pd cations with NaBH$_4$ in the presence of EG leads to the formation of Ag-Pd alloys with very

93
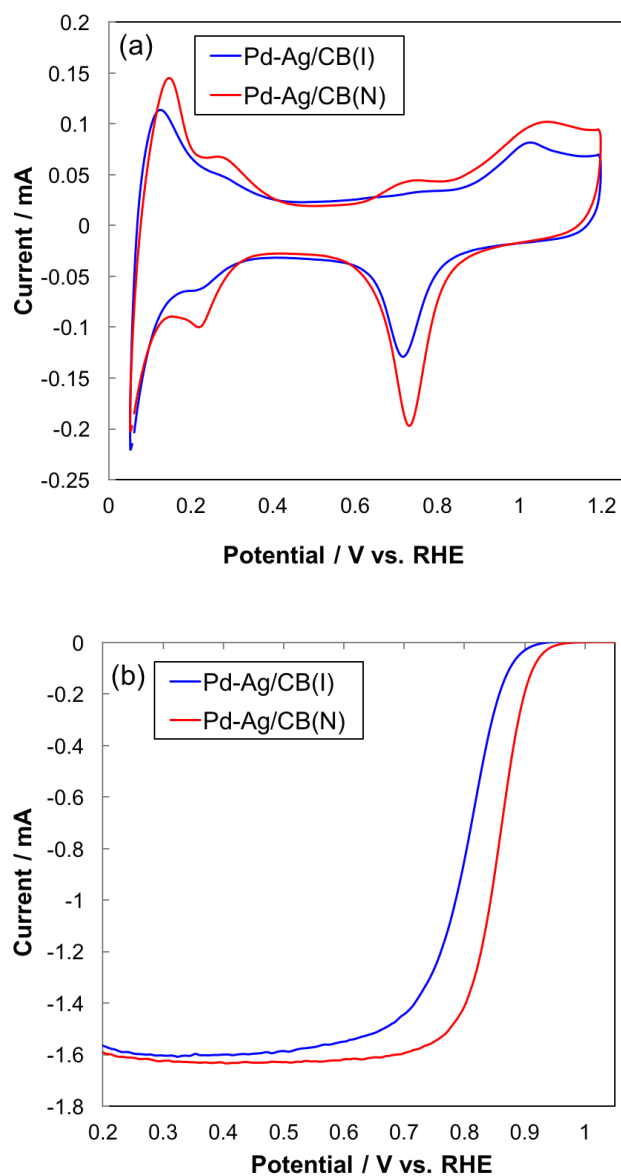
Fig. 4.5 CVs and polarization curves for the ORR of Pd-Ag/CB(I) and Pd-Ag/CB(N) catalysts.

smaller size. [14,18]. This is due to the protection of small alloy particles by EG.

Figure 4.5 shows CVs and polarization curves of the ORR for Pd-Ag/CB(I) and Pd-Ag/CB(N) catalysts. Two peak couples due to the adsorption and desorption of hydrogen, and the oxidation and reduction of Pd were observed in the CVs for both Pd-Ag/CB

catalysts. Although the positions of these peaks are similar in these CVs, the peak currents for Pd-Ag/CB(N) were larger than those for the Pd-Ag/CB(I), suggesting that electrochemically active surface area for the former catalysts is larger than that for the latter one. The Pd-Ag/CB(N) showed significantly higher activity for the ORR than the Pd-Ag/CB(I). As shown in Fig. 4.5b, the threshold for the polarization curve for the ORR at around 0.9 V was positioned at more positive potential for the Pd-Ag/CB(N) compared with that for Pd-Ag/CB(I). The ORR activity at 0.9 V was evaluated from these polarization curves to be 100 A g-Pd^{-1} for Pd-Ag/CB(N) and 14 A g-Pd^{-1} for Pd-Ag/CB(I). The high catalytic activity for the ORR of the Pd-Ag/CB(N) can be attributed to the small particle size and the synergistic effect between Pd and Ag by formation of Pd-Ag alloys.

Recent researches have reported that the ORR activity of Pd-Ag alloy catalyst can be affected by the high synergistic effect between Pd and Ag. In general, Pd metal strongly binds oxygen molecules due to high-lying d-band center, which results in easy O-O bond cleavage. Thus, most of surface Pd atoms are covered with oxygenated intermediates, to cause the low ORR activity. In contrast, Ag metal weakly binds oxygen molecules due to low-lying d-band center, leading to a lower coverage of oxygenated intermediates on Ag metal surfaces. Thus, when the optimal d-band center in the Pd-Ag/CB is obtained by formation of Pd-Ag alloys, the ORR activity can be improved [24–26].

The molar ratio of Ag/(Pd+Ag) in the Pd-Ag/CB(N) was changed to obtain further high catalytic activity for the ORR. Figure 4.6 shows XRD patterns of Pd-Ag/CB(N) with different molar ratios. Amount of Ag added in the Pd-Ag/CB(N) was changed with a fixed Pd loading of 15 wt%. As the Ag/(Pd+Ag) ratio increased from 0 to 50 %, the diffraction
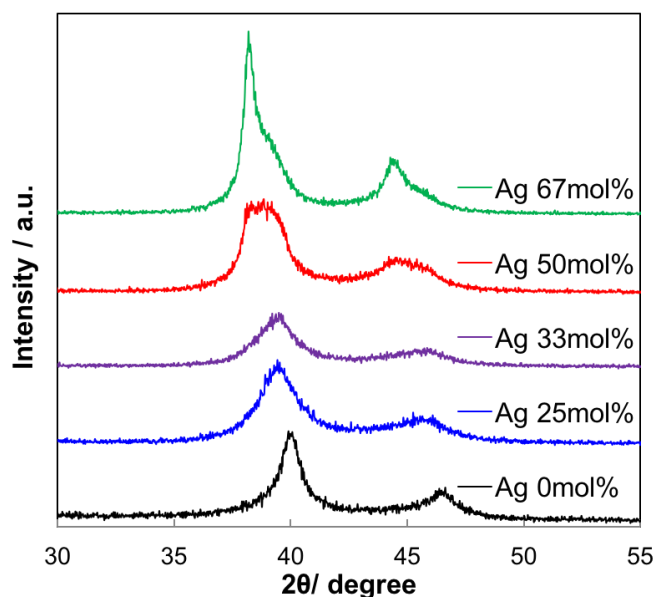
Fig. 4.6 XRD patterns of Pd/CB and Pd-Ag/CB(N) with different molar ratios.

peaks at around 40° and 47° were shifted to lower angles, indicating that the fraction of

Ag in the Pd-Ag alloys became higher with the Ag/(Pd+Ag) ratio. The peaks due to Pd-

Ag alloys were relatively symmetric in shape in the Ag/(Pd+Ag) range ≤ 33 mol%. In

contrast, the peaks due to Pd-Ag alloys became broad and asymmetric for the catalysts

with the Ag/(Pd+Ag) ≥ 50 mol%. Especially, strong peaks which are assignable to Ag

metal or Pd-Ag alloys with very high Ag fraction were seen in the XRD pattern for Pd-

Ag/CB(N) with Ag/(Pd+Ag) = 67%. Therefore, Pd-Ag alloys with uniform composition

are formed in the catalysts with Ag/(Pd+Ag) ≤ 33 mol%, whereas the alloying degree

between Ag and Pd in the catalysts with the Ag/(Pd+Ag) ≥ 50 mol% was low.

Figure 4.7 shows CVs and polarization curves for the ORR of Pd-Ag/CB with various

Ag/(Pd+Ag) values. The CVs for all the Pd-Ag/CB catalysts showed similar features each

other as shown in Fig. 4.7a. The catalytic activity of these Pd-Ag/CB(N) for the ORR
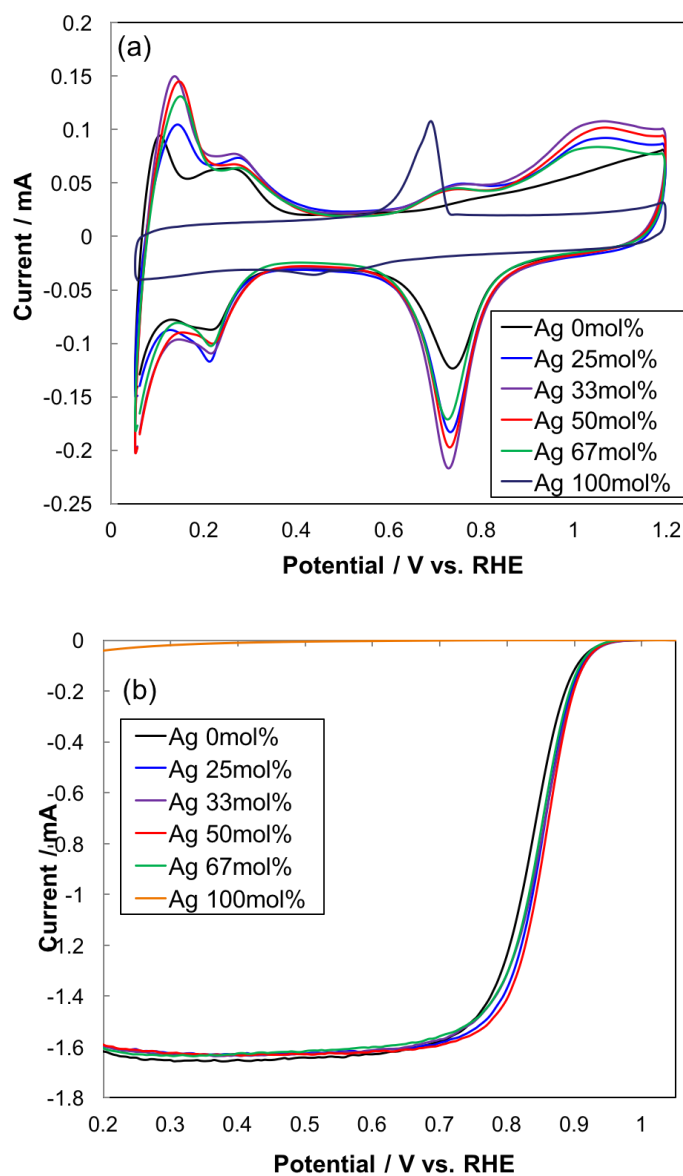
Fig. 4.7 (a) CVs and (b) polarization curves for the ORR of Pd-Ag/CB with various Ag/(Pd+Ag) values.

depended on the Ag/(Pd+Ag) ratio. Ag/CB did not have the catalytic activity for the ORR. The catalytic activity of Pd/CB was always lower than those of all the Pd-Ag/CB catalysts. The threshold of the polarization curves for the ORR was located at more positive potential in the catalysts with Ag/(Ag+Pd) ratio from 0.25 to 0.5. The ORR activity at 0.9
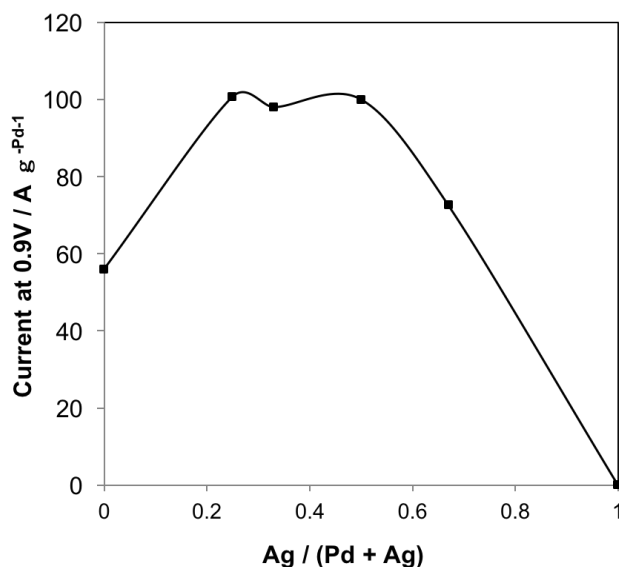
Fig. 4.8 Change in the catalytic activity for the ORR at 0.9 V of Pd-Ag/CB(N) catalysts with Ag/(Pd+Ag) values.

V for these Pd-Ag catalysts were summarized in Fig. 4.8. When the Ag/(Pd+Ag) ratios for the Pd-Ag/CB(N) increased from 0 to 25 mol%, the catalytic activity for the ORR increased. The activity for the ORR on the Pd-Ag/CB remained unchanged in the Ag/(Pd+Ag) ratio from 25 to 50 mol%. However, the addition of too much amount of Ag into the catalysts decreased the ORR activity.

4.3.3 Improvement in durability of Pd-Ag/CB by coverage with silica layers

The Pd-Ag/CB(N) with Ag/(Pd+Ag) ratio of 25 mol%, which had the highest ORR activity, was covered with silica layers to improve their durability under the cathode conditions. The SiO_2 loading of the prepared SiO_2/Pd-Ag/CB catalyst was 8 wt% by ICP analysis. Figure 4.9 shows DF-STEM images of SiO_2/Pd-Ag/CB(N). Size of metal
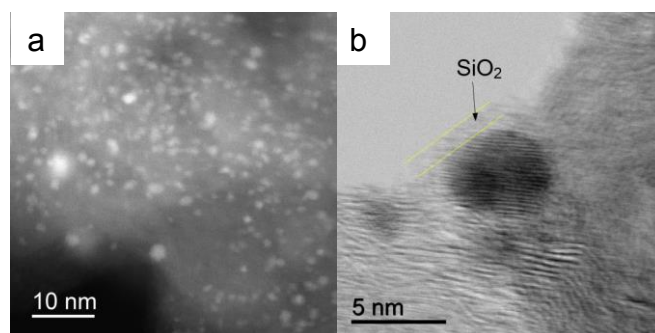
Fig. 4.9 DF-STEM images of SiO_2/Pd-Ag/CB(N).

particles observed in the images was relatively uniform. In addition, it seemed that metal particles were covered with silica layers (Fig. 4.9b). The durability of Pd-Ag/CB(N) and SiO_2/Pd-Ag/CB(N) was evaluated by measuring the CVs and polarization curves after the potential cycling between 0.6 and 1.0 V as a durability test.

Figure 4.10 shows CVs and polarization curves of the ORR for Pd-Ag/CB(N) without silica during the durability test. The peak currents in the CVs for the Pd-Ag/CB(N) were gradually decreased during the durability test. Especially, the peak at around 0.7 V due to the reduction of Pd oxides was diminished after 1000 cycles. The ORR activity for the Pd-Ag/CB also decreased with the number of the potential cycling. The onset potential of the ORR on the Pd-Ag/CB(N) was gradually shifted to more negative potential during the durability test. These results suggested that the metal species of Pd-Ag/CB(N) were dissolved during the durability test. Figure 4.11 shows CVs and polarization curves for the ORR of SiO_2/Pd-Ag/CB(N) during the durability test. The SiO_2 loading of the SiO_2/Pd-Ag/CB(N) catalyst was 8 wt% by ICP analysis. The peak currents in the CV for the fresh SiO_2/Pd-Ag/CB were very low compared to the fresh Pd-Ag/CB(N). The peak currents in the CVs for the SiO_2/Pd-Ag/CB(N) was gradually increased with the number
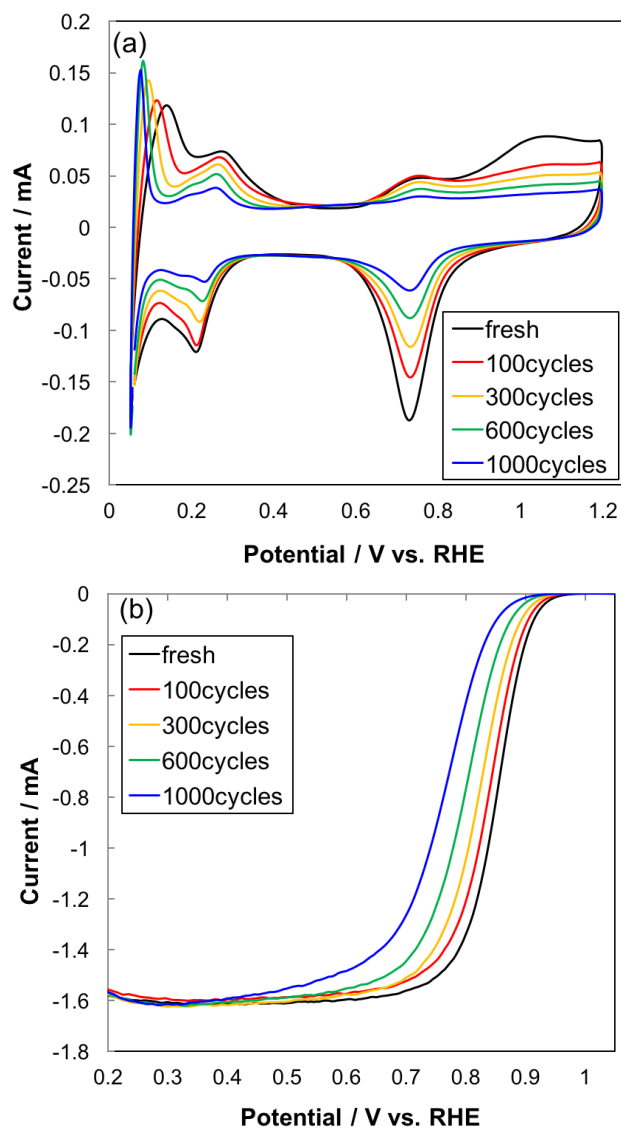
Fig. 4.10 (a) CVs and (b) polarization curves for the ORR of Pd-Ag/CB(N) during
the durability test.

of the potential cycles until 300 cycles and then maintained until 600 cycles. The

polarization curves of the ORR for the SiO_2/Pd-Ag/CB(N) shown in Fig. 4.11b also

showed the improvement of the catalysts by the coverage with silica layers. The fresh

SiO_2/Pd-Ag/CB(N) showed low activity for the ORR, but its activity increased with the

number of the potential cycling. The deactivation of the SiO_2/Pd-Ag/CB(N) was not
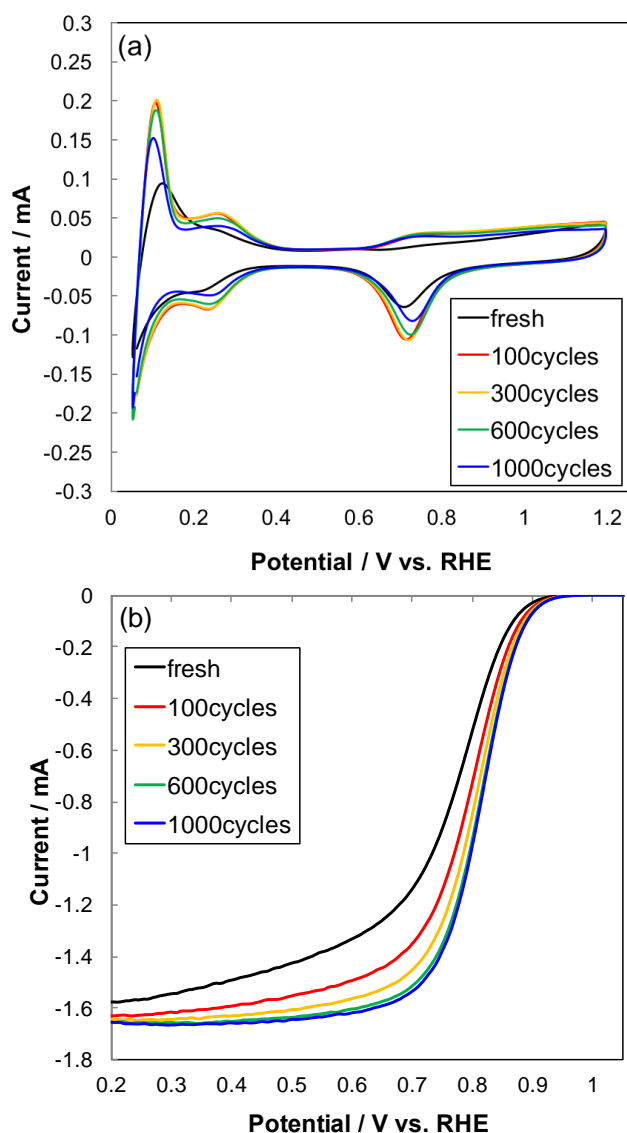
Fig. 4.11 (a) CVs and (b) polarization curves for the ORR of SiO_2/Pd-Ag/CB(N) during the durability test.

observed until 1000 cycles, while Pd-Ag/CB(N) without silica layers were seriously deactivated during the durability test.

The change of the ORR current at 0.9 V for the Pd/CB, Pd-Ag/CB(N) and SiO_2/Pd-Ag/CB(N) during the durability test was shown in Fig. 4.12. The ORR current for the fresh Pd-Ag/CB(N) was about twice higher than that of the fresh Pd/CB, but both the
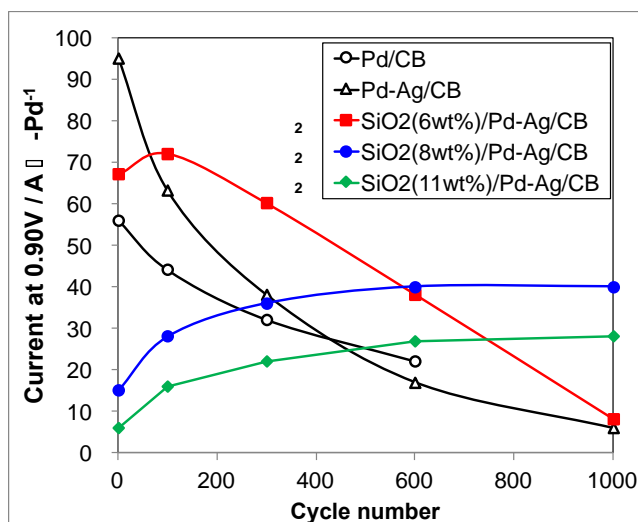
Fig. 4.12 Change in activity for the ORR of Pd/CB, Pd-Ag/CB(N), and SiO$_2$/Pd-Ag/CB(N) catalysts during the durability tests.

catalysts were quickly and seriously deactivated during the durability test. The ORR current for SiO$_2$(6wt%)/Pd-Ag/CB(N) was also rapidly decreased after 100 cycles. In contrast, SiO$_2$(8wt%)/Pd-Ag/CB(N) and SiO$_2$(11wt%)/Pd-Ag/CB(N) were not deactivated until 1000 cycles of the potential cycling. The coverage of Pd-Ag/CB(N) with silica layers led to the decrease in the catalytic activity for the ORR at early period of the durability test. However, the SiO$_2$(8wt%)/Pd-Ag/CB(N) showed higher activity since 300 cycles compared with Pd-Ag/CB(N). It should also be noted that the SiO$_2$(8wt%)/Pd-Ag/CB(N) had the highest activity for the ORR after 1,000 cycles among all the catalysts. That is, the silica layers which wrapped around Pd-Ag alloys improved their durability under the cathode conditions. In addition, the durability of SiO$_2$/Pd-Ag/CB strongly depends on the silica loading in the catalysts. Too thick silica layers on the Pd-Ag catalysts decreased the ORR activity significantly, but thin silica layers could not inhibit the deactivation of the catalysts during the durability tests. Thus, we can obtain the

SiO$_2$(8wt%)/Pd-Ag/CB as highly active and durable non-Pt cathode catalysts.

4.4 Conclusions

Pd/CB catalysts modified with transition metals such as Co, Cu, Y, and Ag were prepared by the reduction of metal precursors with NaBH$_4$ in the presence of EG. The Pd catalysts modified with Ag showed the highest catalytic activity for the ORR among all the modified Pd catalysts in the present study. The Pd-Ag/CB(N) prepared by the reduction with NaBH$_4$ in the presence of EG had the higher activity for the ORR than Pd-Ag/CB(I) prepared by the conventional impregnation methods. The higher catalytic activity of the Pd-Ag/CB(N) could be attributed to the synergistic effect between Pd and Ag metals by their alloy formation, and to the formation of small alloy particles. The coverage of the Pd-Ag/CB(N) with silica layers improved the durability of the catalyst under the cathode conditions, while non-coated Pd-Ag catalysts seriously deactivated during the durability test.

References

[1] M.K. Debe, Nature 486 (2012) 43–51.

[2] J. Greeley, I.E.L. Stephens, A.S. Bondarenko, T.P. Johansson, H.A. Hansen, T.F. Jaramillo, J. Rossmeisl, I. Chorkendorff, J.K. Nørskov, Nat. Chem. 1 (2009) 552–556.

[3] K. Jayasayee, J.A.R. Van Veen, T.G. Manivasagam, S. Celebi, E.J.M. Hensen, F.A. de Bruijn, Appl. Catal. B Environ. 111–112 (2012) 515–526.

[4] M. Oezaslan, P. Strasser, J. Power Sources 196 (2011) 5240–5249.

[5] J. Zheng, R. Fu, T. Tian, X. Wang, J. Ma, Int. J. Hydrogen Energy 37 (2012) 12994–13000.

[6] L. Liu, G. Samjeske, S. Nagamatsu, O. Sekizawa, K. Nagasawa, S. Takao, Y. Imaizumi, T. Yamamoto, T. Uruga, Y. Iwasawa, J. Phys. Chem. C 116 (2012) 23453–23464.

[7] S. Takenaka, T. Tsukamoto, H. Matsune, M. Kishida, Catal. Sci. Technol. 3 (2013) 2723.

[8] W. Zhou, M. Li, O.L. Ding, S.H. Chan, L. Zhang, Y. Xue, Int. J. Hydrogen Energy 39 (2014) 6433–6442.

[9] M.-H. Shao, K. Sasaki, R.R. Adzic, J. Am. Chem. Soc. 128 (2006) 3526–3527.

[10] S. Takenaka, H. Miyata, T. Tsukamoto, H. Matsune, M. Kishida, ECS Trans. 50 (2013) 1715–1722.

[11] J. Zhao, A. Sarkar, A. Manthiram, Electrochim. Acta 55 (2010) 1756–1765.

[12] L. Zhang, K. Lee, J. Zhang, Electrochim. Acta 52 (2007) 3088–3094.

[13] C. Luo, Y. Zhang, X. Zeng, Y. Zeng, Y. Wang, J. Colloid Interface Sci. 288 (2005) 444–448.

[14] Z. Yan, M. Wang, Y. Lu, R. Liu, J. Zhao, J. Solid State Electrochem. 18 (2014) 1087–1097.

[15] W.-D. Lee, D.-H. Lim, H.-J. Chun, H.-I. Lee, Int. J. Hydrogen Energy 37 (2012) 12629–12638.

[16] B.J. Hwang, S.M.S. Kumar, C.H. Chen, R.W. Chang, D.G. Liu, J.F. Lee, J. Phys. Chem. C 112 (2008) 2370–2377.

[17] P. Kim, J.B. Joo, W. Kim, J. Kim, I.K. Song, J. Yi, J. Power Sources 160 (2006) 987–990.

[18] J. Chen, C. Jiang, X. Yang, L. Feng, E.B. Gallogly, R. Wang, Electrochem. Commun. 13 (2011) 314–316.

[19] M.-S. Hyun, S.-K. Kim, B. Lee, D. Peck, Y. Shul, D. Jung, Catal. Today 132 (2008) 138–145.

[20] H. Matsumori, S. Takenaka, H. Matsune, M. Kishida, Appl. Catal. A Gen. 373 (2010) 176–185.

[21] S. Takenaka, A. Hirata, E. Tanabe, H. Matsune, M. Kishida, J. Catal. 274 (2010) 228–238.

[22] S. Takenaka, H. Matsumori, H. Matsune, M. Kishida, Appl. Catal. A Gen. 409–410 (2011) 248–256.

[23] S. Takenaka, H. Miyamoto, Y. Utsunomiya, H. Matsune, M. Kishida, J. Phys. Chem. C 118 (2014) 774–783.

[24] Y. Lu, Y. Jiang, X. Gao, X. Wang, W. Chen, Part. Part. Syst. Charact. 33 (2016) 560–568.

[25] S.T. Nguyen, H.M. Law, H.T. Nguyen, N. Kristian, S. Wang, S.H. Chan, X. Wang, Appl. Catal. B Environ. 91 (2009) 507–515.

[26] a. J. Armenta-González, R. Carrera-Cerritos, M. Guerra-Balcázar, L.G. Arriaga, J. Ledesma-García, J. Appl. Electrochem. 45 (2014) 33–41.

Chapter 5

Conclusions and future works

5.1 Conclusions

The objectives of this thesis are to develop new cathode electrocatalysts including both Pd-based catalysts and non-Pt catalysts with high activity for the ORR and durability to reduce the Pt loading in the PEFCs. A series of studies on the development of carbon nanofibers as a support for Pt or Pt-Co alloy metal catalysts, carbon-supported V-Mo oxides and active and durable carbon-supported Pd-Ag as non-Pt metal catalysts were conducted. The objectives of these studies could be achieved by each strategy. Conclusions of thesis studies are summarized below.

In Chapter 2, carbon nanofiber (CNF) support was developed for the stabilization of Pt-Co nanoparticles during the heat-treatment for the alloy formation. The CNF was formed by methane decomposition over SiO_2-supported Ni catalysts. The treatment of the CNFs with concentrated HNO_3 brought about the formation of porous structures in the CNFs in addition to the introduction of oxygen-containing functional groups on the CNFs. The porous structures in the CNFs inhibited the sintering of Pt metal particles when the CNFs were used as supports. Small Pt-Co alloy particles could be thus prepared on the CNF supports even after treatment of the catalysts at high temperatures. The CNF-supported Pt-Co alloy catalysts (Pt-Co/CNFs) showed a high activity for the ORR, which is attributed to small metal nanoparticles and high alloying degree.

In Chapter 3, the ORR activity of Mo-based oxide catalysts as non-Pt catalysts was investigated. Carbon black-supported Mo oxide catalysts (MoO_x/CB) were prepared from the different Mo precursors including Mo-based heteropolyacids (HPAs) by a conventional impregnation method. The MoO_x/CB modified with V cation exhibited the higher ORR current than MoO_x/CB. In particular, V-MoO_x/CB prepared from $H_3PMo_{12}O_{40}$ as a Mo precursor (V-MoO_x(HPMo)/CB) exhibited the highest catalytic activity for the ORR compared to the Mo-based oxide catalysts prepared by other Mo precursors. The high ORR current of the V-MoO_x(HPMo)/CB is attributed to the stable MoO_x in the acidic electrolyte, the increase in the reduction of MoO_x by interaction with V cations. In this chapter, we could obtain the cheaper and active V-MoO_x(HPMo)/CB as a cathode catalyst.

In Chapter 4, a study on carbon black-supported Pd-Ag alloy catalysts as a non-Pt catalyst was conducted. The ORR activity of Pd/CB catalysts modified with transition metals such as Co, Cu, Y, and Ag was evaluated. The Pd catalysts modified with Ag (Pd-Ag/CB) showed the highest catalytic activity for the ORR among all Pd catalysts modified with other metals in the present work. In addition, the Pd-Ag/CB prepared by the reduction with $NaBH_4$ in the presence of EG had the higher activity for the ORR than Pd-Ag/CB prepared by the conventional impregnation method. The higher catalytic activity of the Pd-Ag/CB could be attributed to the synergistic effect between Pd and Ag metals by their alloy formation, and to the formation of small alloy particles. The low durability of Pd-Ag/CB was solved by silica-coating method. The coverage of the Pd-

Ag/CB with silica layers enhanced the durability of the catalyst under the cathode conditions, while non-coated Pd-Ag catalysts seriously deactivated during the durability test. In this chapter, we conclude that the prepared Pd-Ag alloy covered with silica layers is active and durable in the acidic electrolyte.

In summary, we achieved the enhancement of catalytic activity for the ORR and durability on the new cathode catalysts including the CNF-supported Pt-Co alloy catalysts, V-Mo oxide catalysts, and silica-coated Pd-Ag alloy catalysts. Thus, we contributed to reduction in the Pt utilization on the cathode of PEFCs.

5.2 Future works

All of the cathode electrocatalyst technologies realized throughout the present thesis are in the experimental stage for application of the PEFCs. All of the cathode electrocatalysts including the Pt-based catalysts and non-Pt catalysts should be evaluated by a single cell to be applied to current PEFC's system. However, new electrocatalysts developed in this thesis need further optimization of the activity for the ORR and durability in the experimental stage. Thus, we suggest future works about further optimization of these cathode electrocatalysts in detail.

Firstly, we did not try to evaluate the durability of the Pt-Co/CNFs yet. It was known that metal alloy particles are usually easier to dissolve than pure Pt although the interaction between Pt alloy metals and the CNF is stronger than that of Pt alloy metals and the CB. Therefore, the Pt-Co/CNFs should be subjected to durability test at varying conditions, such as from 0.6 to 1.0 V vs. RHE under oxygen saturated acidic electrolytes

to investigate the dissolution of the Pt-Co nanoparticles, and at potential values higher than 1.0 V vs. RHE to explain corrosion of the CNF support.

Secondly, the stability of the active V-MoO$_x$(HPMo)/CB as non-Pt catalyst in the present study was low in acidic electrolyte due to the dissolution of V cation. Thus, the stability of the V-MoO$_x$(HPMo)/CB should be improved to overcome lower activity for the ORR durability compared to the conventional Pt catalyst. We think that when V cation is immobilized on the support material, the stability of the V-MoO$_x$(HPMo)/CB will be improved, which results in the enhancement of its ORR activity. It is proposed to utilize the CNF supports which was used as the support for Pt-Co alloy catalyst in chapter 2. Since, these CNF promotes the dispersion of metal oxide species as active sites for the ORR.

Finally, the SiO$_2$/Pd-Ag/CB showed high activity for the ORR and durability. However, we did not fully consider the silica layers of SiO$_2$/Pd-Ag/CB. Silica layers on Pd-Ag/CB are formed by hydrolysis with (3-aminopropyl)triethoxysilane (APTES) and tetraethoxysilane (TEOS). Thus, we should consider the amount of APTES and TEOS to obtain optimal silica layers on the Pd-Ag/CB. When we find the optimal silica layers on the Pd-Ag/CB, the durability of SiO$_2$/Pd-Ag/CB can be improved.

ACKNOWLEDGEMENT